



CENTRO DE INVESTIGACIONES
EN ÓPTICA, A.C.

Predictive Modeling of Visual Quality



Ph.D. in Optical Sciences

Advisor: Dr. Daniel Malacara Hernández

Student: Francisco Javier Gantes Nuñez

- Versión definitiva. Incluye cambios sugeridos por revisores -

December 2019
León, Guanajuato, México

“Nobody ever figures out what life is all about, and it doesn’t matter. Explore the world. Nearly everything is really interesting if you go into it deeply enough.”

Richard P. Feynman

Abstract

In this work we investigate two different modeling approaches oriented towards caring for vision in humans. Firstly, numerical wavefront reconstruction methods are applied to quantify the ocular aberrations from data obtained using Hartmann patterns. Two geometries of the Hartmann patterns are considered, square and hexagonal. For each unit cell, a polynomial function is proposed instead of the standard approach using a single polynomial. This approach improves pupil sampling, yielding a better precision in the representation of the aberrations. Secondly, models of human eyes affected by the pathologies of age-related macular degeneration (AMD) and glaucoma are presented. Novel personalized eye models to predict the quality of vision in AMD are developed. These models are presented in order to validate effective techniques to measure the progression of retinal edemas in AMD using simple Amsler grids, it is possible to link the grid distortions with the size of macular edemas. In addition to the theoretical investigations mentioned, a clinical study was done to assess the ocular surface temperature in different zones using long-wave infrared thermal imaging. This study examined the dynamics of temperature changes in glaucoma and healthy patients. The results indicate that subjects with glaucoma cool faster than healthy subjects.

In general, the work presented in this thesis is focused on the development of methods and diagnosis techniques to improve visual quality.

Resumen

En este trabajo se investigaron dos enfoques diferentes de modelado orientado al cuidado de la visión en humanos. Primeramente, métodos numéricos de reconstrucción de frente de onda son aplicados para cuantificar las aberraciones oculares de datos obtenidos de patrones de Hartmann. Dos geometrías de patrones de Hartmann son considerados, cuadrado y hexagonal. Para cada celda unitaria, una función polinomial es propuesta en lugar del enfoque estándar de utilizar un solo polinomio para la pupila, este enfoque mejora el muestreo de la pupila generando una mejor precisión en la representación de las aberraciones. Segundo, se presentan modelos del ojo humano afectados por las patologías de degeneración macular relacionado con la edad (AMD) y glaucoma. Estos modelos son presentados con la finalidad de validar técnicas efectivas para medir la progresión de edemas retinianas en AMD mediante el uso de rejillas de Amsler. Se encontró que utilizando las distorsiones de las rejillas de Amsler es posible vincular el tamaño de los edemas maculares. Adicionalmente a las investigaciones teóricas mencionadas, un estudio clínico fue realizado para evaluar la temperatura de la superficie ocular en diferentes zonas utilizando imágenes térmicas de infrarrojo lejano. Este estudio examinó la dinámica de los cambios de temperatura en pacientes con glaucoma y pacientes control. Los resultados indican que los sujetos con glaucoma sufren un enfriamiento más rápido que los sujetos sanos.

En general, este trabajo presentado en esta tesis está enfocado en el desarrollo de métodos y técnicas de diagnóstico para mejorar la calidad visual.

***To my mom, my dad, my
sister, and my brother.***

Acknowledgments

It would be impossible to name all the people that helped and influenced me to finish this work, but I am going to try to name the people I consider most relevant in my life.

Firstly, I would like to thank Dr. Zacarías Malacara and Dr. Daniel Malacara because of their valuable teaching and support through my graduate studies. I am very grateful they accepted me to work with them, it has been an honor. I cannot be more grateful to them; they have supported me in different aspects of my life. Then, other people from the academic field which I am going to name in the order in which they have appeared. To Dr. Carlos Villaseñor, a very important person in my decision to study a graduate degree and in particular in study Optics. Nowadays I consider Dr. Villaseñor a friend and advisor, he has taught me not only academically topics, but also he has taught me how to be a better person. Dr. Sabino Chávez, you have taught me that hard work always yields results in academic and personal life. Because of your guidance and support, you have helped me to begin my journey as a researcher. Moreover, Dr. Sabino has believed in me, in my abilities and it helped me to be more confident. Thank you, Dr. Sabino. I have to name M.C. Enrique Landgrave as he has been a valuable person who, since he was elected as an examiner of my Ph.D. thesis, attempted to give me advice and from him, I learned to be more critical, analytical and careful in science.

To Dr. Juan Tabernerero, thank you for all the trust and knowledge you have shared with me, for your guidance and support, I really enjoyed working with you. Thank you to the VERI team from Anglia Ruskin University, Dr. Nery García, Dr. Carles Otero, Dr. Tjerk Zult, Dr. Rich Warner, Elena, Elsa, and finally, but not less important, Megan Vaughan. Megan, she was one of the first people that helped me in Cambridge not only in the academic field, also she helped me in my adaptation to life in this beautiful city. Moreover, thank you, Megan, for the review and corrections about my thesis, and because of you, I started to be more deeply interested in reading.

Dr. Armando Gómez and Dr. Geovanni Hernández, thank you, they have been concerned about my academic formation. They have given me support, help, and advice through my master's and Ph.D. degree.

Thank you to the CONACyT for the scholarships and CIO for allowing me to develop in my graduate studies. To all the staff members from the CIO, for the 'buenos días' and the knowledge, they shared with me.

Secondly, in my personal life, I have to thank my parents, David and Mary, my sister Dany and my brother Luis David, they have been my main reason to be the person I am. Because my family are the most important people I have in my life, there are no words to describe their support and value to me.

Pau Vázquez, what can I say about your friendship, you have been there for me every time I need it with the perfect words and advice. Thank you, Pau. To Montse... I remember receiving a message from you at the perfect time.

Thank you 'Compa' Jorge García, since we were together in the master's degree you helped me and in my predoctoral internship in England as well.

I would like to thank, again, Dr. Juan and his family, Dr. Estela, his wife, to his sons Juan, Pedro and Elena, they made me feel at home during my stay in Cambridge.

There a lot of friends and people I should name and thank, friends from the CIO, from my hometown, 'El Molino', from Cambridge, UK, but I would need a lot of pages. As I always said, I am a very lucky man, in every place I have been, there have always been people that have helped me...

Contents

Preface	1
List of Figures	3
List of Acronyms	6
Chapter 1 - The Human Eye: Overview	7
1.1 General Anatomy and Physiology.....	7
1.2 Optical Structure and Retina.....	8
1.2.1 The Cornea.....	9
1.2.2 The Lens.....	10
1.2.3 The Retina.....	11
1.4 Conclusions.....	13
Chapter 2 - Ocular Aberrations and Other Pathologies	15
2.1 Ocular Aberrations.....	16
2.1.1 Wavefront Definitions.....	17
2.1.2 Transverse Aberrations.....	19
2.1.3 Hartmann and Shack-Hartmann Sensor Tests, Measuring the Aberrations ..	21
2.1.4 Wavefront Retrieval.....	23
2.2 Age-Related Macular Degeneration.....	24
2.2.1 Amsler Grid Test.....	26
2.3 Glaucoma.....	27
2.4 Conclusions.....	28
Chapter 3 - Zonal Wavefront Reconstruction with Square Cells	29
3.1 Wavefront Considerations.....	29
3.2 Sampling and Identification of Point Distribution in a Square Pattern.....	31

3.3 Wavefront Retrieval in a Square Cell	36
3.3.1 Aberration Coefficients Calculation	37
3.3.2 Calculation of the Aberration Values Inside Each Square Cell	41
3.3.3 Contiguous Cells Coupling and Wavefront Representations	43
Chapter 4 - Zonal Wavefront Reconstruction with Hexagonal Cells.....	50
4.1 Design and Implementation of the Hexagonal Hartmann Pattern	51
4.2 Wavefront Retrieval in a Hexagonal Cell.....	57
4.2.1 Aberration Coefficients Calculation	58
4.2.2 Aberration Values Within the Hexagonal Cells Calculation.....	67
4.2.3 Contiguous Cells Joining and Wavefront Representations	69
4.3 Conclusions	81
Chapter 5 -Eye Models to Predict Quality Vision in Age-Related Macular Degeneration	82
5.1 Eye Model with Age-Related Macular Degeneration.....	82
5.2 Conclusions	87
Chapter 6 - Ocular Surface Characterization Using Infrared Thermography	88
6.1 Infrared Thermography and Eye Temperature Measurement	89
6.2.1 Methodology	91
6.2.2 Results.....	92
6.3 Conclusions	94
Chapter 7 - Conclusions	95
Bibliography	98

Preface

The human eye and vision were probably some of the first interests for optics science, in order to understand the vision system. It is clear that the study of the human eye started before the development of light sources and instruments. But interestingly, nowadays, visual optics have been improved with advances from other areas, such as astronomy, with the use of wavefront sensing and adaptive optics as an example.

The interest to improve the quality of vision is the first attempt to understand the human eye. There is evidence that Christopher Scheiner in 1619 published a work describing a principle to test the refraction of the human eye [1]. The principle described by Scheiner uses a disk perforated with two holes, which reminds similar to the Hartmann screen. After Scheiner, Tscherning in 1894 attempted to measure the refractive errors using a four-dimensional spherical lens with a grid pattern, with the aim to project it on the retina [2]. Finally, in 1900 Hartmann developed his test and although he established it in order to evaluate optical surfaces, it has been used to measure ocular aberrations [3].

The development of refractive surgery represented an important stimulus in the progression of the visual optics field [4]. The main purpose of this procedure is to reduce the refractive aberrations of the human eye. There are references that suggest refractive corrections by Hermann Boerhaave in 1708, but it was not performed until 1746 by von Haller, although the first published evidence is from the 1890s [5].

Hermann von Helmholtz can be considered as one of the first scientists that describe the human eye as an imperfect optical instrument. It was not until 1873 with the English translation of *Popular Lectures on Scientific Subjects* published in New York that the work of Helmholtz about the eye was known [6], [7]. In this work, Helmholtz described the structure of the human eye, spherical aberration, astigmatism, and some pathologies of the optic nerve. Furthermore, this scientist was the first one to look at a living retina,

which, nowadays, seems to be a normal thing, thanks to the works of Liang and Williams [8].

In this work, two methods of wavefront reconstruction are proposed using square and hexagonal Hartmann patterns. These techniques have the advantage that not only one polynomial is obtained to rebuild the wavefront, instead, but several polynomials are obtained, one for each cell. The contribution of these methods can be applied to corneal topography; allowing more accurate measurements of the cornea. Further, preliminary models of the human eye with Age-Related Macular Degeneration (AMD) are presented, in order to develop an easy and cost-effective method for screening retinal edemas in AMD using Amsler grids. Finally, an ocular surface temperature analysis is presented as a procedure that evaluates the temperature dynamics in glaucoma patients using infrared thermography.

This work is divided into six chapters. Chapter 1 is an overview description of the human eye, presenting the refractive elements and retina. Chapter 2 describes ocular aberrations and some definitions in order to understand them, as well as AMD and glaucoma, are mentioned. Chapter 3 and Chapter 4 present the wavefront reconstruction methods using square and hexagonal Hartmann patterns and the advantages over other methods are discussed. In Chapter 5 the methodology of the eye models to predict and screen the development of retinal edemas is presented. Finally, in Chapter 7, the study of temperature dynamics of the ocular surface in glaucoma patients is presented, considering some controlled factors and using thermography.

List of Figures

Figure 1-1.- Schematic illustration of the horizontal section of the right eye. Figure adapted from Atchison and Smith. [11] 8

Figure 1-2.- Section of the retina showing different layers involved in phototransduction. 11

Figure 2-1.- Original image and the representation of the four major defects caused by several facts such as ocular aberrations and some pathologies. 16

Figure 2-2.- Wavefront deformations, graphic representation. Each column represents an order..... 19

Figure 2-3.- Classical Hartmann set up. 21

Figure 2-4.- Shack-Hartmann Sensor set up. A micro-lenslet subdivides the wavefront into zonal areas. 22

Figure 2-5.- Graphic representation of the retinal affectations in wet and dry AMD. 25

Figure 2-6.- Amsler grid. It is a checkerboard with a square pattern where the patients look at the center and described the missing lines or deformed lines. 26

Figure 2-7.- Comparison between a normal and a glaucoma eye. 27

Figure 3-1.- Three possible Hartmann screen patterns. (a) Triangles. (b) Squares. (c) Hexagons. 30

Figure 3-2.- Square screen patterns placed in a pupil with a diameter D , which is divided into cells with size s . (a) A sampling point is centered at the center of the pupil and (b) a square cell is centered. 31

Figure 3-3.- Square cell parameters to design the square screen patterns. 32

Figure 3-4.- Transverse aberrations measurements with different reference spheres. (a) From the optical axis. (b) Square pattern, closer sphere, used as a reference and (c) reference square array in presence of spherical aberration. 34

Figure 3-5.- Labels of the sampling points within the square cell with an angle θ_0 40

Figure 3-6.- Square cells pattern with points inside them to evaluate the wavefront deformations. Also, subscripts (i, j) , (m, n) and (k, l) are shown. The (i, j) values are the position of the sampling point, represented by black circles, and they are the position of

the cell as well; so, the location of the cell is represented by the lower-left corner sampling point. (m, n) coordinates are the positions of the inner points for each one of the cells, with the cell center as the origin. For the case of (k, l) values, they are coordinates with reference at the pupil center..... 42

Figure 3-7.- Once the piston term has been optimized, the two contiguous cells coincide along the border; continuous wavefronts, continuous slopes but discontinuous curvatures. Two adjacent wavefronts have the same slopes at the border, thus, they have the same heights, but the second derivative might be different..... 43

Figure 3-8.- The filling process of (i, j) cells. If the cell (i, j) is on the right, the piston term is obtained by the average of the difference between the left and lower cells. In contrast, if the cell (i, j) is on the left side, the right and lower cells are used. 45

Figure 3-9.- Wavefront simulation using the Zernike polynomials shown in Table 3.1 and the wavefronts reconstruction using trapezoidal integration and the proposed method. (a) Wavefront simulation selecting some arbitrary wavefront coefficients. (b) Wavefront the trapezoidal integration method and (c) wavefront retrieved with the proposed method. [62] 48

Figure 4-1.- Hexagonal cell with sampling points at vertices and coordinate numbers for a hexagonal cell in a hexagonal array. 52

Figure 4-2.- Interpretation of the values θ_0 and m , and angles $m\alpha'$ and θ 53

Figure 4-3.- Triangle shaped by the pupil center, a selected cell and the first cell of a ring. 53

Figure 4-4.- Hexagonal arrays with a different number of rings in a circular pupil. 55

Figure 4-5.- Interpolated spots, red crosses, inside the hexagonal cells that cover the whole pupil. 67

Figure 4-6.- Contiguous cells illustrating the distance between two sampling points and the apothem length..... 68

Figure 4-7.- Representation of hexagonal cells before the piston term calculation (a) and after (b)..... 69

Figure 4-8.- Sampling points shared between contiguous cells and the twelve cases to calculate the piston term. 70

Figure 4-9.- (a) Hexagonal Hartmann pattern with 96 sampling points and (b) square Hartmann pattern with 120 sampling points. 73

Figure 4-10.- (a) Simulated wavefront to be tested and retrieved, (b) retrieved wavefront after trapezoidal integration, (c) retrieved wavefront using square cell integration and (d) retrieved wavefront after hexagonal cell integration [88]. 74

Figure 4-11.- (a) Wavefront values data, (b) Partial derivatives in x and (c) Partial derivatives in y. 80

Figure 5-1.- Standard Wisconsin Age-Related Maculopathy grading system. The grid is defined by three concentric circles centered at the macula. 83

Figure 5-2.- Schematic eye model with drusen deformations of 300 μm in the retina. . 83

Figure 5-3.- Male subject of 85 years old and AMD. (a) Cross-sectional retinal fundus image of a patient with late AMD. (b) Image vision simulation of an image. (c) Schematic eye of the patient with AMD. (d) Amsler grid simulation. 85

Figure 5-4.- Male subject of 76 years old and AMD. (a) Cross-sectional retinal fundus image of a patient with late AMD. (b) Image vision simulation of an image. (c) Schematic eye of the patient with AMD. (d) Amsler grid simulation. 86

Figure 6-1.- Zones where the temperature was measured. [97] 92

Figure 6-2.- Temperature values measured in control and glaucoma subjects. (a) Eyelid, (b) central ocular surface and (c) peripheral ocular surface at $t = 0$ s. Squares and points represent controls and glaucoma, with the main value in green asterisk. [97] 92

Figure 6-3.- Average OST changes in the central cornea zone. Green lines are the periods of time analyzed to find the cooling rates. [97] 93

Figure 6-4.- Cooling rate (a) from 0 to 2 seconds, (b) from 2 to 4 seconds and (c) from 4 to 8 seconds. [97] 93

List of Acronyms

Acronym	Term
AMD	Age-Related Macular Degeneration
ARM	Age-Related Maculopathy
RPE	Retinal Pigment Epithelium
GA	Geography Atrophy
IOP	Intraocular Pressure
OAG	Open-Angle Glaucoma
ACG	Angle-Closure Glaucoma
VERI	Visual and Eye Research Institute
IR	Infrared
OST	Ocular Surface Temperature
CEC	Controlled Environmental Chamber

Chapter 1 - The Human Eye: Overview

The healthy human eye is a sophisticated optical system that is capable of forming images on the retina with a good resolution. It belongs to a general group of eyes well-known as 'camera-type eyes', because, in a simple manner, the eye works as a camera lens focusing light onto a film. In the eye, the optical imaging system is formed by the cornea and crystalline lens, while the retina is the detection instrument. Now, the complexity of the eye comes when it is analysed as a complete biological organ as the neural connections have to be considered. As the cornea and lens are 'living' lenses, other factors like organic components, start to be important.

The eye can be explained from an optical system perspective; thus, it can be affected by aberrations that reduce the quality of the retinal image. The total aberration contribution can be divided between the two components of the optical imaging system: the cornea and the crystalline lens. Additionally, deteriorations in the retina, discussed in Chapter 6, reduce the image resolution. However, there are additional factors responsible for the degradation of retinal images, such as diffraction in the pupil and intraocular scattering [9], [10].

In this chapter, an overview of the human eye is studied in order to introduce some elements that contribute to the quality of vision.

1.1 General Anatomy and Physiology

In a general manner, the human eye can be organized in three layers distinguished in Fig. 1-1. Starting from the exterior layer or region, it is formed by the cornea and sclera. The main function of the cornea is to refract and transmit the light to the lens and retina at last. Whereas, the sclera is a membrane that protects and maintains the eye shape.

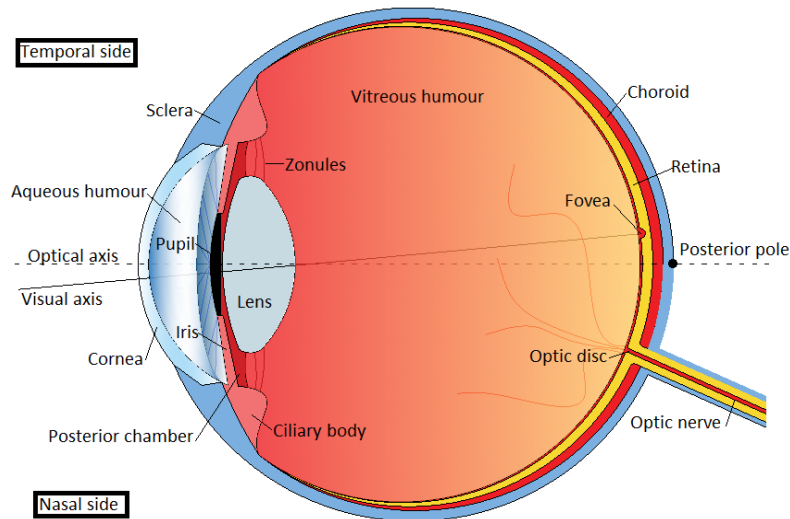


Figure 1-1.- Schematic illustration of the horizontal section of the right eye. Figure adapted from Atchison and Smith. [11]

In the middle area the iris, ciliary body, and the choroid are situated, where the iris controls the pupil size and acts as a diaphragm [11]. The ciliary body's main function is to control the shape and hence the power of the lens, its secondary function is producing aqueous. The third element, the choroid, is the layer where oxygen and nutrients are provided to the outer retinal layer.

The third area is the inner layer, composed of the retina, a very complex layered structured. The retina formed by neurons, whose function is to capture and process light. There are three transparent chambers that are surrounded by the ocular layer considered previously, the anterior, posterior and vitreous chamber.

1.2 Optical Structure and Retina

The eye has two refracting elements: the cornea and the lens. The analysis of the tear film and its influence in the refractive power is not considered in this work. There are some characteristics to consider related to these elements, like transparency, curvatures and refractive index, in order to generate an image with a good quality [11]. On the other hand,

the retina is an element that gets the information from the outer environment and transmits it to the brain.

The main objective of this section is to describe a brief overview of the eye, so, the cornea, lens and the retina are presented in order to understand some basic optical parameters and functionality.

1.2.1 The Cornea

The cornea is considered as the most densely innervated tissue of the body and furthermore, is avascular. Also, this is the first element where the incident light can be transmitted, absorbed or scattered. Light scattering is present only if some small irregularities are present in the retina. It is a thin, approximately *0.55 mm*, transparent layer, with a diameter of about *12 mm*. From the *12 mm*, *4 mm* corresponds to the optic zone, which is responsible for most of the refractive function and is located in the center of the cornea [12].

The cornea is an almost sphere with an anterior radius of 7.8 mm and 6.5 mm of posterior radius, and a refractive index value of 1.3771 [9]. Since the main difference in refractive index occurs between the cornea and the air, the largest refractive power of the eye is due to the cornea, about 70%.

As the cornea is the first and most significant refracting surface of the human eye, it is also the main source of high order aberrations and astigmatism. Hence, the methods and techniques to measure and correct the aberrations in the cornea are still in research, because the quality of the retinal image can be improved if the corneal aberrations are corrected. Nevertheless, it is necessary to consider that the cornea and lens work together to form a high-quality retinal image, and this is the reason for the complexity of analysis of the cornea or lens as individual elements.

The pupil, another element that works with the cornea and lens, has a direct influence on imaging. It is a variable opening localized in the center of the iris, which is a sphincter muscle with a central aperture that regulates the amount of light entering. The

pupil size can vary from 2 mm in bright light to approximately 8 mm in the dark, and as was said, it influences the image quality, mainly because if its size is less than 2 mm , the effect of diffraction is significant [9].

More detailed information on the cornea can be found in many specialized books in this area [10], [11].

1.2.2 The Lens

After the light has passed through the pupil, the lens is the second refracting surface. The lens is a dynamic tissue that changes its shape in order to modify the optical power of the whole eye. The capacity of the shape modification is well-known as the basis of the mechanism of accommodation, which allows the focusing of images on the retina. Suspensory ligaments, known as zonules, are the connections between the lens and ciliary body of the eye, and they are responsible for the changes in lens shape when a contraction or relaxation is presented.

Approximately one-third (20 D) of the total dioptric power is due to the lens, whose shape, in a very basic description, is a biconvex lens. The truth is that the crystalline is not a simple system. Its biological nature makes a complex system with aspheric surfaces and inhomogeneous with a gradient refractive index, with the characteristic that the refractive index is larger in the center than in the periphery. Further, the lens is an element that through life keeps growing, and this growth produces an age-dependency of the features. Several works have been attempting to represent novel shapes and effects of the lens, such as the works presented by Gómez-Correa et. al. [13], [14], were using two distinct spheroidal hemispheres, a complete description of the lens is made, also including the gradient refracting index and age-dependency.

Another reason that makes it difficult to analyze the crystalline lens is its location. It is located in the posterior chamber of the eye, where its anterior surface is in contact with the central zone of the iris. The lens, in the same manner as the cornea, is a transparent avascular element with an average refractive index value of 1.42 and a thickness of about 3.6 mm when is in a relaxed state.

For a detailed description of the lens crystalline, see specialized books [10], [11] and papers [13], [14] related to this topic.

1.2.3 The Retina

The retina is a receptive organ with light-sensitive functionality that is responsible for the absorption and translation tasks. It is formed by several layers that perform different optical functions in order to improve the image formation. At the same time, in the retinal layers, there are six classes of neurons: bipolar cells, horizontal cells, amacrine cells, ganglion cells and photoreceptors, where its influence in the visual system is to capture and process the light, and the last kind of neuronal cell are the Müllerian glia [12]. The basic organization of these layers shown in Fig. 1-2.

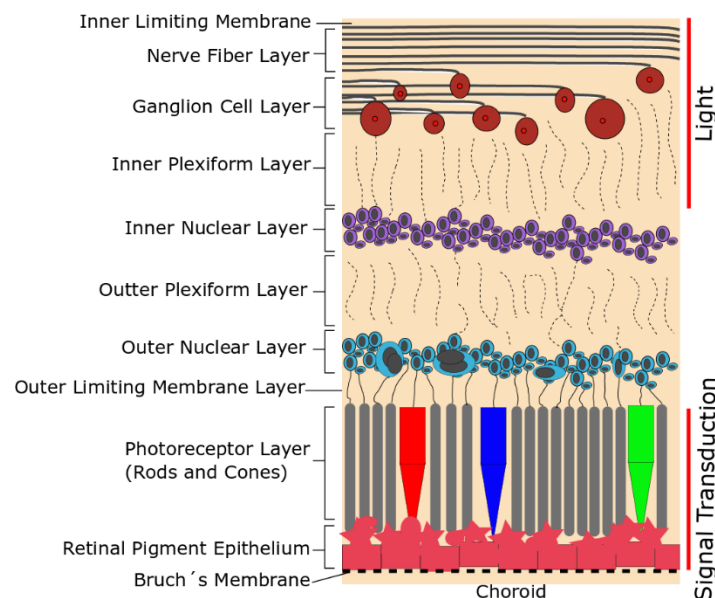


Figure 1-2.- Section of the retina showing different layers involved in phototransduction.

As can be inferred from Fig. 1-2, the choroid and sclera protect and support the retina structure.

The central area of the retina is called the fovea, where the cone photoreceptors are located and the light-photoreceptor interaction is performed, thus, it is in this area where the optics become critical. The interaction light-photoreceptor is an important

aspect of the visual optics because it is the previous step of the neural response. This interaction is named absorption, and this concept can be understood only if the light is considered a particle, called a photon, and this process is performed by the photoreceptors. In other words, the photoreceptors develop the task of transforming the light into an electrical signal interpreted by the neurons.

Most of the vertebrate's eyes, including the human eye, have two types of photoreceptors in the retina, i.e., rods and cones. The relation between rods and high sensitivity to low levels of light is common, contrary to the cones, but, the neural wiring has an important meaning with the light levels [11]. The responsible elements of absorption in the photoreceptors are pigments. In the rods, the rhodopsin is the pigment present, in which peak absorption is about *496 nm* and in the cones, there are three types of photopsin pigments centered at *419*, *531* and *559 nm*, or blue, green and red sensitives cones [10].

The ratio between rods and cones is 20 to 1 approximately and they are distributed in the retina. The majority of cones are located in the peripheral retina, when it could be inferred that the majority of them should be in the fovea, which is located about 5° wide of the optical axis and is the area responsible for sharp central vision. However, there are more cones in the fovea than rods. It is important to mention that even when the fovea is considered as the ventral vision, it is located off-axis position, contrary to the aberration theory, which establishes that the best image position of an optical system is on the optical axis.

There is another region in the retina named the optic disc, where there are no cones or rods present, so, it means that this region is 'blind'. This area is where the vascular supply enters and the visual information travels through the optic nerve to the brain. The visual phototransduction is the process in which light is transformed into electrical signals. In this process, photoreceptors and the optic nerve are involved. The optic nerve is the structure that works as a messenger due to this element transmit the information received by the photoreceptors.

Once the optical components of the human eye have been described, it is possible to find all these values in models known as schematic eyes. There are several schematic eyes, which have been made with average values of populations and considering some specific characteristics. Moreover, some schematic eyes can be very complex describing the refractive surface with aspheric and gradients of refractive index, but all this complexity results in elaborate calculations. On the other hand, paraxial schematic eyes are simpler and are mostly used, although, for accurate results, a sophisticated schematic eye could be the best option. In this work, to analyze the Age-Related Macular Degeneration, AMD, the Escudero-Navarro eye model is used [15]. This is a paraxial model and the geometrical parameters are described in Table 1.1. Further reviews of schematic eyes can be found in some papers and books [10], [11], [16]–[18].

Table 1.1 - Geometry of the Schematic Wide-Angle Eye Model.

Surface	Type	Conic Constant	Radius (mm)	Thickness (mm)	Optical Medium	Refractive Index (543 nm)
1	Conic	-0.26	7.72	0.55	Cornea	1.3777
2	Spherical	0	6.50	3.05	Aqueous	1.3391
Stop	Plane	0	Infinite	0	Aqueous	1.3391
4	Conic	-3.1316	10.20	4.00	Lens	1.4222
5	Conic	-1	-6.00	16.3203	Vitreous	1.3377
Image	Spherical	0	-12.00	-	-	-

1.4 Conclusions

In this chapter, a general overview of the elements of the human eye was presented in order to understand the following chapters. Analyzing the refractive elements and retina of the human eye can be inferred that those components contribute to the quality of vision.

In addition, other elements that are out of this work, such as the eyeball and central nervous system, are part of the complex optical system that decreases the visual quality.

As part of understanding the contributions of the elements to the visual quality, an interesting question arises; how far can the human vision be improved?

Chapter 2 - Ocular Aberrations and Other Pathologies

In the previous chapter, a brief description of the human eye structure and functionality was presented. As can be understood, the human eye is a very complex system because of all the elements that compound it, but because of its sophistication, it has to be assumed that it is not a perfect optical imaging system. The reason is that there are several factors that cause a degradation of the retinal images, and they are not just refractive errors due to the cornea and lens.

Besides the optical aberrations, chromatic and monochromatic, diffraction caused by the pupil and intraocular scattering, there are other issues responsible for imperfect images. In the case of chromatic aberrations, these can be longitudinal, a variation of power conditioned to the wavelength, and transverse, image position changes in the retina according to the wavelength. This type of aberrations has a considerable presence in the human eye, but, the real influence on the image is relatively small. It can be explained from the presence of different kinds of pigments in the retina and the ocular media, as well as the lens, act as wavelengths filters. The lens is capable of absorbing short-wavelength light, mostly blue, mitigating the chromatic aberration. Also, there is a yellow macular pigment which is the main filter [9].

For the reasons explained, in the following sections definitions related to ocular aberrations and two pathologies are presented. AMD and Glaucoma, which are two of the most frequent causes of blindness in the world are described [19]. In order to get a better idea of the treatment in this chapter, Fig. 2-1 shows a representation of the refraction errors and four of the major pathologies.

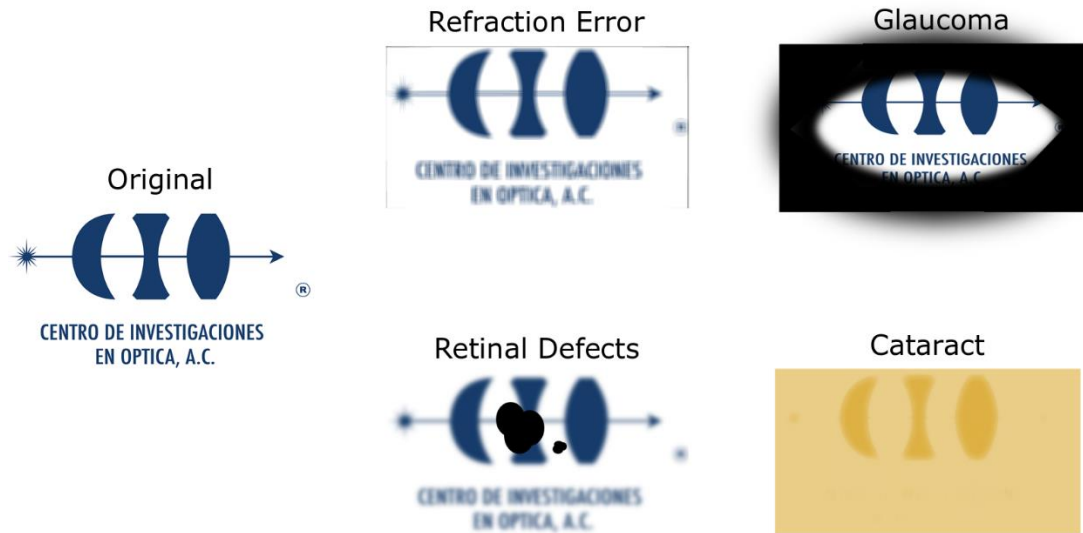


Figure 2-1.- Original image and the representation of the four major defects caused by several facts such as ocular aberrations and some pathologies.

2.1 Ocular Aberrations

Usually, most ocular aberrations are due to defocus and astigmatism, which are better known as refractive errors. Myopia and hyperopia are those defects caused by defocusing and usually they are corrected by ordinary ophthalmic lenses. However, those defects are not the only source of ocular aberrations [4].

High order aberrations are defects that also contribute to the visual quality, mainly when pupils are bigger in diameter, as during the night. Spherical aberration and coma are examples of high order aberrations and produce halos and double vision, respectively.

A normal vision needs all the elements involved in the visual system to work together. The refractive elements, the retina, optic nerve, and central nervous system, to name a few, are in charge of developing a good image.

It is useful to understand the wavefront and wavefront aberration terms before the discussion of the representation and measurement. For this reason, in the following sections, an overview of wavefront terms and measurement techniques are presented to explain some pathologies.

2.1.1 Wavefront Definitions

In terms of physical optics, the wavefront is associated with the phase of the complex field of an electromagnetic wave. Thereby, the planes of a wave that have the same phase at a specific time shape a wavefront [20], [21]. In geometrical optics, the envelope of rays is interpreted as a wavefront where the phase can be considered constant [22]. This definition can be deduced from the theorem of Malus and Dupin, which establishes that after a reflexion or refraction, a normal rectilinear ray remains normal [23].

With the wavefront definition, we can define an aberrated wavefront as the optical path difference between a reference sphere and the aberrated wavefront

$$W(x, y) = \text{aberrated wavefront} - \text{reference sphere} \quad (2.1)$$

It is normal to use an analytical expression to describe the wavefront irregularities produced by aberrations. A polynomial representation is the most used analytical expression and can be written as

$$W(x, y) = \sum_{i=0}^N \sum_{j=0}^i a_{i,j} x^{i-j} y^j \quad (2.2)$$

where N is the degree of the polynomial. However, since most of the optical systems have a circular shape, and therefore the pupils do too, it is more natural to write the polynomials in polar coordinates. In this case, the expression to get a polar representation can be written in two forms $\rho^n \cos^m \theta$ and $\rho^n \sin^m \theta$ or alternatively, $\rho^n \cos m\theta$ and $\rho^n \sin m\theta$. The expression in polar coordinates can be obtained as follows

$$W(x, y) = \rho^n \begin{bmatrix} \cos \\ \sin \end{bmatrix} (l\theta) \quad (2.3)$$

where $l = 0, 1, \dots, n$ with the condition that $n + l$ should be even.

As the Eq. 2.3 has to be a single-valued function, there are two conditions that have to be satisfied:

- a) The m value has to be smaller or equal to n .
- b) The sum $n + m$ has to be even.

Now, the selection of the trigonometric functions, *cosine* or *sine* and the value of l , in Eq. 2.3 can be determined as in Table 2.1.

Table 2.1.- Selection of the trigonometric functions and l value for Eq. 2.3.

$n+m$ parity	Value of l	Trigonometric function
Even	m	cos
Odd	$m-1$	sin

Therefore, Eq. 2.3 for the wavefront deformation is the following

$$W(\rho, \theta) = \sum_{n=0}^N \sum_{m=0}^n A_n \rho^n \begin{bmatrix} \cos \\ \sin \end{bmatrix} (l\theta) \quad (2.4)$$

From Eq. 2.4 the aberration terms up to 3rd power are in Table 2.2 and a graphic representation is shown in Fig. 2-2.

Table 2.2.- Aberrations terms used to represent the wavefront deformations $W(\rho, \theta)^*$.

N	m	r	l	Polar Coordinates	Cartesian Coordinates	Name
0	0	0	0	1	1	Piston
1	0	1	1	$\rho \cos \theta$	x	Tilt about y axis
	1	2	1	$\rho \sin \theta$	y	Tilt about x axis
2	0	3	0	ρ^2	$x^2 + y^2$	Defocusing
	1	4	2	$\rho^2 \cos 2\theta$	$x^2 - y^2$	Astigmatism, axis at 0° or 90°
	2	5	2	$\rho^2 \sin 2\theta$	$2xy$	Astigmatism, axis at $\pm 45^\circ$
3	0	6	1	$\rho^3 \cos \theta$	$(x^2 + y^2)x$	Coma, along x axis
	1	7	1	$\rho^3 \sin \theta$	$(x^2 + y^2)y$	Coma, along y axis
	2	8	3	$\rho^3 \cos 3\theta$	$(x^2 - 3y^2)x$	Triangular astigmatism, semi-axes at $0^\circ, 120^\circ, 240^\circ$
	3	9	3	$\rho^3 \sin 3\theta$	$(3x^2 - y^2)y$	Triangular astigmatism, semi-axes at $30^\circ, 150^\circ, 270^\circ$

*The angle θ is measured counter-clockwise, with respect to the x axis.

Where r is given by

$$r = \frac{n(n+1)}{2} + m \tag{2.5}$$

the subscript n is the degree of the polynomial and $m = 0, 1, 2, \dots, n$.

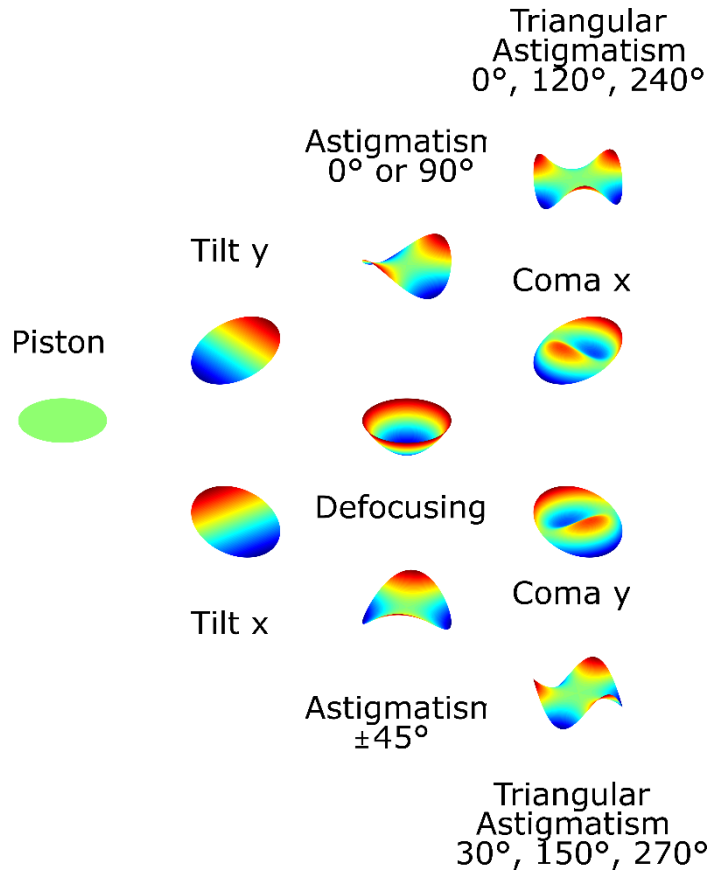


Figure 2-2.- Wavefront deformations, graphic representation. Each column represents an order.

2.1.2 Transverse Aberrations

From the point of view of geometrical optics, to consider an imaging optical system as ideal, it is necessary for the system to produce an image point of a point light source. Now, in terms of physical optics, as the light is considered a wave, a point source has to emit a spherical wavefront [24]. Consider that, the only way to get an ideal image point is when the optical system produces a convergent and perfect spherical wave.

With the wavefront definitions and considering a perfect spherical wave, aberrations can be interpreted as deviations or irregularities from this ideal spherical wave. Understanding the anterior description, it is inferred that the measurements of aberrations are obtained by the difference between the aberrated wavefront and a close reference sphere.

Most of the real optical systems, even centered optical systems, may produce asymmetrical aberrations. This is due to the fact that some optical surfaces are imperfect spheres or surface decentering. Consequently, most of the time is necessary to test wavefronts with random deformations.

As is habitual, the local wavefront slopes in the x and y directions, transverse aberrations, are related to the wavefront with the following equations

$$\begin{aligned}\frac{\partial W(x, y)}{\partial x} &= -\frac{TA_x}{r_w} \\ \frac{\partial W(x, y)}{\partial y} &= -\frac{TA_y}{r_w}\end{aligned}\tag{2.6}$$

where r_w is the radius of curvature of the wavefront if the transverse aberrations are measured at the radius of curvature. Although also, r_w could be the distance from the pupil to the plane where the transverse aberrations are measured.

The transverse aberrations in polar coordinates are given by

$$\begin{aligned}TA_\rho &= -r_w \frac{\partial W(\rho, \theta)}{\partial \rho} \\ TA_\theta &= -\frac{r_w}{\rho} \frac{\partial W(\rho, \theta)}{\partial \theta}\end{aligned}\tag{2.7}$$

A larger pupil size implies that irregular aberrations have to be considered in the polynomial representation. Thus, the importance of the use of polynomial terms not included in the classic aberrations of conventional optical systems. Equally, in some cases there are wavefront deformations that are neighboring the edge of the pupil and, a high-order polynomial has to be used. The reason to use a high-order polynomial is with the purpose of include high spatial frequencies and also if the wavefront has small and

strong irregularities [25], [26]. But, the usage of high-order polynomial signifies a large computing time and, in some cases depending on the wavefront retrieval method, increased numerical errors.

2.1.3 Hartmann and Shack-Hartmann Sensor Tests, Measuring the Aberrations

The Hartmann [3] and Shack-Hartmann [27] tests are methods that use a screen to sample a wavefront. The basic Hartmann set up consist of placing an opaque screen with a two-dimensional array of openings into the entrance pupil of the system under test, Fig. 2-3.

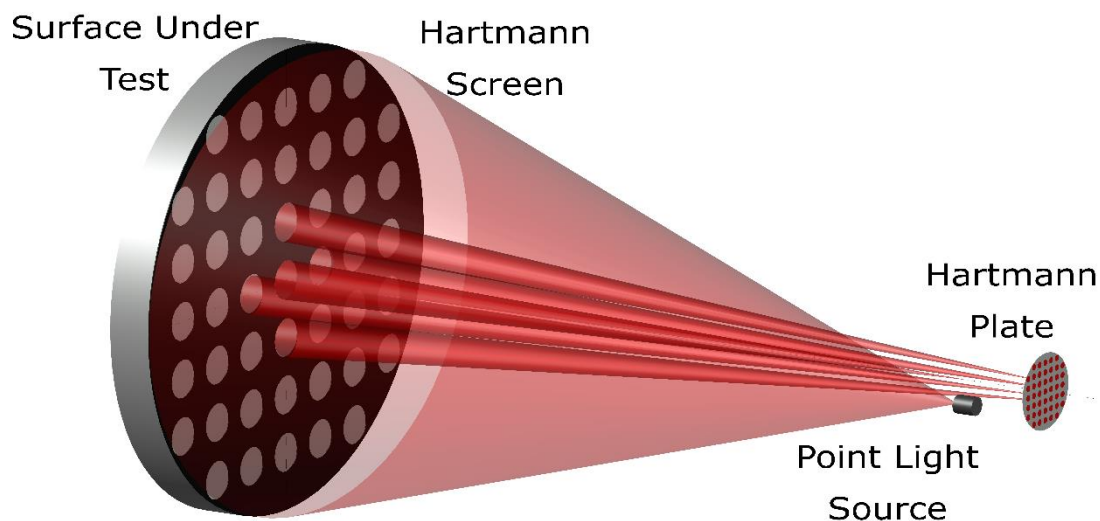


Figure 2-3.- Classical Hartmann set up.

Although there are many different configurations of the Hartmann test, as described by Malacara-Hernández *et. al.* [28], all of them have two basic elements, an opaque screen with a two-dimensional array of holes or lenslets and a Hartmann plate. However, the use of a screen is not the only option to evaluate the wavefront with the Hartmann test. In 1999 Laude *et. al.* introduced a Hartmann wavefront scanner where an aperture can be displaced programmatically over the wavefront [29]. Also, the use of a

Liquid-crystal television has been reported [30] and this system of the scanner has been implemented in an aberrometer as well [31].

The purpose of the Hartmann screen is to sample the wavefront slopes at different points, sampling points, on the entrance or exit pupil of the optical system under test. While the Hartmann plate is a set of defocused images of the object point light source.

Originally, the Hartmann test was developed as a method to test astronomical mirrors [32], but nowadays the Shack-Hartmann wavefront sensor has been adopted by visual optics instruments to measure ocular aberrations [7], [33]–[35]. The main difference between Hartmann and Shack-Hartmann tests is the replacement of the screen with an array of holes with a lenticular screen. However, there are other essential differences such as the collimated beam of light used in Shack-Hartmann instead of the convergent light beam required in the Hartmann test. Furthermore, Shack-Hartmann Sensor has the advantages that it can be used to test a positive or negative power and the spots have a light energy density higher than in the Hartmann test. Fig. 2-4 shows a basic set up for the Shack-Hartmann Sensor test.

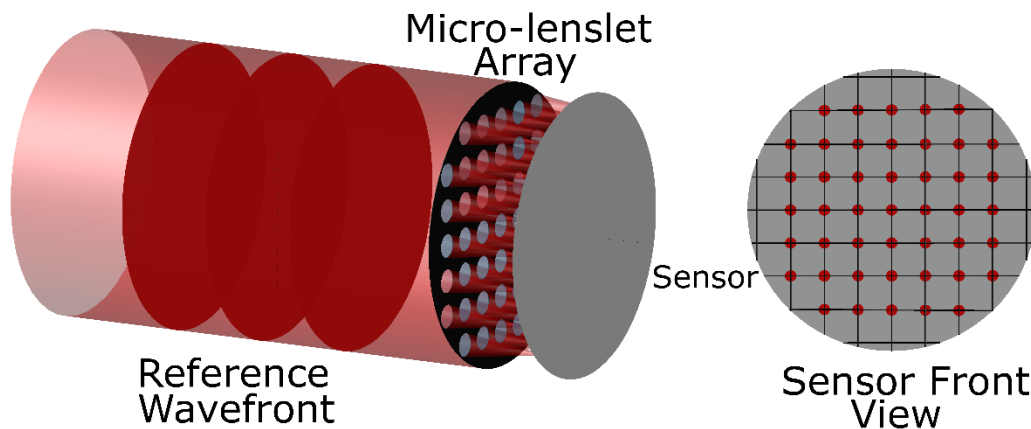


Figure 2-4.- Shack-Hartmann Sensor set up. A micro-lenslet subdivides the wavefront into zonal areas.

2.1.4 Wavefront Retrieval

As it is well-known, a set of local slopes of the wavefront are measured with the Hartmann test, so, the wavefront information is obtained from the image of an array of spots. The local slope is obtained from the distance between the optical axis of the lenslet and the corresponding spot. The reference Hartmann pattern can be obtained from the measurement of a planar wavefront. Henceforth, a displacement is proportional to the local slope of the wavefront in the area tested with the sensor. Each spot in the focal plane matches up with the corresponding portion of the wavefront sampled by a specific lenslet.

Since these tests measure wavefront slopes, an integration method is necessary to obtain the wavefront deformations. These methods can be classified into two categories, i.e., zonal and modal, including the well know trapezoidal integration, the Southwell integration algorithm [36] and polynomial fitting. With polynomial fitting, a smooth retrieved wavefront is obtained, as a result of filtering high spatial frequencies. This is due to the fact that spatial frequencies with a period shorter than the sampling point separation of the Hartmann sampling points are filtered out.

Another example of a wavefront retrieval method is by using Fourier analysis [17] but excludes the need for centering the spots using a Fourier transform of the Hartmann pattern. This technique also filters out high spatial frequencies, like modal methods. As a result of modal methods, they can be appropriate for optical systems or surfaces that are smooth enough, so, the polynomial representation has a relatively small order. An example of a suitable application of modal methods is testing astronomical instrumentation [37].

Usually, a high order polynomial is required when the wavefront deformations are close to the edge of the pupil for the purpose to fit the data without losing high spatial frequencies. Unfortunately, high order polynomial fitting requires large computing time and also it can add some non-desirable numerical errors. Hernández-Gómez *et. al.* [26], [38] shown that a polynomial fitting, even if a high degree is used, can show numerical errors or to a large computing time for some wavefront profiles with strong and small extent irregularities.

For the case of zonal methods [36], [39], [40], they do not fit the whole wavefront to a polynomial, so they are more appropriate to measure small extent irregularities. When eye aberrations are trying to be measured, is common to use a zonal method since the human eye is a kind of non-smooth wavefront with high irregularities. In addition, there are some exceptional cases when the use of both methods is necessary in order to compare results. As an example of wavefront retrieval method, the common trapezoidal integration method is a case which its accurate depends if the transverse aberrations are almost linear, or, the wavefront curvature is almost constant, which, in most cases, it is not true especially in the presence of strong wavefront aberrations. Most of the time, trapezoidal integration is a good wavefront retrieval method for astronomical mirrors in its final testing stages, but in other cases, as in human eye testing, it is not.

2.2 Age-Related Macular Degeneration

The rising prevalence of AMD is a significant secondary effect due to the increase in life expectancy. In this aspect, visual diseases are a considerable group of interest, besides chronic diseases such as heart diseases, cancer, and diabetes. AMD is one example of a visual disease with an association with age, it is suffered by people older than 60 years [41], though this is not the only factor. AMD is considered a complex disease caused by several risk factors among which are age, genetics and the environment [41]–[44]. This disease is the leading cause of visual loss and blindness since it affects approximately 30-50 million people worldwide, but with a projected amount of 288 million by 2040 [45], [46].

The main affected zone due to AMD is the macula, where the fovea is located and this is responsible for the high acuity vision. As explained previously, photoreceptors and the retinal pigment epithelium are situated in this area, which means that the dysfunction of these causes the visual loss. Usually, this disease generates a malfunction of the physiologically immunosuppressive sub-retinal environment.

There are two stages of progress identified in AMD, the early and late phases. In early AMD, also called age-related maculopathy (ARM), the presence of soft protrusions

called *drusen* starts to be visible. The drusen are an accumulation of membranous and lipoproteinaceous debris located between the retinal pigment epithelium (RPE) and Bruch's membrane. As can be inferred, the existence of drusen deforms the retina, producing metamorphosis. They can have a size of less than $63\ \mu\text{m}$ in diameter for hard drusen or between 63 and $1000\ \mu\text{m}$, or even aberrometer, for soft drusen [47]. The presence of a few small drusen is not related to AMD, but they can be an indicator of the possibility to develop AMD.

For the case of late AMD, it is developed when large-sized soft drusen are present and AMD is divided into two clinical forms: exudative or neovascular ('wet') and geography atrophy, GA ('dry'). In neovascular AMD, a choroidal neovascularisation grows in the RPE, seeping fluids like lipids or blood, which produces fibrous scarring well-identified as retinal edemas. On the other hand, geography atrophy is characterized by the degeneration of the photoreceptor layer or loss of RPE, and the lesions can develop in scotomas [42], [47], [48]. Figure 2-5 illustrates a graphic representation of late AMD affecting the retina.

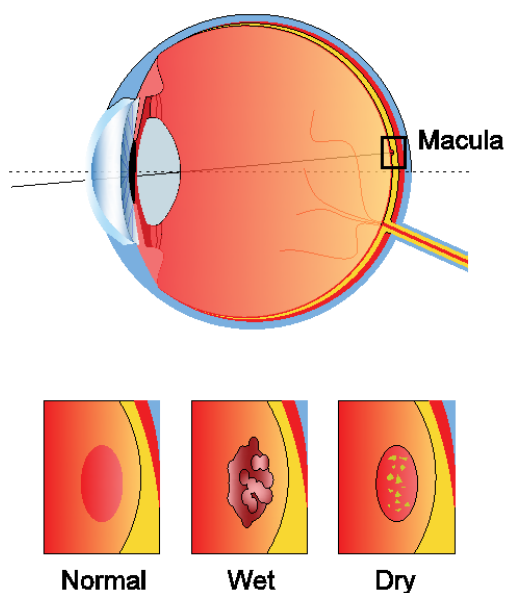


Figure 2-5.- Graphic representation of the retinal affectations in wet and dry AMD.

As the lesions due to AMD can be of a size, that can be visible in a fundus exploration, the development and improvement of some identification techniques have been advanced during the time. Fundoscopy, imaging, central visual field testing

(fluorescein angiography, fundus autofluorescence, optical coherence tomography, and microperimetry) and electrophysiology are examples of methods of diagnosis.

2.2.1 Amsler Grid Test

Despite the variety of technological AMD diagnosis methods that have been developed, the monitoring of progression is a difficult task. The time consuming, pricey, and in some cases, difficult to perform, make necessary the use of a simple tool as the Amsler grid [49]–[52]. This instrument is an excellent manner to diagnose AMD, but mainly, it helps in the monitoring of the progression of this disease. The grid was introduced in 1947 by Marc Amsler, and it is described as a *10 cm by 10 cm* square arrangement of white horizontal and vertical lines on a black background. The grid contains 400 small squares, which means that each of the squares corresponds to 1° to visual angle, thus, it covers 20° of area. The Amsler grid has to be held about 30 cm away from the subject and they are asked to look at the center of the grid, (which generally is marked by a dot) and be aware of the squares in their ‘periphery’. They are then asked if the squares have the same size and shape. The presence of any deformation in the lines, squares or loss of lines, indicates the presence of scotomas, and it means that there is a deformation in the retina. Figure 2-6 shows the Amsler grid as a subject may see a scotoma or metamorphosis.

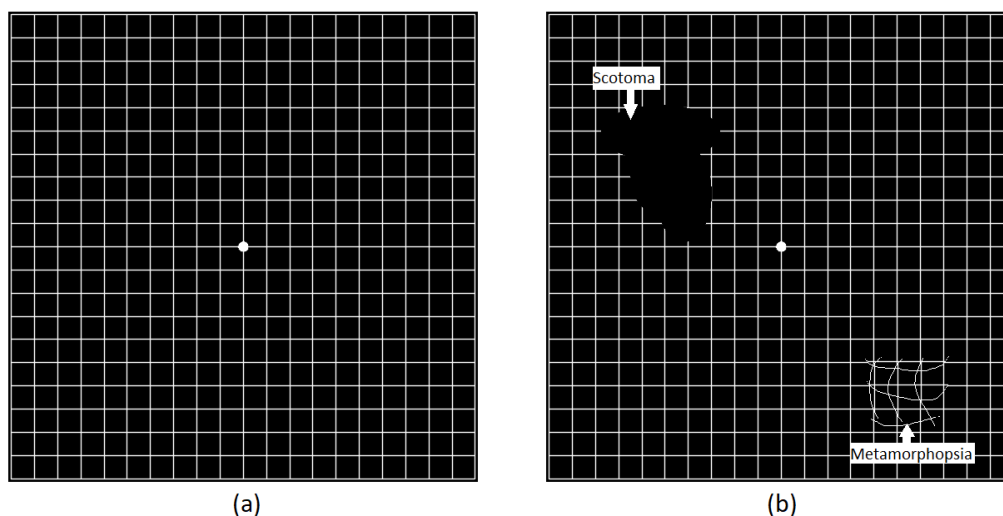


Figure 2-6.- Amsler grid. It is a checkerboard with a square pattern where the patients look at the center and described the missing lines or deformed lines.

2.3 Glaucoma

Glaucoma can be described as a chronic disorder that deteriorates the optic nerve. The progressive optic nerve damage is associated with increased intraocular pressure (IOP), which is dependent on the outflow facility of aqueous humor [53]. Degeneration of the optic nerve starts with visual field defects and can lead to blindness. It is becoming an increasing pathology, with the prediction suggesting that the number of people worldwide will escalate to 79.6 million by next year and the main reason is due to the velocity of the aging population [54]. Figure 2-7 shows the effect of the internal pressure in glaucoma subjects.

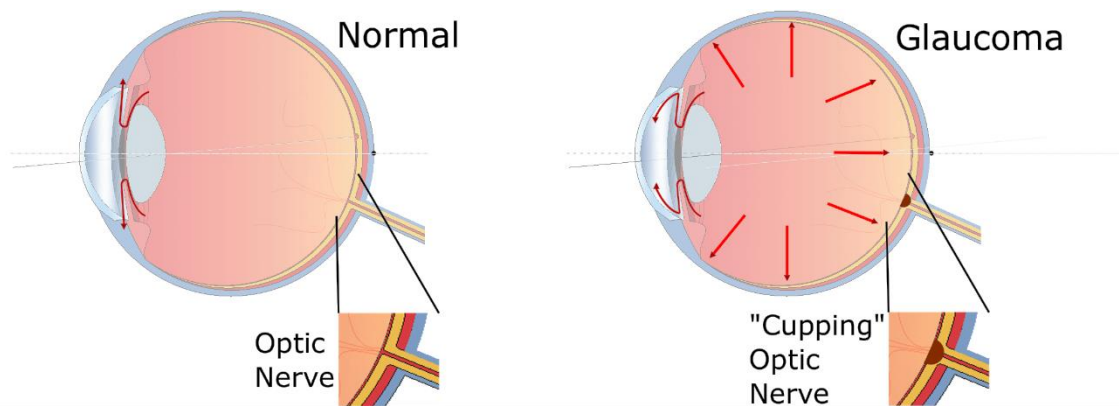


Figure 2-7.- Comparison between a normal and a glaucoma eye.

In order to understand this ocular pathology, it is needed to identify the two main types of glaucoma that exist; primary open-angle glaucoma (OAG) and angle-closure glaucoma (ACG). OAG, the most common form of glaucoma, is characterized by slowly progressive atrophy of the optic nerve and it is painless. Also, in OAG the symptoms start with the visual loss of peripheral visual function. On the other hand, the ACG decreased the vision and usually is an asymptomatic disease.

The epidemiology of glaucoma is determined by several risk factors such as older age, high IOP, ethnic background, family history and high myopia [53], [55]. With this in mind, the available methods to glaucoma diagnosis are focused on the examination of the IOP level, optic nerve head, retinal nerve fiber layer, visual fields, and gonioscopy. It is important to remark that although IOP is considered as the main risk factor, tonometry, a procedure to determine IOP, is not the only method that can be considered to glaucoma

diagnosis. There is evidence that some patients with glaucoma can present a normal range of IOP [56].

As far as treatments are concerned, the only treatment approved is to lower IOP [53], [55]. In this matter, the main option to control IOP is drop therapy, laser therapy, and surgery. The first one is characterized mainly by the application of topical eye drops, although side effects due to the long-term treatment have been reported, such as dry eye [57], [58]. Laser therapy, or laser trabeculoplasty, is the option if the drug treatment is not working on the success of lower the IOP. In some cases, when drugs are not enough as treatment, as well as laser therapy, incisional surgery is the last option.

In this context, the relevance of developing new diagnosis methods and screening techniques becomes important.

2.4 Conclusions

The causes for monochromatic aberrations can be due to several factors such as age, pupil size, accommodation, retinal eccentricity and some pathologies [9]. For example, pupil size has a direct influence on the aberrations of an optical system, and the human eye is not excluded from this. Although, the human pupil, as previously mentioned, is a system that could change the diameter in order to limit the light input, moreover, the pupil diameter decreases during the life span, which can be inferred as a mechanism to decrease the impact of aberrations. Besides the pupil, the lens also can compensate for small amounts of low-order aberrations, as corneal astigmatism, coma, and spherical aberration, which are the main responsible for retinal image degradation. Furthermore, the gradient index of the lens works as a system that optimizes the peripheral optics of the human eye.

As it has been shown, the human eye is not a perfect optical system, moreover, due to that it is not a centered optical system, this is not perfectly aligned, but there are some compensatory mechanisms. Examples of this are the work that the cornea and lens developed together to decrease the aberrations, and the neural mechanism as well.

Chapter 3 - Zonal Wavefront Reconstruction with Square Cells

The previous chapter established some theory about wavefront retrieval definitions, techniques and Hartmann and Shack-Hartmann Sensor tests. In the case of wavefront retrieval techniques, they present different advantages and disadvantages. However, the main disadvantage occurs when small and strong extent irregularities are presented.

In this chapter, a novel zonal method to integrate the transverse aberrations from a square array is presented with the advantage that this method permits the detection of localized errors that can be described. Additionally, with this technique, a different analytical polynomial for each square cell formed by four sampling points from a square array is found. It means that a single one analytical expression for a wavefront is not obtained, and it allows that small localized errors can be described since each square cell is defined by a polynomial. Moreover, each of the expressions is obtained in an exact manner, which is one advantage of this method over the widely used trapezoidal integration.

3.1 Wavefront Considerations

Several Hartmann screen patterns have been developed with the purpose of improving the sampling of the wavefronts and consequently, to enhance the wavefront reconstruction. Three of the most common Hartmann screen patterns are the triangular, square and hexagonal, Fig. 3-1. Each one of these patterns was developed with the aim to cover the whole pupil of the optical system, but, sometimes a higher sampling wavefront demands more time for data analysis or produces an accumulative error.

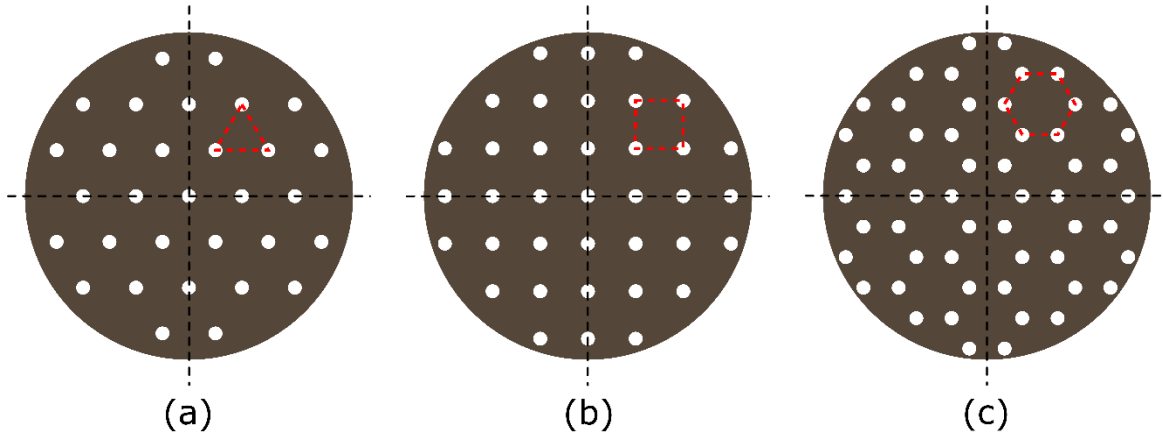


Figure 3-1.- Three possible Hartmann screen patterns. (a) Triangles. (b) Squares. (c) Hexagons.

From the three-screen patterns shown in Fig. 3-1, the simplest one is the square pattern, and it has the advantage that in an exact manner, the spherical power and the astigmatism components can be calculated. As Fig. 3-1(b) shows, if a wavefront is sampled by a square array and is subdivided by squares cells, it means that there are eight data numbers (two slopes at each corner) per squares. With eight data available, it is possible to obtain a wavefront represented by five aberrations, i.e., the tilts, two curvatures, and astigmatism, as shown by Malacara-Hernández [59]. Although, it was found that a more accurate solution could be found by using a least-square adjustment as the proposed method in this thesis described.

If a wavefront is sensed using a Shack-Hartmann sensor with a square pattern, eight number data are obtained: the four slopes and their directions. However, there is a consideration, the eight data are not independent. Malacara-Hernández [60] described the case when four sampling points are equidistantly distributed in a circle, the available information is enough to find an accurate solution for five aberrations, and the wavefront aberrations inside a square cell can be described using the terms in Table 1.2, by

$$W(\rho, \theta) = A_1 \rho \cos \theta + A_2 \rho \sin \theta + A_3 \rho^2 + A_4 \rho^2 \cos 2\theta + A_5 \rho^2 \sin 2\theta \quad (3.1)$$

Tilt in two directions, defocus and astigmatism, with its axis orientation, can be obtained, but, the constant term is not possible to get with this method as Gantes-Nuñez *et. al.* [61] described. It is important to remark that these five coefficients are different for each cell. Also, the high spatial frequencies are missed since a single polynomial function

is not defined, but the spatial frequency limitation by the density of sampling points remains.

On the other hand, if spherical and astigmatism terms are separated in Eq. 3.1, this expression can be written for use in ophthalmic instruments as

$$W(\rho, \theta) = A_1 \rho \cos \theta + A_2 \rho \sin \theta + \left(A_3 - (A_4^2 + A_5^2)^{1/2} \right) \rho^2 + 2(A_4^2 + A_5^2)^{1/2} \rho^2 \sin^2(\theta - \phi) \quad (3.2)$$

where

$$\tan 2\phi = \frac{A_5}{A_4} \quad (3.3)$$

3.2 Sampling and Identification of Point Distribution in a Square Pattern

A circular pupil is the most common pupil of an optical system mainly because of the rotational symmetry, which in some cases, is easier to analyze. A circular pupil can be identified as two possible square screen patterns as Fig. 3-2 illustrates, (a) a sampling point placed at the center of the pupil and (b) a square cell centered at the center of the pupil.

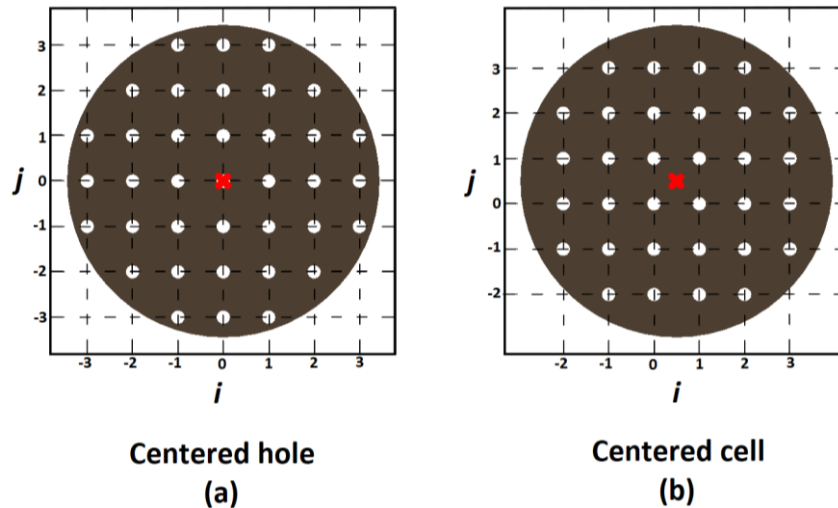


Figure 3-2.- Square screen patterns placed in a pupil with a diameter D , which is divided into cells with size s . (a) A sampling point is centered at the center of the pupil and (b) a square cell is centered.

Because of symmetry convenience, we take a sampling point as the Cartesian coordinate, as Fig. 3-2(a) shows.

Considering D the optical system pupil diameter and d as the aperture diameter, or lenslet diameter, in which the holes are placed at the vertices of the square cells, we can define the size of the cells. If the value ρ is defined as ρ_0 at the corners of the cells and taking the center of these as the origin, the size s of the cells can be derived from Fig. 3-3 by $s = \sqrt{2}\rho_0$.

$$s = \sqrt{2}\rho_0 \quad (3.4)$$

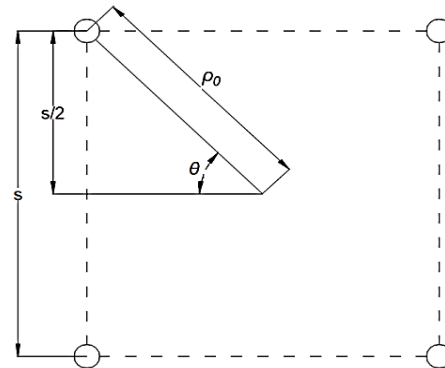


Figure 3-3.- Square cell parameters to design the square screen patterns.

From Fig. 3-3 it can be understood that the transverse aberrations are measured from the light beams passing through the apertures or lenslets positioned at the square cell vertices.

To identify the sampling points in the Hartmann screen, the position of these will be represented by a pair of indices (i, j) , with the coordinate system origin at the center of the pupil as was previously explained. It means that the sampling point at the pupil center has indices $i = j = 0$. Then, the coordinates (x, y) for the sampling points in the Hartmann screen can be either

$$\begin{aligned} x_i &= is \\ y_j &= js \end{aligned} \quad (3.5)$$

A condition related to the position and the number of sampling points along a horizontal and vertical semi-diameter, N , has to be established in order that these have to be inside the circular pupil. Thus, the condition is

$$x_i^2 + y_j^2 < \left(\frac{D-d}{2} \right)^2 \quad (3.6)$$

where D and d were previously defined as the diameters of the pupil and the apertures in the Hartmann screen, respectively. Henceforth, we have

$$i^2 + j^2 < \left(\frac{D-d}{2s} \right)^2 \quad (3.7)$$

Equation 3.7 has to be considered when a Hartmann screen is designed according to ensure that the sampling points are confined in the circular pupil. Now, given a value of the parameter j , the i allowed values can be defined by

$$|i| < \left[\left(\frac{D-d}{2s} \right)^2 - j^2 \right]^{1/2} \quad (3.8)$$

Before, N was defined as the maximum value of the magnitude of i at the horizontal pupil diameter, $j = 0$, it would be given by

$$|i| = N < \left(\frac{D-d}{2s} \right) \quad (3.9)$$

Once the Hartmann screen was designed and Hartmann plate generated, the next step is to measure the transverse aberrations. After transverse aberrations have been measured, it is necessary to label the sampling points with the coordinates defined by Eq. 3.7. Then, the next step is to associate each one of the spots from the Hartmann plate to the matching aperture in the Hartmann screen. This process can be visually or automatically accomplished.

It is common to refer the transverse aberrations to the optical axis of the optical system as Fig. 3-4(a) illustrates, bearing in mind that a sphere with the center of curvature is located at the intersection of the optical axis with the observation plane that has been used as a reference sphere. Nevertheless, using this reference sphere generates a

wavefront retrieved with a large defocus; in fact, to obtain a wavefront without defocusing, the wavefront deformations have to be used a sphere closer to the measured wavefront. Using a sphere closer to the measured wavefront, the transverse aberrations may be obtained with respect to the corners of a square array in the Hartmann plane as is shown in Fig. 3-4(b). From Fig. 3-4(b) is clear that the corners are the ideal positions for the spots of a wavefront without aberrations and only defocusing is present. There is a specific case where a perfect spherical wavefront is tested and the spots will be located at the corners of the square reference only if the square array is modified as Fig. 3-4(c) exemplifies.

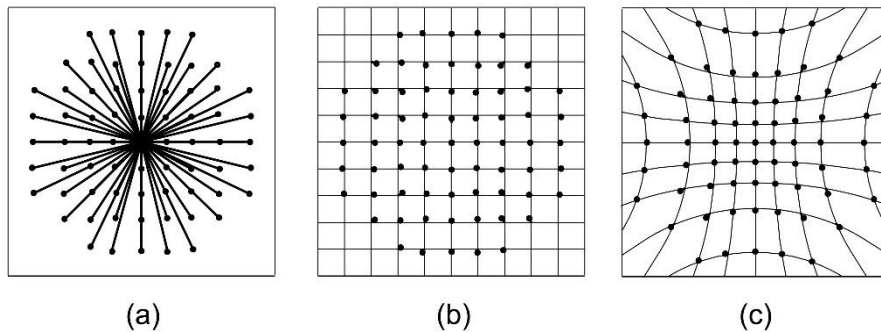


Figure 3-4.- Transverse aberrations measurements with different reference spheres. (a) From the optical axis. (b) Square pattern, closer sphere, used as a reference and (c) reference square array in presence of spherical aberration.

In this work, the reference to measure the transverse aberrations is illustrated in Fig. 3-4(b), so, in subsequent paragraphs is explained how can be constructed the array of square references.

To build the reference grid, the first value to define is the size of the square, which can be computed as the average separation between two consecutive spots. The separation can be considered in the horizontal or vertical direction from the Hartmann pattern. But, to know the separation between two consecutive spots, the spots density in the Hartmann pattern has to be estimated.

For the circular pupil considered in this work, the next equation was used to calculate the average spot density as the relation between the total linear spots number

in the Hartmann pattern, N_T , and the maximum value of ρ , ρ_{\max} , whose is the semi-diameter of a circle containing all of the spots.

$$\text{Spots per unit area} = \frac{N_T}{\pi \rho_{\max}^2} \quad (3.10)$$

To estimate the size of the circle containing the spots, it is necessary to know the distance from the centroid of all spots to the farthest spot from the center of the Hartmann pattern. Hence, the spot separation, σ , along the x or y axis is given by

$$\sigma = \sqrt{\frac{\pi}{N_T} \rho_{\max}^2} \quad (3.11)$$

so, σ value is the separation between lines to be used to build the reference grid.

This reference grid indicates, at the crossings, the ideal coordinates for the spots in the absence of aberrations. They will be named reference points in this work. As stated before, these points have to be labeled in order to identify their position and apply the proposed method. The indices i and j can take N as a maximum value along the vertical or horizontal direction. Hence, the reference grid will be made by $(2N+1) \times (2N+1)$ points. In this case, the reference transverse aberration TA_{rx} and TA_{ry} for the reference points are given by

$$\begin{aligned} TA_{rx} &= i\sigma \\ TA_{ry} &= j\sigma \end{aligned} \quad (3.12)$$

Then, the subsequent step is to associate the identified spots in the Hartmann spot with the closest reference point. To do that, the following equations can be used

$$(TA_x - TA_{rx})^2 + (TA_y - TA_{ry})^2 < \frac{\sigma^2}{2}$$

or

$$(3.13)$$

$$(TA_x - i\sigma)^2 + (TA_y - j\sigma)^2 < \frac{\sigma^2}{2}$$

From Fig. 3-4(b) can be understood that as there could be values in the reference grid that are actually not needed; this is due to the fact that a circular pupil is analyzed

and there are reference points out of the area defined by the pupil. We defined the value $\varepsilon(i, j)=1$ to the reference points that have a corresponding sampling point and a value $\varepsilon(i, j)=0$ to indicate the spots that are not present since there is no sampling point assigned to the reference spot. Now, the value ε works as an indicator to determine if a point is to be taken as a valid point in the wavefront reconstruction method or not, so, it will be possible to build a table with the values (i, j, ε) .

After all the spots were identified, the transverse aberrations can be labeled to their corresponding (i, j) coordinates, making it possible for the construction of a reference table with (i, j, TA_x, TA_y) values. Then, to consider a valid square cell (i, j) , it means there have to be four sampling points forming a square, there is a condition that has to be considered in this address

$$\eta(i, j) = \varepsilon(i, j) \cdot \varepsilon(i+1, j) \cdot \varepsilon(i+1, j+1) \cdot \varepsilon(i, j+1) \quad (3.14)$$

if a sampling point is not present, the value of $\eta(i, j)=0$.

3.3 Wavefront Retrieval in a Square Cell

The previous section explained some considerations to design a reference grid in order to obtain the transverse aberrations values. In addition, in section 3.1 the way to cover the circular pupil with a square pattern was described. From the 3.1 section, it can understand that after the circular pupil has been covered and from Fig. 3-1(b), in the edge of the pupil some triangular cells can be formed, but, as in a previous work was described [60], with 3 points only A_1 , A_2 and A_3 coefficients, corresponding to tilts and defocusing aberrations, can be determined. With four points is possible to determine the wavefront tilt coefficients A_1 and A_2 , the defocus term A_3 , and the astigmatism terms A_4 and A_5 due to there is enough information. In this work, square cells were considered to cover the pupil as much as possible and triangular cells were not used.

3.3.1 Aberration Coefficients Calculation

If Eq. 3.1 is derived with respect to ρ and θ , the transverse aberrations in polar coordinates are given by

$$\begin{aligned} TA_\rho &= -r_w \frac{\partial W(\rho, \theta)}{\partial \rho} = -r_w (A_1 \cos \theta + A_2 \sin \theta + 2A_3 \rho + 2A_4 \rho \cos 2\theta + 2A_5 \rho \sin 2\theta) \\ TA_\theta &= -\frac{r_w}{\rho} \frac{\partial W(\rho, \theta)}{\partial \theta} = -r_w (-A_1 \sin \theta + A_2 \cos \theta - 2A_4 \rho \sin 2\theta + 2A_5 \rho \cos 2\theta) \end{aligned} \quad (3.15)$$

Now, the relation between the transverse aberrations in polar coordinates and Cartesian coordinates is defined by

$$\begin{aligned} TA_x &= TA_\rho \cos \theta - TA_\theta \sin \theta \\ TA_y &= TA_\rho \sin \theta + TA_\theta \cos \theta \end{aligned} \quad (3.16)$$

Applying Eq. 3.3 for every Hartmann plate spot and using some trigonometric identities, it is possible to use the least-squares fitting described by Malacara-Hernández [60] with the purpose of aberration coefficients calculation. Thus, defining an error function ν for a cell with four sampling points as

$$\begin{aligned} \nu &= \sum_{n=1}^4 \left[(TA_\rho - TA'_\rho)^2 + (TA_\theta - TA'_\theta)^2 \right] \\ &= r_w^2 \sum_{n=1}^4 \left[\left(\frac{\partial W(\rho, \theta)}{\partial \rho} + \frac{TA'_\rho}{r_w} \right)^2 + \left(\frac{1}{\rho} \frac{\partial W(\rho, \theta)}{\partial \theta} + \frac{TA'_\theta}{r_w} \right)^2 \right] \end{aligned} \quad (3.17)$$

r_w value is closely constant, nearly equal to the distance from the exit pupil to the observation plane. Also, the use of primes is to indicate that these values are measured data and not variables. Hence, the partial derivatives of error function have to be performed with respect to the coefficients A_k , where $k = 5$ for the case of square cell and these partial derivatives have to be equaled to zero

$$\frac{\partial v}{\partial A_k} = r_w^2 \sum_{n=1}^4 \left[\left(\frac{\partial W(\rho, \theta)}{\partial \rho} + \frac{TA'_\rho}{r_w} \right)^2 \frac{\partial^2 W(\rho, \theta)}{\partial A_k \partial \rho} + \left(\frac{1}{\rho} \frac{\partial W(\rho, \theta)}{\partial \theta} + \frac{TA'_\theta}{r_w} \right)^2 \frac{\partial^2 W(\rho, \theta)}{\partial A_k \partial \theta} \right] = 0 \quad (3.18)$$

As a result, substituting Eq. 2.15 in the error function v

$$v = r_w^2 \sum_{n=1}^4 \left[\left(A_1 \cos \theta + A_2 \sin \theta + 2A_3 \rho + 2A_4 \rho \cos 2\theta + A_5 \rho \sin 2\theta + \frac{TA'_\rho}{r_w} \right)^2 + \left(-A_1 \sin \theta + A_2 \cos \theta - 2A_4 \rho \sin 2\theta + 2A_5 \rho \cos 2\theta + \frac{TA'_\theta}{r_w} \right)^2 \right] \quad (3.19)$$

The next step is to obtain the derivatives of these functions with respect to each one of the five unknown coefficients $A_k = 0$

$$-\frac{1}{r_w} \sum_{n=1}^4 [TA'_\rho \cos \theta - TA'_\theta \sin \theta] = \sum_{n=1}^4 \left[\begin{array}{l} (A_1 \cos \theta + A_2 \sin \theta + 2A_3 \rho + 2A_4 \rho \cos 2\theta + 2A_5 \rho \sin 2\theta) \cos \theta \\ -(-A_1 \sin \theta + A_2 \cos \theta - 2A_4 \rho \sin 2\theta + 2A_5 \rho \cos 2\theta) \sin \theta \end{array} \right] \quad (3.20)$$

$$-\frac{1}{r_w} \sum_{n=1}^4 [TA'_\rho \sin \theta + TA'_\theta \cos \theta] = \sum_{n=1}^4 \left[\begin{array}{l} (A_1 \cos \theta + A_2 \sin \theta + 2A_3 \rho + 2A_4 \rho \cos 2\theta + 2A_5 \rho \sin 2\theta) \sin \theta \\ +(-A_1 \sin \theta + A_2 \cos \theta - 2A_4 \rho \sin 2\theta + 2A_5 \rho \cos 2\theta) \cos \theta \end{array} \right] \quad (3.21)$$

$$-\frac{1}{r_w} \sum_{n=1}^4 [TA'_\rho] = \sum_{n=1}^4 [(A_1 \cos \theta + A_2 \sin \theta + 2A_3 \rho + 2A_4 \rho \cos 2\theta + 2A_5 \rho \sin 2\theta)] \quad (3.22)$$

$$-\frac{1}{r_w} \sum_{n=1}^4 [TA'_\rho \cos 2\theta - TA'_\theta \sin 2\theta] = \sum_{n=1}^4 \left[\begin{array}{l} (A_1 \cos \theta + A_2 \sin \theta + 2A_3 \rho + 2A_4 \rho \cos 2\theta + 2A_5 \rho \sin 2\theta) \cos 2\theta \\ -(-A_1 \sin \theta + A_2 \cos \theta - 2A_4 \rho \sin 2\theta + 2A_5 \rho \cos 2\theta) \sin 2\theta \end{array} \right] \quad (3.23)$$

$$-\frac{1}{r_w} \sum_{n=1}^4 [TA'_\rho \sin 2\theta + TA'_\theta \cos 2\theta] = \sum_{n=1}^4 \left[\begin{array}{l} (A_1 \cos \theta + A_2 \sin \theta + 2A_3 \rho + 2A_4 \rho \cos 2\theta + 2A_5 \rho \sin 2\theta) \sin 2\theta \\ +(-A_1 \sin \theta + A_2 \cos \theta - 2A_4 \rho \sin 2\theta + 2A_5 \rho \cos 2\theta) \cos 2\theta \end{array} \right] \quad (3.24)$$

After some algebraic steps and writing the above expressions in terms of the multiple angle, $\sin n\theta$ and $\cos n\theta$, we obtain

$$-\frac{1}{r_w} \sum_{n=1}^4 [TA'_\rho \cos \theta - TA'_\theta \sin \theta] = 4A_1 + 2A_3 \rho \sum_{n=1}^4 \cos \theta + 2A_4 \rho \sum_{n=1}^4 \cos \theta + 2A_5 \rho \sum_{n=1}^4 \sin \theta \quad (3.25)$$

$$-\frac{1}{r_w} \sum_{n=1}^4 [TA'_\rho \sin \theta + TA'_\theta \cos \theta] = 4A_2 + 2A_3 \rho \sum_{n=1}^4 \sin \theta - 2A_4 \rho \sum_{n=1}^4 \sin \theta + 2A_5 \rho \sum_{n=1}^4 \cos \theta \quad (3.26)$$

$$-\frac{1}{r_w} \sum_{n=1}^4 [TA'_\rho] = A_1 \sum_{n=1}^4 \cos \theta + A_2 \sum_{n=1}^4 \sin \theta + 8A_3 \rho + 2A_4 \rho \sum_{n=1}^4 \cos 2\theta + 2A_5 \rho \sum_{n=1}^4 \sin \theta \quad (3.27)$$

$$-\frac{1}{r_w} \sum_{n=1}^4 [TA'_\rho \cos 2\theta - TA'_\theta \sin 2\theta] = A_1 \sum_{n=1}^4 \cos \theta - A_2 \sum_{n=1}^4 \sin \theta + 2A_3 \rho \sum_{n=1}^4 \cos \theta + 8A_4 \rho \quad (3.28)$$

$$-\frac{1}{r_w} \sum_{n=1}^4 [TA'_\rho \sin 2\theta + TA'_\theta \cos 2\theta] = A_1 \sum_{n=1}^4 \sin \theta + A_2 \sum_{n=1}^4 \cos \theta + 2A_3 \rho \sum_{n=1}^4 \sin 2\theta + 8A_5 \rho \quad (3.29)$$

With the assumption that the sampling points are distributed in a regular angular manner, to calculate the matrix elements can be easily proved by using the following expressions

$$\begin{aligned} \sum_{n=1}^4 \sin M\theta &= (4 \sin \theta_0) \delta_{M,4} \\ \sum_{n=1}^4 \cos M\theta &= (4 \cos \theta_0) \delta_{M,4} \end{aligned} \quad (3.30)$$

where θ_0 correspond to the first sampling point in the square cell, starting counterclockwise as Fig. 3-5 illustrates and M is the harmonic component number, where

$$\delta_{M,4} = \begin{cases} 0 & \text{if } M \neq 4 \\ 1 & \text{if } M = 4k \end{cases} \quad (3.31)$$

and k is an integer. Then, using the Nyquist-Shannon sampling theorem [62]

$$\begin{aligned} \sum_{n=1}^4 \sin M\theta &= 0 \\ \sum_{n=1}^4 \cos M\theta &= 0 \end{aligned} \quad (3.32)$$

for all the values of M .

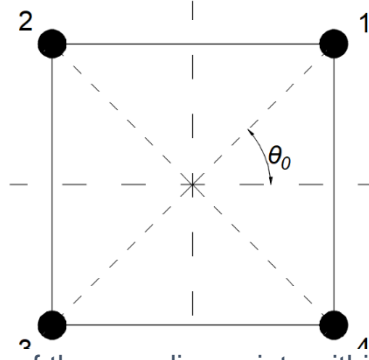


Figure 3-5.- Labels of the sampling points within the square cell with an angle θ_0 .

Using these results in Eqs. (3.25-3.29), the aberration coefficients are obtained as

$$A_1 = -\frac{1}{4r_w} \sum_{n=1}^4 [TA'_{\rho n} \cos \theta_n - TA'_{\theta n} \sin \theta_n] = -\frac{1}{4r_w} \sum_{n=1}^4 [TA'_{x n}] \quad (3.33)$$

$$A_2 = -\frac{1}{4r_w} \sum_{n=1}^4 [TA'_{\rho n} \sin \theta_n + TA'_{\theta n} \cos \theta_n] = -\frac{1}{4r_w} \sum_{n=1}^4 [TA'_{y n}] \quad (3.34)$$

$$A_3 = -\frac{1}{8\rho_0 r_w} \sum_{n=1}^4 [TA'_{\rho n}] = -\frac{1}{8\rho_0 r_w} \sum_{n=1}^4 [TA'_{x n} \cos \theta_n + TA'_{y n} \sin \theta_n] \quad (3.35)$$

$$A_4 = -\frac{1}{8\rho_0 r_w} \sum_{n=1}^4 [TA'_{\rho n} \cos 2\theta_n - TA'_{\theta n} \sin 2\theta_n] = -\frac{1}{8\rho_0 r_w} \sum_{n=1}^4 [TA'_{x n} \cos \theta_n - TA'_{y n} \sin \theta_n] \quad (3.36)$$

$$A_5 = -\frac{1}{8\rho_0 r_w} \sum_{n=1}^4 [TA'_{\rho n} \sin 2\theta_n + TA'_{\theta n} \cos 2\theta_n] = -\frac{1}{8\rho_0 r_w} \sum_{n=1}^4 [TA'_{x n} \sin \theta_n + TA'_{y n} \cos \theta_n] \quad (3.37)$$

where ρ_0 is the distance from the center to the corners of the square cell.

Then, substituting the coordinates for the four sampling points at the corners of the square cell and considering the cell center as the origin, Fig. 3-5

$$A_1 = -\frac{1}{4r_w} [TA'_{x1} + TA'_{x2} + TA'_{x3} + TA'_{x4}] \quad (3.38)$$

$$A_2 = -\frac{1}{4r_w} [TA'_{y1} + TA'_{y2} + TA'_{y3} + TA'_{y4}] \quad (3.39)$$

$$A_3 = -\frac{1}{8sr_w} \begin{bmatrix} TA'_{x1} + TA'_{y1} - TA'_{x2} + TA'_{y2} \\ -TA'_{x3} - TA'_{y3} + TA'_{x4} - TA'_{y4} \end{bmatrix} \quad (3.40)$$

$$A_4 = -\frac{1}{8sr_w} \begin{bmatrix} TA'_{x1} - TA'_{y1} - TA'_{x2} - TA'_{y2} \\ -TA'_{x3} + TA'_{y3} + TA'_{x4} + TA'_{y4} \end{bmatrix} \quad (3.41)$$

$$A_5 = -\frac{1}{8sr_w} \begin{bmatrix} TA'_{x1} + TA'_{y1} + TA'_{x2} - TA'_{y2} \\ -TA'_{x3} - TA'_{y3} - TA'_{x4} + TA'_{y4} \end{bmatrix} \quad (3.42)$$

With this method, the piston term is lost in the retrieved wavefront, but the appropriate piston term can be later recovered.

As was demonstrated, with a square cell is possible to describe the wavefront deformation, in an exact manner, by five aberration terms, *i.e.*, two tilts, the defocus, and two primary astigmatism terms. It is important to mention that the transverse aberration coefficients are defined by the vertices of a square cell.

3.3.2 Calculation of the Aberration Values Inside Each Square Cell

Equation 3.1 written in Cartesian coordinates has the form of

$$w_{kl}(x, y) = A_1(i, j)x + A_2(i, j)y + A_3(i, j)(x^2 + y^2) + A_4(i, j)(x^2 - y^2) + 2A_5(i, j)xy \quad (3.43)$$

Using Eq. 3.43 and once the aberration coefficients values were calculated with Eqs. (3.38-3.42), the wavefront deformations values, $w_{ij}(x, y)$, can be found if this equation is evaluated at several points inside each square cell, as Fig. 3-6 illustrates.

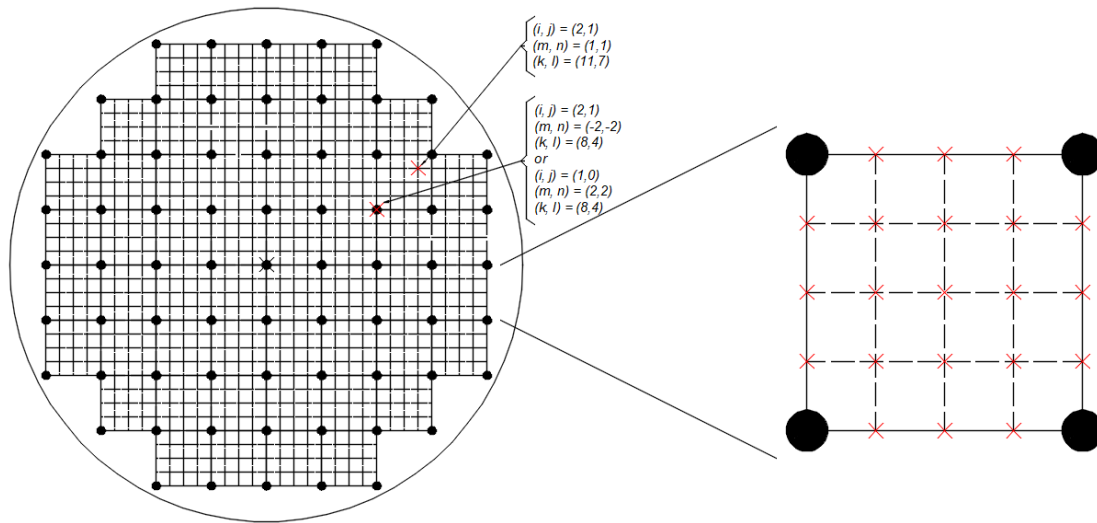


Figure 3-6.- Square cells pattern with points inside them to evaluate the wavefront deformations. Also, subscripts (i, j) , (m, n) and (k, l) are shown. The (i, j) values are the position of the sampling point, represented by black circles, and they are the position of the cell as well; so, the location of the cell is represented by the lower-left corner sampling point. (m, n) coordinates are the positions of the inner points for each one of the cells, with the cell center as the origin. For the case of (k, l) values, they are coordinates with reference at the pupil center.

The piston term A_0 is excluded because the origin of the coordinates (x, y) is taken at the center of the square cells.

Now, since the final objective is to construct the whole wavefront, some points were defined inside of square cells to do interpolation and make possible to obtain a more regular wavefront. These values are defined by (n, m) with m and $n = -2, -1, 0, 1, 2$, and they are related to the x and y coordinates by

$$\begin{aligned} x &= \frac{ns}{4} \\ y &= \frac{ms}{4} \end{aligned} \tag{3.44}$$

It is important to point out that numbers (n, m) are not the same as those used in Tables 2.1 and 2.2.

After the whole pupil has been covered by square cells, the new points are defined by the subscripts (k, l) , whose origin is placed at the pupil center. Then, once the (i, j) values have been assigned to the cells, the points (k, l) can be defined as

$$\begin{aligned} k &= 4i + m + 2 \\ l &= 4j + n + 2 \end{aligned} \tag{3.45}$$

In Fig. 3-6 there are some examples of the use of these subscripts and the red crosses represent the new points calculated. Consequently, the wavefront values are dependent on i, j, n, m subscripts, $w(i, j, n, m)$ and now is possible to calculate the piston term $A_0(i, j)$, so, the final $W(k, l)$ can be described as follows

$$\begin{aligned} W(k, l) &= W(4i + m + 2, 4j + n + 2) \\ &= w(i, j, m, n) + A_0(i, j) \end{aligned} \tag{3.46}$$

In the next section is explained the manner to calculate the piston term for each square cell in order to obtain a continuous wavefront.

3.3.3 Contiguous Cells Coupling and Wavefront Representations

The piston term can be determined if a process of joining contiguous terms, so, to calculate this coefficient, the wavefront of the square cells that compose it have to be matched at the edges. As can be seen in Fig. 3-6, there are two sampling points shared between two adjacent cells, hence, the slopes at the two vertices between the two joined cells are the same for both cells. Fig. 3-7 describes the similarities between wavefront profiles for the contiguous cells.

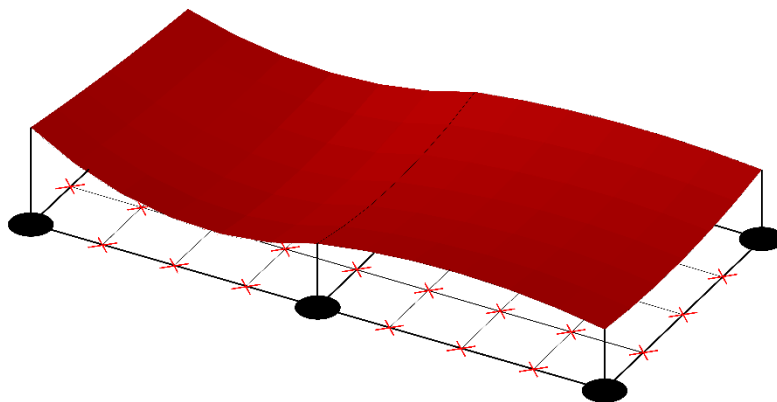


Figure 3-7. - Once the piston term has been optimized, the two contiguous cells coincide along the border; continuous wavefronts, continuous slopes but discontinuous curvatures. Two adjacent wavefronts have the same slopes at the border, thus, they have the same heights, but the second derivative might be different.

In this work, we will refer to filling the empty cells to the method of finding the proper piston term and placing of the wavefront deformation values $w(i, j, m, n)$ in the cell (i, j) .

The first step to fill the vacant cells starts with the lowest row of cells from the pupil and finishing it with the uppermost row of cells. For the case of Fig. 3-6, the procedure starts with the cell $(-2, -4)$ which is located at the lowest row starting from left to right. In that case, this cell is the first one which means that there are no previous values to level it, so, the rest of the cells has to be matched with this cell. The next cell to level will be $(-1, -4)$, then $(0, -4)$ and so on until the cells that are in the lowest row are leveled. However, as can be seen in Fig. 3-6, in the next row, -3 , for the first left column there is no below cell to be equated with.

The previous problem can be handled and solved if the fill and level process is developed in two steps; firstly, filling the right half of the pupil and then the left half. The filling right half process starts in $(0, -4)$ cell, meaning that pupil right half is considered from the coordinate $i = 0$ and continues upward. Once the right half of the pupil has been leveled, the second step is the filling of the left half, starting in $(-1, -4)$ cell.

Leveling in this manner the pupil guarantees a cell with which the next one could be leveled; for the case of going from left to right, an empty cell will always be to the right unless the cell is the first one from a row. If the cell is the first one from a row, there will be a cell below which can be associated. For the case of the left half, this process is developed leveling the cells with the contiguous right cells, which have been filled in the previous step.

To illustrate the process, in Fig. 3-8 are exemplified the manner in which a cell is leveled considered that a cell below and a cell to the left or right is filled as well.

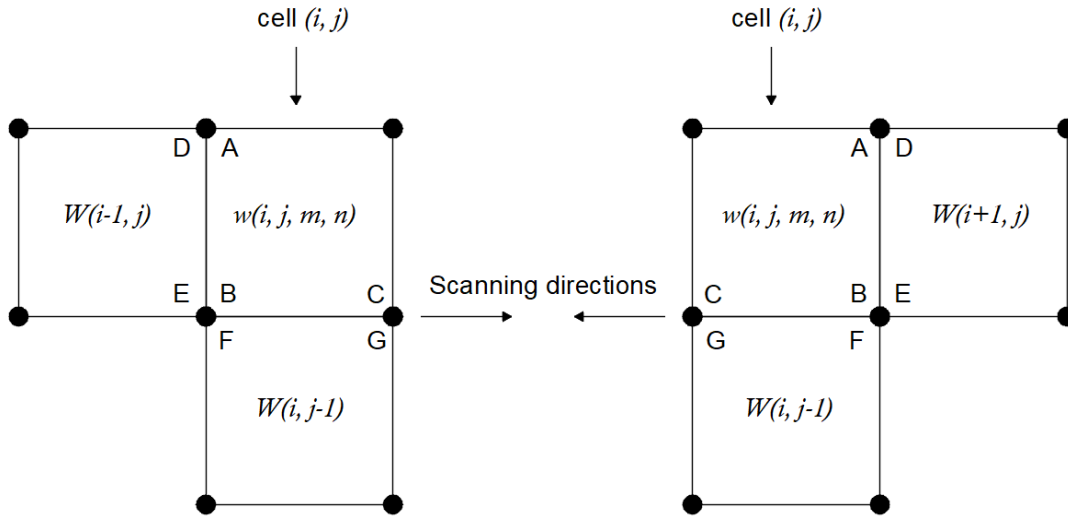


Figure 3-8.- The filling process of (i, j) cells. If the cell (i, j) is on the right, the piston term is obtained by the average of the difference between the left and lower cells. In contrast, if the cell (i, j) is on the left side, the right and lower cells are used.

For a right cell, the piston term is calculated by taking the average of the differences between the points A and D, B and E, B and F, and C and G. The average of the differences is considered due to the fact to increase the accuracy even if the differences should be equal because the elements are sharing the sampling points. Considering the first cell of a row is expected that the points D and E do not exist, thus, the value of $\eta(i, j-1)$, Eq. 3.14, for this cell, is zero and the corresponds differences have to be multiplied by η value. For the case of the left direction, the values of F and G could not exist, and also the values of $\eta(i, j-1)$ is zero. Thus, considering the η value, the function to calculate the piston term A_0 , for the first step, filling from left to right, is

$$A_0(i, j) = \frac{\left\{ \begin{aligned} & [(W(4i, 4j+4) - w(i, j, -2, 2)) + (W(4i, 4j) - w(i, j, -2, -2))] \eta(i-1, j) + \\ & [(W(4i, 4j) - w(i, j, -2, -2)) + (W(4i+4, 4j) - w(i, j, 2, -2))] \eta(i, j-1) \end{aligned} \right\}}{2[\eta(i-1, j) + \eta(i, j-1)]} \quad (3.47)$$

The process of filling the left side of the pupil is similar to the preceding described, but the method starts with the cells in the column $(-1, j)$. As this process is the second step, all the right cells have been filled and leveled, column $i = 0$, and for some cases, the cells from the lower cells are filled as well. Using the same procedure in Eq. 3.47, for the pupil left half the piston term is given by

$$A_0(i, j) = \frac{\left\{ \begin{aligned} & \left[(W(4i+4, 4j+4) - w(i, j, 2, 2)) + (W(4i+4, 4j) - w(i, j, 2, -2)) \right] \eta(i+1, j) + \\ & \left[(W(4i, 4j) - w(i, j, -2, -2)) + (W(4i+4, 4j) - w(i, j, 2, -2)) \right] \eta(i, j-1) \end{aligned} \right\}}{2[\eta(i+1, j) + \eta(i, j-1)]} \quad (3.48)$$

With the described method to level the cells, the wavefront values in the whole pupil have been found, but the piston of the whole pupil is referred to the cell with coordinates $(0, j_{\min})$. It is convenient that the piston value is equal to zero at the center of the wavefront, consequently, the final step of this procedure is to make that the cell $(0, 0)$ has a value of zero. This can be done subtracting the original values of the pupil to all remaining wavefront values. For pupils that do not have a sampling point at the center of the pupil, as in telescope mirror with a central hole, there is no possibility to apply the method.

The first step leveling the right half side of the pupil, the expression to reference the piston term to the central cell is

$$W(x, y) = W(ks, ls) = \sum_{i=0}^N \sum_{j=0}^N \left(\left(\sum_{m=-2+\eta(i-1, j)}^2 \sum_{n=-2+\eta(i, j-1)}^2 w(i, j, m, n) + A_0(i, j) \right) \right) \quad (3.49)$$

where the wavefront deformations $w(i, j, m, n)$ are added to their piston term values previously calculated with Eq. 3.47 and 3.48. Now, for the left side, the expression is given by

$$W(x, y) = W(ks, ls) = \sum_{i=0}^N \sum_{j=0}^N \left(\left(\sum_{m=-2}^{2+\eta(i-1, j)} \sum_{n=-2+\eta(i, j-1)}^2 w(i, j, m, n) + A_0(i, j) \right) \right) \quad (3.50)$$

It is important to remark that the duplicated values of the wavefront deformations at the border for contiguous cells have been eliminated with these equations.

The method described to recover the wavefront using an array of square cells is better than a polynomial fitting (modal reconstruction). Using the polynomial fitting there is the possibility to smooth out many local bumps or valleys, eliminating many real errors, if the wavefront is quite irregular or highly aspheric. In this respect, zonal procedures are a better option if localized errors or high-order aberrations are present. The typical and most used zonal method is trapezoidal integration, so, the results of our proposal are compared with this method.

In order to evaluate the proposed method, a wavefront simulation was built with some arbitrary aberration coefficients to a high-order expression in terms of Zernike polynomials, Table 3.1, as Fig. 3-9 illustrates.

Table 3.1.- Orthonormal Zernike circle polynomial terms used for the simulated wavefront illustrated in Fig. 3-9(a).

Aberration name	j	n	m	$Z_j(\rho, \theta)$	Value ($\times 10^{-3}$)
Defocus	4	2	0	$\sqrt{3}(2\rho^2 - 1)$	0.040
Astigmatism at $\pm 45^\circ$	5	2	2	$\sqrt{6}\rho^2 \sin 2\theta$	0.010
Astigmatism at $\pm 45^\circ$ or $\pm 90^\circ$	6	2	2	$\sqrt{6}\rho^2 \cos 2\theta$	0.020
Triangular astigmatism, $\pm 30^\circ$, $\pm 150^\circ$, $\pm 270^\circ$	9	3	3	$\sqrt{8}\rho^3 \sin 3\theta$	0.030
Triangular astigmatism, $\pm 0^\circ$, $\pm 120^\circ$, $\pm 240^\circ$	10	3	3	$\sqrt{8}\rho^3 \cos 3\theta$	0.030
Pentagonal astigmatism, with peaks at Triangular astigmatism, $s(72^\circ)$	20	5	5	$\sqrt{12}\rho^5 \cos 5\theta$	0.100

A simulated wavefront, Fig. 3-9(a), was selected to show the differences between the proposed method and the well-known trapezoidal method. Using the Zernike polynomials to generate the wavefront simulation, a Hartmann pattern was produced, selecting a Hartmann screen with five points in the right half and five in the left. Also, five points from the top and five from the bottom were chosen to keep a symmetrical sampling pupil. Once the Hartmann pattern was produced, the trapezoidal method was implemented to rebuild the wavefront and the result is shown in Fig. 3-9(b). In the same way, but using the proposed technique, the wavefront was retrieved and is shown in Fig. 3-9(c). The whole pupil was covered by sixty-four cells, and inside of each cell were interpolated four points to plot the wavefront. It can be noted that the wavefront reconstruction with the proposed method is more faithful than the trapezoidal integration method. Also, can be said that another advantage is that the local curvatures can be more easily estimated.

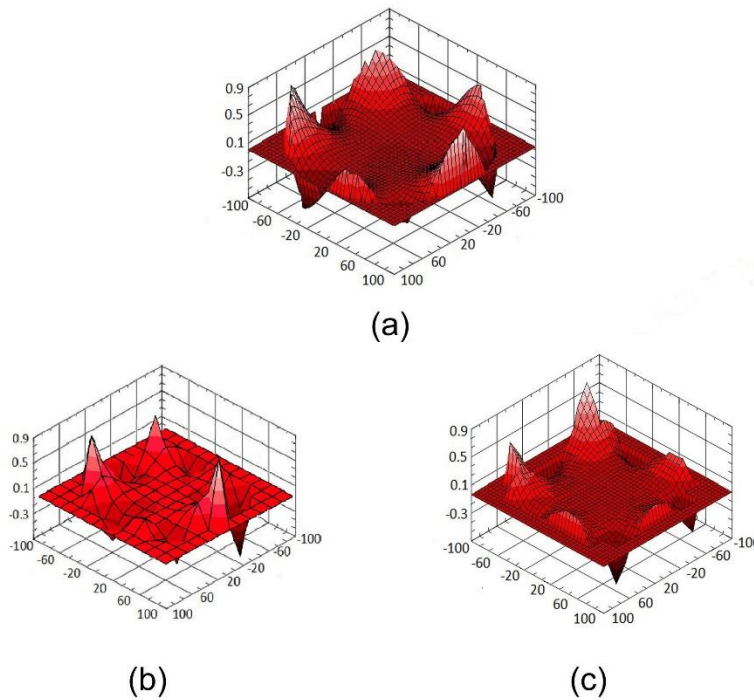


Figure 3-9.- Wavefront simulation using the Zernike polynomials shown in Table 3.1 and the wavefronts reconstruction using trapezoidal integration and the proposed method. (a) Wavefront simulation selecting some arbitrary wavefront coefficients. (b) Wavefront the trapezoidal integration method and (c) wavefront retrieved with the proposed method. [62]

3.4 Conclusions

In this chapter, a method to retrieve the measured wavefront using an array of square cells has been described. This method has the advantage that a polynomial is assigned to each one of the cells that covered the pupil, which contains tilt, curvature, and astigmatism terms. Further, with this procedure, the functions that represent the wavefront of two contiguous cells are continuous, as well as their derivatives (slopes). However, the second derivatives (curvatures) are not continuous in the borders.

For the case of wavefront deformations that strongly departs from a perfect sphere, when high-order aberrations exist in the wavefront, for example, it might not be necessary to implement a procedure to make the curvatures continuous at contiguous cells. Consider that the curvatures of two contiguous cells are different, as is expected for a non-spherical wavefront; in this case, an extra wavefront deformation $w'_{i,j}(x, y)$ can be added to each cell. This extra wavefront deformation would have to satisfy the following conditions, due to the fact that the rest of aberration terms of the wavefront in the square cell cannot be modified:

- (a) The slopes and curvatures at the center of this extra wavefront deformation should be zero in order to not modify the those of the square cells. If the power terms with a value of 1 and 2 in the function $w'_{i,j}(x, y)$ are not present, this condition is achieved.
- (b) In the borders, the wavefront deformations and slopes should not be modified by this extra term.
- (c) The extra term should not alter the curvature at the center of the cell.
- (d) For contiguous cells, the curvature at the borders should be averaged.

Finally, although some errors are appreciated in the edges of the pupil, it is possible to be eliminated if a similar procedure is applied to the triangular cells formed near the edge of the pupil.

Chapter 4 - Zonal Wavefront Reconstruction with Hexagonal Cells

Wavefront retrieval techniques is an interesting research area that has the objective of improving the accuracy of these methods, as well as the wavefront sensing [63]–[72]. The main reason is due to their applications as in the study of human eye and design of freeform surfaces. In the first case, generally, low-aberrations can be measured and corrected in clinical practice; but the difficulty to measure or correct high-order aberrations, such as spherical aberrations and coma, is the reason to continue exploring new measure techniques [73]–[80]. An example of a wavefront reconstruction application can be appreciated in the aberrometer which even now their basic principle of work is based on the common technique of Shack-Hartmann [81]. Visual personalized corrections are the main objective of this kind of equipment.

Evaluation of freeform surfaces is another area with maintained research in wavefront analysis techniques. The inclusion of this kind of element in optical systems due to the fact that the number of elements can be reduced and also the size of the system [82]. The problems with freeform surfaces are fabrication and testing, as well as the cost of manufacturing [82]–[84].

Different geometrical arrays and techniques have been used to sample optical system pupils, such as triangular, square and hexagonal patterns. Each one of these patterns has advantages and disadvantages, but typically, they are limited by the total surface that is covered, especially near the edge of the pupil. In this manner, with the hexagonal pattern is possible to cover in a better way the whole pupil.

This chapter describes a method to integrate Shack-Hartmann and Hartmann patterns in a similar way that the previous chapter, but using hexagonal cells. The polynomial representation obtained from each hexagonal cell allows one to increase the

number of aberrations coefficients that can be calculated. Further, the hexagonal array configuration provides a higher density of spots than in an array of square cells [85]–[87]. Thus, with hexagonal cells is possible to cover more area at the edges than with square cells, so, the local curvatures and low order aberrations in each cell are more accurately obtained than using square cells.

4.1 Design and Implementation of the Hexagonal Hartmann Pattern

In the previous chapter, it was said that the square array is the simplest geometrical array to sample an optical pupil from the Hartmann test, but, working with this distribution, only five aberration coefficients can be obtained. Instead, although hexagonal array is more complicated to analyze, the number of aberrations coefficients is higher than square geometry. Using hexagonal cells, an exact analytical expression is generated for each cell, as in square cell, but for this case, we obtain twelve data points, two slopes at each vertex. Thus, in the hexagonal cell is possible to obtain four aberration coefficients, coma aberrations, and triangular astigmatisms, plus those found with the square cell.

Due to the geometry of hexagonal pattern, there are two possible sampling points' distributions, at the center of the cell or at the vertices of a hexagon; though, with the second configuration, there is a higher sampling density. In this work, it is used with the configuration where the sampling points at the vertices, so, a hexagonal cell is placed with the center at the pupil center as Fig. 3-1 illustrates. Using this set up it is possible to infer that if a sampling point were added at the center of the hexagon, the analysis would have to be considered a triangular one. Hence, in this work is presented an analysis to design the distribution of the openings in the hexagonal array.

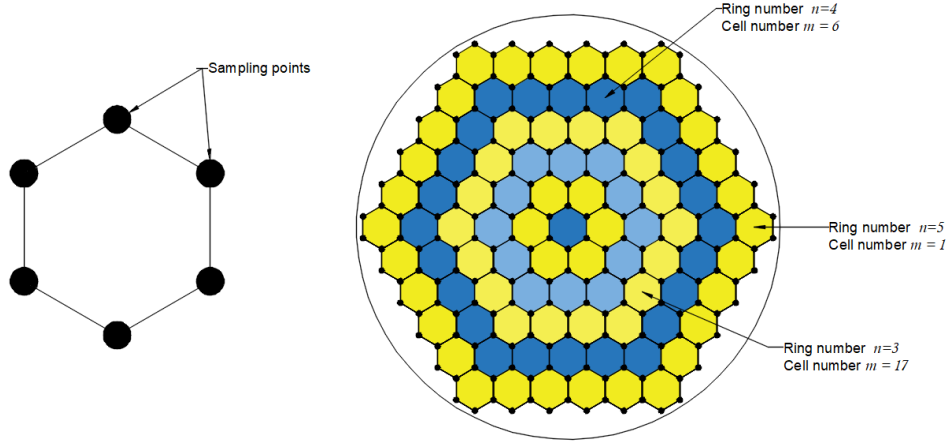


Figure 4-1.- Hexagonal cell with sampling points at vertices and coordinate numbers for a hexagonal cell in a hexagonal array.

To perform the integration process is necessary to identify the hexagonal cells, so, the position of each cell within the whole cell array in the circular pupil is described by a pair of numbers. The first number is defined as n and indicates the ring number, in Fig. 4-1 the rings are colored with a specific color, where $n=0$ to N . Central cell is the ring number zero, $n=0$. Each one of the rings has n hexagonal cells on each side, it means that the total number of cells in a ring is $6n$. Then, the second number used to identify the location of a cell is defined as m , which indicates the cell number in the ring, starting with $m=1$ on the right side, and the maximum number of cells in the ring is $m=6n$. These pairs of numbers can be observed clearly in Fig. 4-1.

Now, to design the Hartmann screen the size of each hexagonal cell has to be determined considering the side length, s , or the apothem a , associated by

$$a = \frac{\sqrt{3}}{2} s \quad (4.1)$$

Also, an auxiliary parameter k is defined in order to identify the side number for the hexagonal ring. It starts on the first side at the right and on the upper part of the pupil. Once the parameter n and m have been defined, with m beginning at the x axis and increasing its value in a counter-clockwise direction, the k value is given by

$$k = \text{int} \left[\frac{m-1}{n-1} \right] + 1 \quad (4.2)$$

where int is the non-rounded integer value.

With the k parameter definition, a better manner to enumerate the cells can be used in order to identify the side in which the cell is placed. Instead of number m , a number m'_k is utilized, with the main difference that m number starts at the first hexagonal cell of the whole hexagonal ring and m'_k has its origin at the first cell of the side k . Fig. 4-2 illustrates the use of this parameter as well as θ and θ'_k which are referred to as the angle formed by the cells.

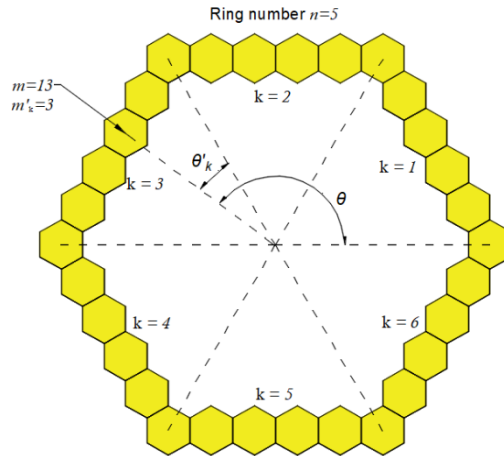


Figure 4-2.- Interpretation of the values θ_0 and m , and angles m'_k and θ .

As can be seen in Fig. 4-2, a triangle is formed between the first cell of a k side, a selected cell m'_k , and the pupil center. Fig. 4-3 shows an example of a triangle-shaped by the anterior elements.

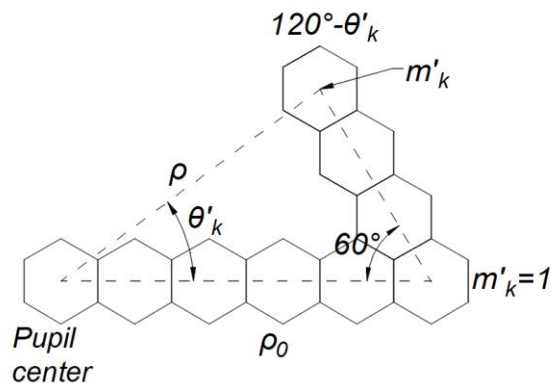


Figure 4-3.- Triangle shaped by the pupil center, a selected cell and the first cell of a ring.

In Fig. 4-3 can be observed two new parameters, ρ value is formed by the distance between the pupil center to the cell m'_k and the ρ_0 value is considered from the center of the pupil to the cell at the beginning of the line k .

For the case of the hexagon, the side size is equal to the circumradius, which is the distance from the center to any one of its vertex. Following the description of Fig 4-3, the ρ_0 value can be given by

$$\rho_0 = 2(n-1)a = \sqrt{3}(n-1)s \quad (4.3)$$

where s is the side and a is the apothem of the cells. Now, the value of m'_k can be obtained as follow

$$m'_k = m - (k-1)(n-1) \quad (4.4)$$

With these values defined, the distance from the beginning of the line k for a hexagonal ring n to the cell m'_k is

$$2(m'_k-1)a = \sqrt{3}(m'_k-1)s \quad (4.5)$$

Then, the value of ρ can be found using the trigonometric *cosine* law and from Fig. 4-3

$$\rho^2 = 3(n-1)^2 s^2 + 3(m'_k-1)^2 s^2 - 6(n-1)(m'_k-1)s^2 \cos(60^\circ) \quad (4.6)$$

or

$$\rho = \left(\sqrt{3[(n-1)^2 + (m'_k-1)^2 - (n-1)(m'_k-1)]} \right) s \quad (4.7)$$

Now, if the trigonometric *sine* law is applied to the same triangle we can obtain the angle θ'_k by

$$\sin\theta'_k = \frac{3(m'_k-1)s}{2\rho} \quad (4.8)$$

and the θ value in radians as well can be given by

$$\theta = \theta'_k + \frac{\pi}{3}(k-1) \quad (4.9)$$

These equations were developed in order to find the polar coordinates ρ and θ for a given cell if the values of n and m are specified.

After the considerations to identify the hexagonal cells in a Hartmann plate and size of these, the next step is defining a cell density in the circular pupil. It has been said that the central cell could be considered the ring $n=0$ and each one of the rings has n hexagonal cells, so, the total number of cells in one ring is $6n$. Because of the previous circumstances, in an array with N rings, plus one at the center, the total number of cells, M_c , is given by

$$M_c = 1 + 6(1 + 2 + 3 + \dots + N) = 3(N+1)N + 1 \quad (4.10)$$

Besides the total number of cells, the total number of vertices, M_v , is also important to calculate due to the fact that they are equal to the apertures or lenslets in the Hartmann screen. Unless N is larger than 6, as Fig. 4-4 illustrates the total number of sampling points is given by

$$M_v = 1 + 6(1 + 3 + 5 + 7 + \dots + (2N+1)) = 6(N+1)^2 \quad (4.11)$$

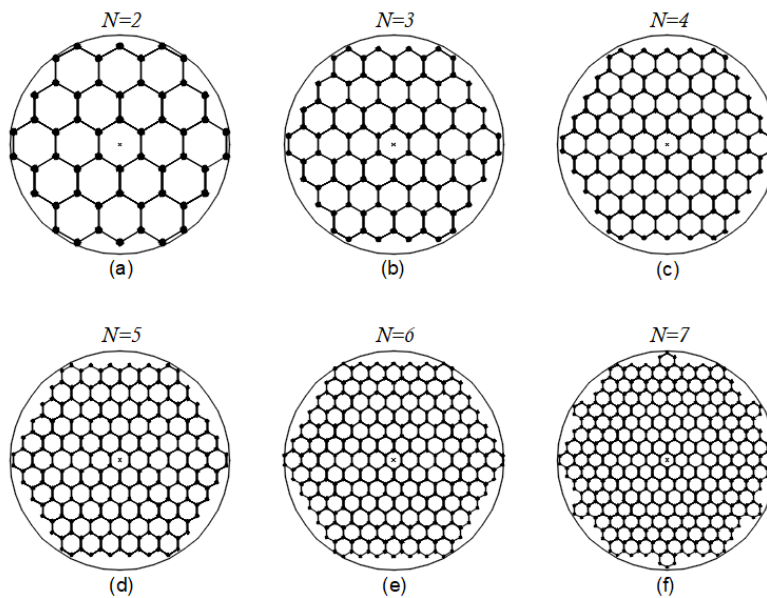


Figure 4-4.- Hexagonal arrays with a different number of rings in a circular pupil.

A relation between the number of rings N and considering the radius (semi-diameter) of the pupil as R , can be defined as

$$\left(R - \frac{s}{2}\right)^2 = [(2N+1)a]^2 + \left(\frac{s}{2}\right)^2 \quad (4.12)$$

If the s value is considered as the maximum diameter for the apertures or lenslets in the Hartmann screen, using Eq. 4.1 in Eq. 4.12 the radius of the circumscribed circle come to be defined as

$$R = \left(\frac{s}{2}\right) \left[3(2N+1)^2 + 1\right]^{1/2} + \frac{s}{2} = \left(\left[3(2N+1)^2 + 1\right]^{1/2} + 1\right) \left(\frac{s}{2}\right) \quad (4.13)$$

Thus, if D is considered as the pupil diameter, it is given by

$$\frac{D}{s} = \left[3(2N+1)^2 + 1\right]^{1/2} + 1 \quad (4.14)$$

On the other hand, if the Hartmann screen was already designed and the Hartmann plate is the only available information, it is necessary to build the reference Hartmann pattern. To do this, the sampling points M obtained from the Hartmann plate give information about the number of apertures or lenslets. Then, using 4.11, it is possible to find the N number of rings that the Hartmann pattern has to have as follows

$$N = \sqrt{\frac{M}{6} - 1} \quad (4.15)$$

Substituting the N value in Eq. 4.14, the ratio D/s can be obtained and in this manner is possible to rebuild the Hartmann screen geometry. As an example, Table 4.1 describes some hexagonal arrays with their corresponding number of rings, hexagonal cells, sampling points and D/s ratio.

Table 4.1.- Values of total hexagonal cells, sampling points and D/s ratio generated depending on the number ring N .

Number of rings (N)	Hexagonal cells (M_c)	Sampling points (M_v)	D/s
1	7	24	6.2915
2	19	54	9.7178
3	37	96	13.1655
4	61	150	16.6205
5	91	216	20.0788
6	127	294	23.5389
7	169+3=172	284+18=302	27

With the values shown in Table 4.1 is possible to generate the transverse aberrations produced by the ideal Hartmann screen with defocusing. Consequently, with the reference Hartmann screen, the wavefront can be retrieved with respect to a close reference sphere.

4.2 Wavefront Retrieval in a Hexagonal Cell

Wavefront reconstruction using a hexagonal array to cover the pupil allows a representation, applying the proposed method, with nine aberration terms and considering the terms in Table 2.2 as follows

$$\begin{aligned}
 W(\rho, \theta) = & A_1 \rho \cos \theta + A_2 \rho \sin \theta + A_3 \rho^2 + A_4 \rho^2 \cos 2\theta + A_5 \rho^2 \sin 2\theta \\
 & + A_6 \rho^3 \cos \theta + A_7 \rho^3 \sin \theta + A_8 \rho^3 \cos 3\theta + A_9 \rho^3 \sin 3\theta
 \end{aligned} \tag{4.16}$$

where similar to the case of square cells, the piston term is lost, because as is well known, transverse aberrations are obtained from the first derivative and piston term is a constant.

4.2.1 Aberration Coefficients Calculation

As described in Chapter 3, the basic principle of operation of the wavefronts retrieval proposed methods in this work is to find a polynomial that recovers a local area of the total wavefront. Twelve slopes are the available data in a hexagonal array, two for each sampling point, and with this information is possible to determine the triangular astigmatism terms, corresponding to the third harmonic component.

The procedure to obtain the coefficient terms for Eq. 4.16 is similar to the described in the previous chapter but considering the four extra terms. Under those circumstances, Eq. 3.15 is expressed as

$$\begin{aligned}
 TA_\rho &= -r_w \frac{\partial W(\rho, \theta)}{\partial \rho} = -r_w \left(\begin{aligned} &A_1 \cos \theta + A_2 \sin \theta + 2A_3 \rho + 2A_4 \rho \cos 2\theta + 2A_5 \rho \sin 2\theta \\ &+ 3A_6 \rho^2 \cos \theta + 3A_7 \rho^2 \sin \theta + 3A_8 \rho^2 \cos 3\theta + 3A_9 \rho^2 \sin 3\theta \end{aligned} \right) \\
 TA_\theta &= -\frac{r_w}{\rho} \frac{\partial W(\rho, \theta)}{\partial \theta} = -r_w \left(\begin{aligned} &-A_1 \sin \theta + A_2 \cos \theta - 2A_4 \rho \sin 2\theta + 2A_5 \rho \cos 2\theta \\ &-A_6 \rho^2 \sin \theta + A_7 \rho^2 \cos \theta - 3A_8 \rho^2 \sin 3\theta + 3A_9 \rho^2 \cos 3\theta \end{aligned} \right)
 \end{aligned} \tag{4.15}$$

Then, the error function is defined by

$$\begin{aligned}
 v &= \sum_{n=1}^6 \left[(TA_\rho - TA'_\rho)^2 + (TA_\theta - TA'_\theta)^2 \right] \\
 &= r_w^2 \sum_{n=1}^6 \left[\left(\frac{\partial W(\rho, \theta)}{\partial \rho} + \frac{TA'_\rho}{r_w} \right)^2 + \left(\frac{1}{\rho} \frac{\partial W(\rho, \theta)}{\partial \theta} + \frac{TA'_\theta}{r_w} \right)^2 \right]
 \end{aligned} \tag{4.16}$$

note that this expression is almost the same that Eq. 3.17 but the upper bound of summation in Eq. 4.16 is 6 because now it is a hexagonal cell.

Substituting Eq. 4.15 in 4.16 is obtained in the next equation

$$v = r_w^2 \sum_{n=1}^4 \left[\begin{array}{l} \left(A_1 \cos \theta + A_2 \sin \theta + 2A_3 \rho + 2A_4 \rho \cos 2\theta + A_5 \rho \sin 2\theta \right. \\ \left. + 3A_6 \rho^2 \cos \theta + 3A_7 \rho^2 \sin \theta + 3A_8 \rho^2 \cos 3\theta + 3A_9 \rho^2 \sin 3\theta + \frac{TA'_\rho}{r_w} \right)^2 \\ + \left(-A_1 \sin \theta + A_2 \cos \theta - 2A_4 \rho \sin 2\theta + 2A_5 \rho \cos 2\theta \right. \\ \left. - A_6 \rho^2 \sin \theta + A_7 \rho^2 \cos \theta - 3A_8 \rho^2 \sin 3\theta + 3A_9 \rho^2 \cos 3\theta + \frac{TA'_\theta}{r_w} \right)^2 \end{array} \right] \quad (4.17)$$

Then, in order to obtain the coefficient aberrations terms in needed to obtain the derivatives of this error function with respect of each one of the nine unidentified coefficients $A_k = 0$

$$-\frac{1}{r_w} \sum_{n=1}^6 [TA'_\rho \cos \theta - TA'_\theta \sin \theta] = \sum_{n=1}^6 \left[\begin{array}{l} \left(A_1 \cos \theta + A_2 \sin \theta + 2A_3 \rho + 2A_4 \rho \cos 2\theta \right. \\ \left. + 2A_5 \rho \sin 2\theta + 3A_6 \rho^2 \cos \theta + 3A_7 \rho^2 \sin \theta \right) \cos \theta \\ \left. + 3A_8 \rho^2 \cos 3\theta + 3A_9 \rho^2 \sin 3\theta \right) \\ - \left(-A_1 \sin \theta + A_2 \cos \theta - 2A_4 \rho \sin 2\theta \right. \\ \left. + 2A_5 \rho \cos 2\theta - A_6 \rho^2 \sin \theta + A_7 \rho^2 \cos \theta \right) \sin \theta \\ \left. - 3A_8 \rho^2 \sin 3\theta + 3A_9 \rho^2 \cos 3\theta \right) \end{array} \right] \quad (4.18)$$

$$-\frac{1}{r_w} \sum_{n=1}^6 [TA'_\rho \sin \theta + TA'_\theta \cos \theta] = \sum_{n=1}^6 \left[\begin{array}{l} \left(A_1 \cos \theta + A_2 \sin \theta + 2A_3 \rho + 2A_4 \rho \cos 2\theta \right. \\ \left. + 2A_5 \rho \sin 2\theta + 3A_6 \rho^2 \cos \theta + 3A_7 \rho^2 \sin \theta \right) \sin \theta \\ \left. + 3A_8 \rho^2 \cos 3\theta + 3A_9 \rho^2 \sin 3\theta \right) \\ + \left(-A_1 \sin \theta + A_2 \cos \theta - 2A_4 \rho \sin 2\theta \right. \\ \left. + 2A_5 \rho \cos 2\theta - A_6 \rho^2 \sin \theta + A_7 \rho^2 \cos \theta \right) \cos \theta \\ \left. - 3A_8 \rho^2 \sin 3\theta + 3A_9 \rho^2 \cos 3\theta \right) \end{array} \right] \quad (4.19)$$

$$-\frac{1}{r_w} \sum_{n=1}^6 [TA'_\rho] = \sum_{n=1}^6 \left[\begin{array}{l} \left(A_1 \cos \theta + A_2 \sin \theta + 2A_3 \rho + 2A_4 \rho \cos 2\theta + 2A_5 \rho \sin 2\theta \right. \\ \left. + 3A_6 \rho^2 \cos \theta + 3A_7 \rho^2 \sin \theta + 3A_8 \rho^2 \cos 3\theta + 3A_9 \rho^2 \sin 3\theta \right) \end{array} \right] \quad (4.20)$$

$$-\frac{1}{r_w} \sum_{n=1}^6 [TA'_\rho \cos 2\theta - TA'_\theta \sin 2\theta] = \sum_{n=1}^6 \left[\begin{array}{l} \left(\begin{array}{l} A_1 \cos \theta + A_2 \sin \theta + 2A_3 \rho \\ + 2A_4 \rho \cos 2\theta + 2A_5 \rho \sin 2\theta \\ + 3A_6 \rho^2 \cos \theta + 3A_7 \rho^2 \sin \theta \\ + 3A_8 \rho^2 \cos 3\theta + 3A_9 \rho^2 \sin 3\theta \end{array} \right) \cos 2\theta \\ - \left(\begin{array}{l} -A_1 \sin \theta + A_2 \cos \theta \\ -2A_4 \rho \sin 2\theta + 2A_5 \rho \cos 2\theta \\ -A_6 \rho^2 \sin \theta + A_7 \rho^2 \cos \theta \\ -3A_8 \rho^2 \sin 3\theta + 3A_9 \rho^2 \cos 3\theta \end{array} \right) \sin 2\theta \end{array} \right] \quad (4.21)$$

$$-\frac{1}{r_w} \sum_{n=1}^6 [TA'_\rho \sin 2\theta + TA'_\theta \cos 2\theta] = \sum_{n=1}^6 \left[\begin{array}{l} \left(\begin{array}{l} A_1 \cos \theta + A_2 \sin \theta + 2A_3 \rho \\ + 2A_4 \rho \cos 2\theta + 2A_5 \rho \sin 2\theta \\ + 3A_6 \rho^2 \cos \theta + 3A_7 \rho^2 \sin \theta \\ + 3A_8 \rho^2 \cos 3\theta + 3A_9 \rho^2 \sin 3\theta \end{array} \right) \sin 2\theta \\ + \left(\begin{array}{l} -A_1 \sin \theta + A_2 \cos \theta \\ -2A_4 \rho \sin 2\theta + 2A_5 \rho \cos 2\theta \\ -A_6 \rho^2 \sin \theta + A_7 \rho^2 \cos \theta \\ -3A_8 \rho^2 \sin 3\theta + 3A_9 \rho^2 \cos 3\theta \end{array} \right) \cos 2\theta \end{array} \right] \quad (4.22)$$

$$-\frac{1}{r_w} \sum_{n=1}^6 [3TA'_\rho \cos \theta - TA'_\theta \sin \theta] = \sum_{n=1}^6 \left[\begin{array}{l} \left(\begin{array}{l} A_1 \cos \theta + A_2 \sin \theta + 2A_3 \rho \\ + 2A_4 \rho \cos 2\theta + 2A_5 \rho \sin 2\theta \\ + 3A_6 \rho^2 \cos \theta + 3A_7 \rho^2 \sin \theta \\ + 3A_8 \rho^2 \cos 3\theta + 3A_9 \rho^2 \sin 3\theta \end{array} \right) \cos \theta \\ + \left(\begin{array}{l} -A_1 \sin \theta + A_2 \cos \theta \\ -2A_4 \rho \sin 2\theta + 2A_5 \rho \cos 2\theta \\ -A_6 \rho^2 \sin \theta + A_7 \rho^2 \cos \theta \\ -3A_8 \rho^2 \sin 3\theta + 3A_9 \rho^2 \cos 3\theta \end{array} \right) \sin \theta \end{array} \right] \quad (4.23)$$

$$-\frac{1}{r_w} \sum_{n=1}^6 [3TA'_\rho \sin \theta + TA'_\theta \cos \theta] = \sum_{n=1}^6 \left[\begin{array}{l} \left(\begin{array}{l} A_1 \cos \theta + A_2 \sin \theta + 2A_3 \rho \\ + 2A_4 \rho \cos 2\theta + 2A_5 \rho \sin 2\theta \\ + 3A_6 \rho^2 \cos \theta + 3A_7 \rho^2 \sin \theta \\ + 3A_8 \rho^2 \cos 3\theta + 3A_9 \rho^2 \sin 3\theta \end{array} \right) \sin \theta \\ + \left(\begin{array}{l} -A_1 \sin \theta + A_2 \cos \theta \\ -2A_4 \rho \sin 2\theta + 2A_5 \rho \cos 2\theta \\ -A_6 \rho^2 \sin \theta + A_7 \rho^2 \cos \theta \\ -3A_8 \rho^2 \sin 3\theta + 3A_9 \rho^2 \cos 3\theta \end{array} \right) \cos \theta \end{array} \right] \quad (4.24)$$

$$-\frac{1}{r_w} \sum_{n=1}^6 [TA'_\rho \cos 3\theta - TA'_\theta \sin 3\theta] = \sum_{n=1}^6 \left[\begin{array}{l} \left(\begin{array}{l} A_1 \cos \theta + A_2 \sin \theta + 2A_3 \rho \\ + 2A_4 \rho \cos 2\theta + 2A_5 \rho \sin 2\theta \\ + 3A_6 \rho^2 \cos \theta + 3A_7 \rho^2 \sin \theta \\ + 3A_8 \rho^2 \cos 3\theta + 3A_9 \rho^2 \sin 3\theta \end{array} \right) \cos 3\theta \\ + \left(\begin{array}{l} -A_1 \sin \theta + A_2 \cos \theta \\ -2A_4 \rho \sin 2\theta + 2A_5 \rho \cos 2\theta \\ -A_6 \rho^2 \sin \theta + A_7 \rho^2 \cos \theta \\ -3A_8 \rho^2 \sin 3\theta + 3A_9 \rho^2 \cos 3\theta \end{array} \right) \sin 3\theta \end{array} \right] \quad (4.25)$$

$$-\frac{1}{r_w} \sum_{n=1}^6 [TA'_\rho \sin 3\theta + TA'_\theta \cos 3\theta] = \sum_{n=1}^6 \left[\begin{array}{l} \left(\begin{array}{l} A_1 \cos \theta + A_2 \sin \theta + 2A_3 \rho \\ + 2A_4 \rho \cos 2\theta + 2A_5 \rho \sin 2\theta \\ + 3A_6 \rho^2 \cos \theta + 3A_7 \rho^2 \sin \theta \\ + 3A_8 \rho^2 \cos 3\theta + 3A_9 \rho^2 \sin 3\theta \end{array} \right) \sin 3\theta \\ + \left(\begin{array}{l} -A_1 \sin \theta + A_2 \cos \theta \\ -2A_4 \rho \sin 2\theta + 2A_5 \rho \cos 2\theta \\ -A_6 \rho^2 \sin \theta + A_7 \rho^2 \cos \theta \\ -3A_8 \rho^2 \sin 3\theta + 3A_9 \rho^2 \cos 3\theta \end{array} \right) \cos 3\theta \end{array} \right] \quad (4.26)$$

The previous equations can be expressed in terms of the multiple angle, $\sin n\theta$ and $\cos n\theta$, and after some algebraic steps can be given by

$$-\frac{1}{r_w} \sum_{n=1}^6 [TA'_\rho \cos \theta - TA'_\theta \sin \theta] = \left[\begin{array}{l} 6A_1 + 2A_3\rho \sum_{n=1}^6 \cos \theta + 2A_4\rho \sum_{n=1}^6 \cos \theta \\ + 2A_5\rho \sum_{n=1}^6 \sin \theta + A_6\rho^2 \sum_{n=1}^6 (2 + \cos 2\theta) \\ + A_7\rho^2 \sum_{n=1}^6 \sin 2\theta + 3A_8\rho^2 \sum_{n=1}^6 \cos \theta \\ + 3A_9\rho^2 \sum_{n=1}^6 \sin 2\theta \end{array} \right] \quad (4.27)$$

$$-\frac{1}{r_w} \sum_{n=1}^6 [TA'_\rho \sin \theta + TA'_\theta \cos \theta] = \left[\begin{array}{l} 6A_2 + 2A_3\rho \sum_{n=1}^6 \sin \theta - 2A_4\rho \sum_{n=1}^6 \sin \theta \\ + 2A_5\rho \sum_{n=1}^6 \cos \theta + A_6\rho^2 \sum_{n=1}^6 \sin 2\theta \\ + A_7\rho^2 \sum_{n=1}^6 (2 - \cos 2\theta) - 3A_8\rho^2 \sum_{n=1}^6 \sin 2\theta \\ + 3A_9\rho^2 \sum_{n=1}^6 \cos 2\theta \end{array} \right] \quad (4.28)$$

$$-\frac{1}{r_w} \sum_{n=1}^6 [TA'_\rho] = \left[\begin{array}{l} A_1 \sum_{n=1}^6 \cos \theta + A_2 \sum_{n=1}^6 \sin \theta + 12A_3\rho + 2A_4\rho \sum_{n=1}^6 \cos \theta \\ + 2A_5\rho \sum_{n=1}^6 \sin 2\theta + 3A_6\rho^2 \sum_{n=1}^6 \cos \theta \\ + 3A_7\rho^2 \sum_{n=1}^6 \sin \theta + 3A_8\rho^2 \sum_{n=1}^6 \cos 3\theta \\ + 3A_9\rho^2 \sum_{n=1}^6 \sin 3\theta \end{array} \right] \quad (4.29)$$

$$-\frac{1}{r_w} \sum_{n=1}^6 [TA'_\rho \cos 2\theta - TA'_\theta \sin 2\theta] = \left[\begin{aligned} & A_1 \sum_{n=1}^6 \cos \theta - A_2 \sum_{n=1}^6 \sin \theta + 2A_3 \rho \sum_{n=1}^6 \cos 2\theta \\ & + 12A_4 \rho + A_6 \rho^2 \sum_{n=1}^6 (2\cos \theta + \cos 3\theta) \\ & + A_7 \rho^2 \sum_{n=1}^6 (\sin 3\theta - 2\sin \theta) \\ & + 3A_8 \rho^2 \sum_{n=1}^6 \cos \theta + 3A_9 \rho^2 \sum_{n=1}^6 \sin \theta \end{aligned} \right] \quad (4.30)$$

$$-\frac{1}{r_w} \sum_{n=1}^6 [TA'_\rho \sin 2\theta + TA'_\theta \cos 2\theta] = \left[\begin{aligned} & A_1 \sum_{n=1}^6 \sin \theta + A_2 \sum_{n=1}^6 \sin \theta + 2A_3 \rho \sum_{n=1}^6 \sin 2\theta \\ & + 12A_5 \rho + A_6 \rho^2 \sum_{n=1}^6 (2\sin \theta + \sin 3\theta) \\ & + 2A_7 \rho^2 \sum_{n=1}^6 \sin \theta \cos \theta \\ & - 3A_8 \rho^2 \sum_{n=1}^6 \sin \theta + 3A_9 \rho^2 \sum_{n=1}^6 \cos \theta \end{aligned} \right] \quad (4.31)$$

$$-\frac{1}{r_w} \sum_{n=1}^6 [3TA'_\rho \cos \theta - TA'_\theta \sin \theta] = \left[\begin{aligned} & A_1 \sum_{n=1}^6 (2 + \cos \theta) + A_2 \sum_{n=1}^6 \sin 2\theta + 6A_3 \rho \sum_{n=1}^6 \cos \theta \\ & + 2A_4 \rho \sum_{n=1}^6 (2\cos \theta + \cos 3\theta) \\ & + A_5 \rho \sum_{n=1}^6 (2\sin \theta + \sin 3\theta) \\ & + A_6 \rho^2 \sum_{n=1}^6 (4\cos 2\theta + 5) + 4A_7 \rho^2 \sum_{n=1}^6 \sin 2\theta \\ & + 3A_8 \rho^2 \sum_{n=1}^6 (2\cos 2\theta + \cos 4\theta) \\ & + 3A_9 \rho^2 \sum_{n=1}^6 (2\sin 2\theta + \sin 4\theta) \end{aligned} \right] \quad (4.32)$$

$$-\frac{1}{r_w} \sum_{n=1}^6 [3TA'_\rho \sin\theta + TA'_\theta \cos\theta] = \left[\begin{aligned} & A_1 \sum_{n=1}^6 \sin 2\theta + A_2 \sum_{n=1}^6 (2 - \cos 2\theta) + 6A_3 \rho \sum_{n=1}^6 \sin \theta \\ & + 2A_4 \rho \sum_{n=1}^6 (\sin 3\theta - 2\sin \theta) \\ & + 2A_5 \rho \sum_{n=1}^6 (2\cos \theta - \cos 3\theta) \\ & + 4A_6 \rho^2 \sum_{n=1}^6 \sin 2\theta + A_7 \rho^2 \sum_{n=1}^6 (5 - 4\cos 2\theta) \\ & + 3A_8 \rho^2 \sum_{n=1}^6 (\sin 4\theta - 2\sin 2\theta) \\ & + 3A_9 \rho^2 \sum_{n=1}^6 (2\cos 2\theta - \cos 4\theta) \end{aligned} \right] \quad (4.33)$$

$$-\frac{1}{r_w} \sum_{n=1}^6 [TA'_\rho \cos 3\theta - TA'_\theta \sin 3\theta] = \left[\begin{aligned} & A_1 \sum_{n=1}^6 \cos 2\theta - A_2 \sum_{n=1}^6 \sin 2\theta + 2A_3 \rho \sum_{n=1}^6 \cos 3\theta \\ & + 2A_4 \rho \sum_{n=1}^6 \cos \theta - 2A_5 \rho \sum_{n=1}^6 \sin \theta \\ & + A_6 \rho^2 \sum_{n=1}^6 (2\cos 2\theta + \cos 4\theta) \\ & + A_7 \rho^2 \sum_{n=1}^6 (\sin 4\theta - 2\sin 2\theta) \\ & + 18A_8 \rho^2 \end{aligned} \right] \quad (4.34)$$

$$-\frac{1}{r_w} \sum_{n=1}^6 [TA'_\rho \sin 3\theta + TA'_\theta \cos 3\theta] = \left[\begin{aligned} & A_1 \sum_{n=1}^6 \sin 2\theta + A_2 \sum_{n=1}^6 \cos 2\theta + 2A_3 \rho \sum_{n=1}^6 \sin 3\theta \\ & + 2A_4 \rho \sum_{n=1}^6 \sin \theta + 2A_5 \rho \sum_{n=1}^6 \cos \theta \\ & + A_6 \rho^2 \sum_{n=1}^6 (2\sin 2\theta + \sin 4\theta) \\ & + A_7 \rho^2 \sum_{n=1}^6 (2\cos 2\theta - 4\cos 4\theta) \\ & + 18A_9 \rho^2 \end{aligned} \right] \quad (4.35)$$

Now, following the same considerations from Eq. 3.30 to 3.32 in Chapter 3, but considering the hexagon, the previous expressions for the aberration terms are

$$A_1 = -\frac{1}{6r_w} \sum_{n=1}^6 [-TA'_\rho \cos\theta - 3TA'_\theta \sin\theta] \quad (4.36)$$

$$A_2 = -\frac{1}{6r_w} \sum_{n=1}^6 [-TA'_\rho \sin\theta + 3TA'_\theta \cos\theta] \quad (4.37)$$

$$A_3 = -\frac{1}{12r_w} \sum_{n=1}^6 [TA'_\rho] \quad (4.38)$$

$$A_4 = -\frac{1}{12r_w} \sum_{n=1}^6 [TA'_\rho \cos 2\theta - TA'_\theta \sin 2\theta] \quad (4.39)$$

$$A_5 = -\frac{1}{12\rho r_w} \sum_{n=1}^6 [TA'_\rho \sin 2\theta + TA'_\theta \cos 2\theta] \quad (4.40)$$

$$A_6 = -\frac{1}{6\rho^2 r_w} \sum_{n=1}^6 [TA'_\rho \cos\theta + TA'_\theta \sin\theta] \quad (4.41)$$

$$A_7 = -\frac{1}{6\rho^2 r_w} \sum_{n=1}^6 [TA'_\rho \sin\theta - TA'_\theta \cos\theta] \quad (4.42)$$

$$A_8 = -\frac{1}{18\rho^2 r_w} \sum_{n=1}^6 [TA'_\rho \cos 3\theta - TA'_\theta \sin 3\theta] \quad (4.43)$$

$$A_9 = -\frac{1}{18\rho^2 r_w} \sum_{n=1}^6 [TA'_\rho \sin 3\theta + TA'_\theta \cos 3\theta] \quad (4.44)$$

Finally, substituting the coordinates for the six points in the correspond hexagonal cell and taking the center of the cell as the origin, the aberrations terms in Cartesian coordinates are

$$A_1 = -\frac{1}{6r_w} \left[-\sqrt{3}TA'_{y_1} + 3TA'_{x_2} + \sqrt{3}TA'_{y_3} - \sqrt{3}TA'_{y_4} + 3TA'_{x_5} + \sqrt{3}TA'_{y_6} \right] \quad (4.45)$$

$$A_2 = -\frac{1}{6r_w} \left[\begin{array}{l} -\sqrt{3}TA'_{x_1} + 2TA'_{y_1} - TA'_{y_2} + \sqrt{3}TA'_{x_3} + 2TA'_{y_3} \\ -\sqrt{3}TA'_{x_4} + 2TA'_{y_4} - TA'_{y_5} + \sqrt{3}TA'_{x_6} + 2TA'_{y_6} \end{array} \right] \quad (4.46)$$

$$A_3 = -\frac{1}{24\rho r_w} \left[\begin{array}{l} \sqrt{3}TA'_{x_1} + TA'_{y_1} + 2TA'_{y_2} - \sqrt{3}TA'_{x_3} - TA'_{y_3} \\ -\sqrt{3}TA'_{x_4} - TA'_{y_4} - 2TA'_{y_5} + \sqrt{3}TA'_{x_6} - TA'_{y_6} \end{array} \right] \quad (4.47)$$

$$A_4 = -\frac{1}{24\rho r_w} \left[\begin{array}{l} \sqrt{3}TA'_{x_1} - TA'_{y_1} - 2TA'_{y_2} - \sqrt{3}TA'_{x_3} - TA'_{y_3} \\ -\sqrt{3}TA'_{x_4} + TA'_{y_4} + 2TA'_{y_5} + \sqrt{3}TA'_{x_6} + TA'_{y_6} \end{array} \right] \quad (4.48)$$

$$A_5 = -\frac{1}{24\rho r_w} \left[\begin{array}{l} TA'_{x_1} + \sqrt{3}TA'_{y_1} + 2TA'_{x_2} + TA'_{x_3} - \sqrt{3}TA'_{y_3} \\ -TA'_{x_4} - \sqrt{3}TA'_{y_4} - 2TA'_{y_5} - TA'_{x_6} + \sqrt{3}TA'_{y_6} \end{array} \right] \quad (4.49)$$

$$A_6 = -\frac{1}{12\rho^2 r_w} \left[\begin{array}{l} TA'_{x_1} + \sqrt{3}TA'_{y_1} - 2TA'_{x_2} + TA'_{x_3} - \sqrt{3}TA'_{y_3} \\ + TA'_{x_4} + \sqrt{3}TA'_{y_4} - 2TA'_{x_5} + TA'_{x_6} - \sqrt{3}TA'_{y_6} \end{array} \right] \quad (4.50)$$

$$A_7 = -\frac{1}{12\rho^2 r_w} \left[\begin{array}{l} \sqrt{3}TA'_{x_1} - TA'_{y_1} + 2TA'_{y_2} - \sqrt{3}TA'_{x_3} - TA'_{y_3} \\ + \sqrt{3}TA'_{x_4} - TA'_{y_4} + 2TA'_{x_5} - \sqrt{3}TA'_{x_6} - TA'_{y_6} \end{array} \right] \quad (4.51)$$

$$A_8 = -\frac{1}{36\rho^2 r_w} \left[\begin{array}{l} TA'_{x_1} - \sqrt{3}TA'_{y_1} - 2TA'_{x_2} + TA'_{x_3} + \sqrt{3}TA'_{y_3} \\ + TA'_{x_4} - \sqrt{3}TA'_{y_4} - 2TA'_{x_5} + TA'_{x_6} + \sqrt{3}TA'_{y_6} \end{array} \right] \quad (4.52)$$

$$A_9 = -\frac{1}{36\rho^2 r_w} \left[\begin{array}{l} \sqrt{3}TA'_{x_1} + TA'_{y_1} - 2TA'_{y_2} - \sqrt{3}TA'_{x_3} + TA'_{y_3} \\ + \sqrt{3}TA'_{x_4} + TA'_{y_4} - 2TA'_{y_5} - \sqrt{3}TA'_{x_6} + TA'_{y_6} \end{array} \right] \quad (4.53)$$

where r_w is nearly constant and approximately equal to the distance from the exit pupil to the observation plane. In addition, these equations illustrate that they are dependent on the six sampling points.

4.2.2 Aberration Values Within the Hexagonal Cells Calculation

With the expression described in the previous section and the transverse aberrations data, the wavefront can be retrieved. In the same manner that for the square cells, it is necessary to create new values $w_i(x,y)$ inside the cells in order to obtain a smooth local surface in each one. Fig. 4-5 illustrates the proposed number and design of inner points to create a better wavefront reconstruction.

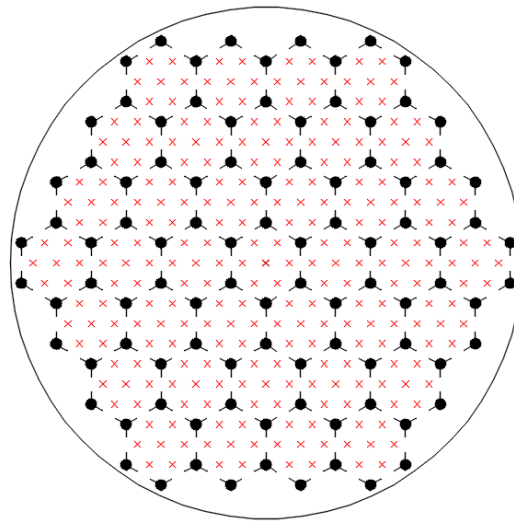


Figure 4-5.- Interpolated spots, red crosses, inside the hexagonal cells that cover the whole pupil.

These new values were calculated using the ratio that exists between the side of the hexagon cell and the apothem, defined by Eq. 4.1, that Fig. 4-6 shows, as follow

$$2a = 3\rho_i \rightarrow a = \frac{3}{2}\rho_i \quad (4.54)$$

$$\frac{\sqrt{3}}{2}s = \frac{3}{2}\rho_i \rightarrow \rho_i = \frac{s}{\sqrt{3}} \quad (4.55)$$

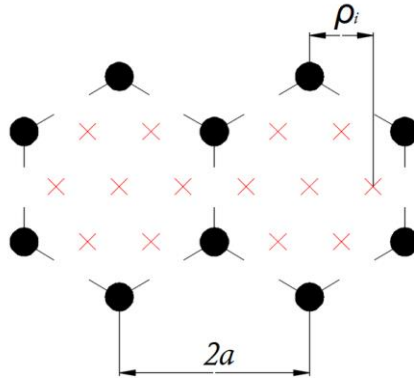


Figure 4-6.- Contiguous cells illustrating the distance between two sampling points and the apothem length.

where ρ_i is the distance between points that are placed inside the hexagonal cells. This distance is created in a manner that sampling points and the inside points are uniformly distributed. Using the value of ρ_i and varying the θ angle from 0° to 360° , is possible to obtain the (x_i, y_i) coordinates in increments of 60° using the coordinate conversion expressions

$$\begin{aligned} x_i &= x_c + \rho_i \cos\theta \\ y_i &= y_c + \rho_i \sin\theta \end{aligned} \tag{4.56}$$

where x_c and y_c are to the values of the cell center and x_i and y_i are the values of the new coordinates inside the cell.

Also, in Fig. 4-6 is possible to see that the new inside values are rotated by 30° with respect to the hexagonal cell points, and with this characteristic, the wavefront retrieval is uniform.

Once the new values were generated, the wavefront deformation over the whole pupil is possible to retrieve using the aberration coefficients and using the next expression in Cartesian coordinates

$$\begin{aligned}
w_i(x, y) = & A_1(x, y)x + A_2(x, y)y + A_3(x, y)(x^2 + y^2) + A_4(x, y)(x^2 - y^2) \\
& + 2A_5(x, y)xy + A_6(x, y)x(x^2 + y^2) + A_7(x, y)y(x^2 + y^2) \\
& + A_8(x, y)x(y^2 - x^2) + A_9(x, y)y(y^2 - x^2)
\end{aligned} \tag{4.57}$$

The wavefront deformation is expressed in lower case, w , because the expression is used to retrieve the local wavefront in each one of the hexagonal cells. Furthermore, as can be seen in Eq. 4.57, the piston term $A_0(x,y)$ is lost, so, as in the same manner than square cells, a procedure is needed to calculate this term and it is described in the next section.

4.2.3 Contiguous Cells Joining and Wavefront Representations

In a similar manner than square cells, the piston term can be obtained if the values of adjacent cells are compared. However, in the hexagonal cells due to the geometry and just for some specific cells, there are three possible configurations or sharing points between cells; two, three and four sampling shared points. Due to the fact that contiguous cells have sampling points in common, and in this points the transverse aberrations are the same, the heights and the slopes are continuous but might be a curvature discontinuity between them. Fig. 4-7 illustrates two neighboring hexagonal cells before and after the procedure of finding the piston term.

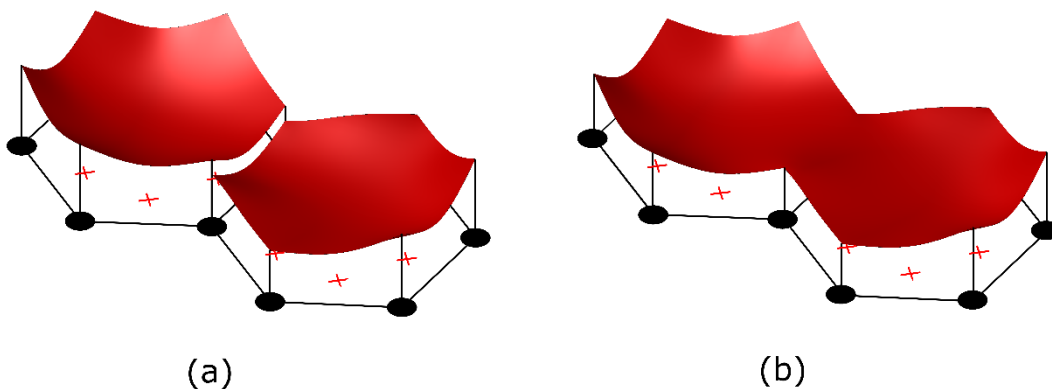


Figure 4-7.- Representation of hexagonal cells before the piston term calculation (a) and after (b).

It has been explained that the configuration of hexagonal cells selected is considering a cell in the center of the pupil. This geometry also allows that this central cell will be considered as the reference to start the process of piston term calculation. Then, the next cells to be leveled are those that are located in ring number 1 and continue with numbers 2, 3, ..., N . However, the process to find the piston term for hexagonal configuration is not as simple as for the square array.

For hexagonal array, the method to obtain the piston term is considered in twelve steps. One step for each one of the sides and vertices of the hexagon as Fig. 4-8 shows.

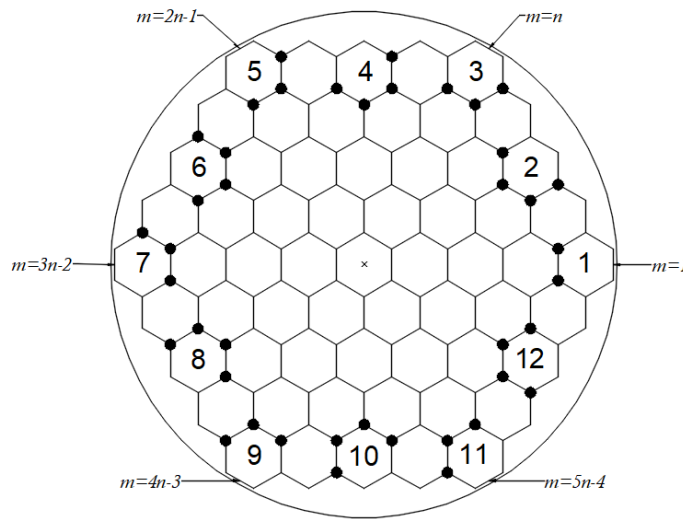


Figure 4-8.- Sampling points shared between contiguous cells and the twelve cases to calculate the piston term.

As described in section 4.1 of this chapter, the hexagonal cells are identified by (n, m) and for the vertices is used the letter l . From Fig. 4-8 can be seen that to leveled the cells, cells of previous rings have to be considered and for some cases, there are two, three or four shared sampling points to calculate the piston term. For this reason, there have twelve cases to be considered. At this point is important to remark that once the value of the piston term for a cell has been found, this value has to be added to the thirteen values, considering the inside values, immediately. This is because in most cases the next cell is in the same ring. So, after the piston term has been obtained, the value is added to the wavefront value by the next expression

$$W_{A_{0g}}(n, m, l) = W(n, m, l) + A_{0g} \quad (4.58)$$

where the subscript g is the case number. The twelve cases are listed in Table 4.2 with their respective conditions in which they have to be applied.

Table 4.2.- Cases and conditions to apply the piston term calculation.

Case	Condition	Equation	
1	$m=1$	$A_{01} = \frac{[W(n, 1, 3) - W(n-1, 1, 1)] + [W(n, 1, 4) - W(n-1, 1, 6)]}{2}$	(4.59)
2	$1 < m < n$	$A_{02} = \frac{1}{4} \left\{ [W(n, m, 3) - W(n-1, m, 1)] \right\} + \frac{1}{4} \left\{ W(n, m, 6) - W(n, m-1, 2) \right\} + \frac{1}{4} \left\{ W(n, m, 4) - \left[\frac{W(n-1, m, 6) + W(n-1, m-1, 2)}{2} \right] \right\} + \frac{1}{4} \left\{ W(n, m, 5) - \left[\frac{W(n-1, m-1, 1) + W(n, m-1, 3)}{2} \right] \right\}$	(4.60)
3	$m=n$	$A_{03} = \frac{1}{3} \left\{ [W(n, m, 4) - W(n-1, m-1, 2)] \right\} + \frac{1}{3} \left\{ W(n, m, 6) - W(n, m-1, 2) \right\} + \frac{1}{3} \left\{ W(n, m, 5) - \left[\frac{W(n-1, m-1, 1) + W(n, m-1, 3)}{2} \right] \right\}$	(4.61)
4	$n < m < 2n-1$	$A_{04} = \frac{1}{4} \left\{ [W(n, m, 4) - W(n-1, m-1, 2)] \right\} + \frac{1}{4} \left\{ W(n, m, 1) - W(n, m-1, 3) \right\} + \frac{1}{4} \left\{ W(n, m, 5) - \left[\frac{W(n-1, m-1, 1) + W(n-1, m-2, 3)}{2} \right] \right\} + \frac{1}{4} \left\{ W(n, m, 6) - \left[\frac{W(n-1, m-2, 3) + W(n, m-1, 4)}{2} \right] \right\}$	(4.62)
5	$m=2n-1$	$A_{05} = \frac{1}{3} \left\{ [W(n, m, 5) - W(n-1, m-2, 3)] \right\} + \frac{1}{3} \left\{ W(n, m, 1) - W(n, m-1, 3) \right\} + \frac{1}{3} \left\{ W(n, m, 6) - \left[\frac{W(n-1, m-2, 2) + W(n, m-1, 4)}{2} \right] \right\}$	(4.63)
6	$2n-1 < m < 3n-2$	$A_{06} = \frac{1}{4} \left\{ [W(n, m, 5) - W(n-1, m-2, 3)] \right\} + \frac{1}{4} \left\{ W(n, m, 2) - W(n, m-1, 4) \right\} + \frac{1}{4} \left\{ W(n, m, 6) - \left[\frac{W(n-1, m-2, 2) + W(n-1, m-3, 4)}{2} \right] \right\} + \frac{1}{4} \left\{ W(n, m, 1) - \left[\frac{W(n-1, m-3, 3) + W(n, m-1, 5)}{2} \right] \right\}$	(4.64)

7	$m=3n-2$	$A_{07} = \frac{1}{3} \left\{ [W(n, m, 6) - W(n-1, m-3, 4)] \right\} \\ + \frac{1}{3} \left\{ [W(n, m, 2) - W(n, m-1, 4)] \right\} \\ + \frac{1}{3} \left\{ W(n, m, 1) - \left[\frac{W(n-1, m-3, 3) + W(n, m-1, 5)}{2} \right] \right\}$	(4.65)
8	$3n-2 < m < 4n-3$	$A_{08} = \frac{1}{4} \left\{ [W(n, m, 6) - W(n-1, m-3, 4)] \right\} \\ + \frac{1}{4} \left\{ [W(n, m, 3) - W(n, m-1, 5)] \right\} \\ + \frac{1}{4} \left\{ W(n, m, 1) - \left[\frac{W(n-1, m-3, 3) + W(n-1, m-4, 5)}{2} \right] \right\} \\ + \frac{1}{4} \left\{ W(n, m, 2) - \left[\frac{W(n-1, m-4, 4) + W(n, m-1, 5)}{2} \right] \right\}$	(4.66)
9	$m=4n-3$	$A_{09} = \frac{1}{3} \left\{ [W(n, m, 1) - W(n-1, m-4, 5)] \right\} \\ + \frac{1}{3} \left\{ [W(n, m, 3) - W(n, m-1, 5)] \right\} \\ + \frac{1}{3} \left\{ W(n, m, 2) - \left[\frac{W(n-1, m-4, 4) + W(n, m-1, 6)}{2} \right] \right\}$	(4.67)
10	$4n-3 < m < 5n-4$	$A_{10} = \frac{1}{4} \left\{ [W(n, m, 1) - W(n-1, m-4, 5)] \right\} \\ + \frac{1}{4} \left\{ [W(n, m, 4) - W(n, m-1, 6)] \right\} \\ + \frac{1}{4} \left\{ W(n, m, 2) - \left[\frac{W(n-1, m-4, 4) + W(n-1, m-5, 6)}{2} \right] \right\} \\ + \frac{1}{4} \left\{ W(n, m, 6) - \left[\frac{W(n-1, m-5, 5) + W(n, m-1, 1)}{2} \right] \right\}$	(4.68)
11	$m=5n-4$	$A_{11} = \frac{1}{3} \left\{ [W(n, m, 2) - W(n-1, m-5, 6)] \right\} \\ + \frac{1}{3} \left\{ [W(n, m, 4) - W(n, m-1, 6)] \right\} \\ + \frac{1}{3} \left\{ W(n, m, 3) - \left[\frac{W(n-1, m-5, 5) + W(n, m-1, 1)}{2} \right] \right\}$	(4.69)
12	$5n-4 < m < 6n-6$	$A_{12} = \frac{1}{4} \left\{ [W(n, m, 2) - W(n-1, m, 6)] \right\} \\ + \frac{1}{4} \left\{ [W(n, m, 5) - W(n, m-1, 1)] \right\} \\ + \frac{1}{4} \left\{ W(n, m, 3) - \left[\frac{W(n-1, 1, 5) + W(n-1, m-6, 1)}{2} \right] \right\} \\ + \frac{1}{4} \left\{ W(n, m, 4) - \left[\frac{W(n-1, m-6, 6) + W(n, m-1, 2)}{2} \right] \right\}$	(4.70)

After the hexagonal cells have been leveled in the whole pupil, the wavefront profile is complete.

It is clear that this process is not a simple one for a hexagonal array, but this is because of the configuration of geometry.

A Hartmann pattern from a simulated wavefront is used to estimate the proposed technique in this chapter. The synthetic wavefront has the characteristics to be a polynomial with a high degree, power of 5, in order to evaluate the method with a wavefront that has high spatial frequencies. The well-known trapezoidal integration and square cell integration methods presented in the previous chapter are used as procedures to compare the integration of the hexagonal cell. There is a fact that has to be considered, the Hartmann pattern used to make the wavefront reconstruction of trapezoidal and square cells methods is a square array pattern. Thus, the number of sampling points is not the same for hexagonal cells as Fig. 4-9 illustrates.

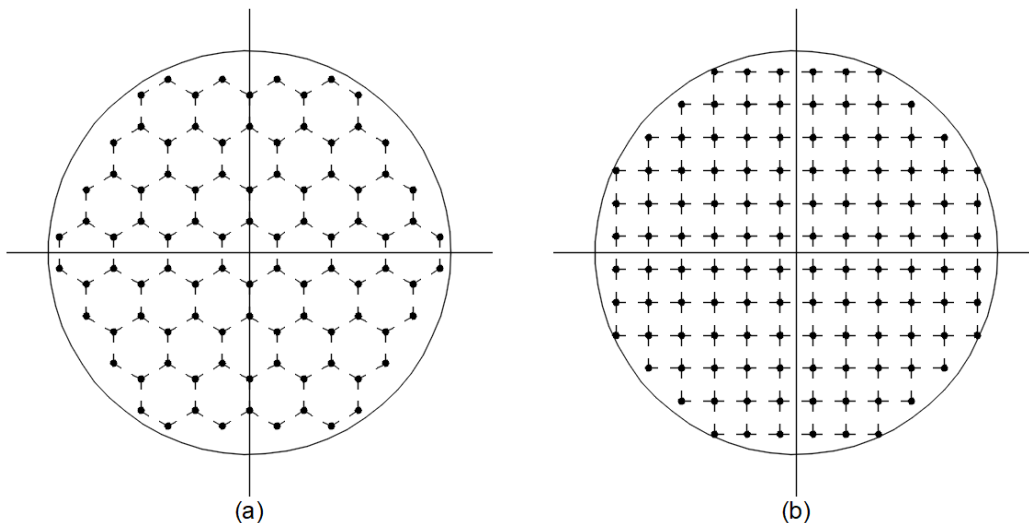


Figure 4-9.- (a) Hexagonal Hartmann pattern with 96 sampling points and (b) square Hartmann pattern with 120 sampling points.

The wavefront simulated was built with the data shown in Table 4.3. Even when the wavefront has local deformations, there are low enough frequencies that can be detected by the hexagonal method.

Table 4.3.- Orthonormal Zernike circle polynomials $Z_j(\rho, \theta)$ terms used in the simulated wavefront illustrated in Fig. 4-10.

Aberration name	j	n	M	$Z_j(\rho, \theta)$	Value ($\times 10^{-3}$)
Defocus	4	2	0	$\sqrt{3}(2\rho^2 - 1)$	0.050
Coma along x axis	7	3	0	$\sqrt{8}(3\rho^3 - 2\rho)\cos\theta$	0.080
Primary Spherical Aberration	11	4	0	$\sqrt{5}(6\rho^4 - 6\rho^2 + 1)$	0.100
Quadrangular Astigmatism at 0°	14	4	4	$\sqrt{10}\rho^4 \cos 4\theta$	0.050
Secondary Coma along x axis	16	5	1	$\sqrt{12}(10\rho^5 - 12\rho^3 + 3\rho)\cos\theta$	0.030
Pentagonal Astigmatism, with peaks at $s(72^\circ) + 18^\circ$	33	7	5	$\sqrt{12}\rho^5 \sin 5\theta$	-0.050

Fig. 4-10 illustrates the original simulated wavefront and the retrieved ones by using three different proposed methods.

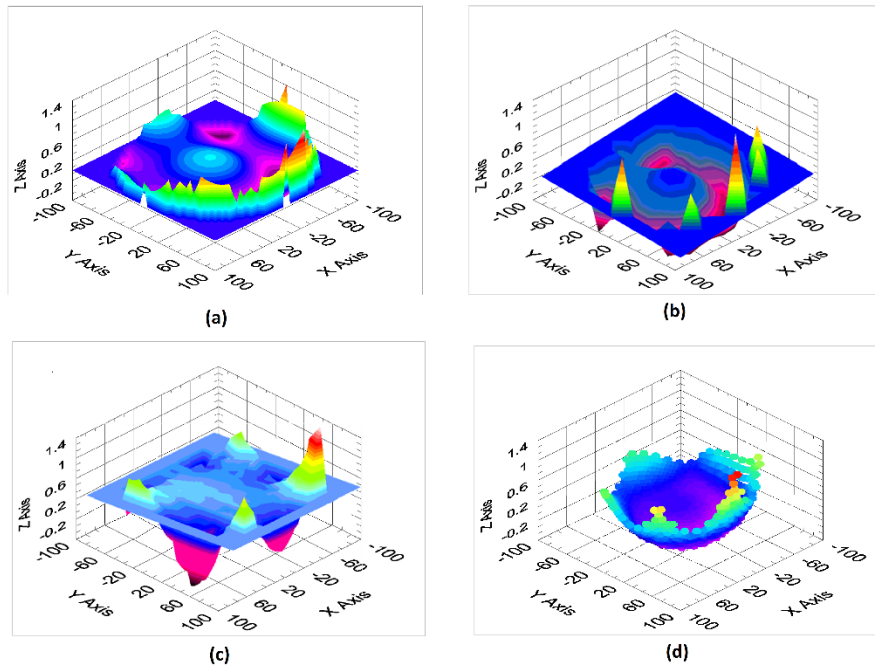


Figure 4-10.- (a) Simulated wavefront to be tested and retrieved, (b) retrieved wavefront after trapezoidal integration, (c) retrieved wavefront using square cell integration and (d) retrieved wavefront after hexagonal cell integration [88].

Fig. 4-10(a) shows that the wavefront retrieved with the hexagonal cells method is smoother and continuous than the obtained with trapezoidal and square cells reconstruction. It is worth noticing that the wavefront plotted does not have the reference mesh in order to show a better figure.

In order to prove the accuracy and better reconstruction of hexagonal cells method, the Peak-to-Valley values, the difference between the maximum and minimum values of the wavefront at zones with values of derivatives in x and y equal to zero. The obtained results are shown in Table 4.4.

Table 4.4.- Peak-to-Valley values obtained with the integration procedures compared.

Figure	Wavefront	Value
3.10(a)	Simulated	1.030227
3.10(b)	Trapezoidal integration	0.816400
3.10(c)	Square cell integration	0.874807
3.10(d)	Hexagonal cell integration	1.000288

Table 4.4 shows that the best result with hexagonal cell integration and the less accurate is obtained with a trapezoidal integration method. A perfect integration method would have to produce an identical retrieved wavefront [88].

Additionally, in order to prove the effectiveness of the methods proposed in the ocular aberrations measurements, two keratoconus corneas were analyzed. Subjects data obtained with a Pentacam AXL, Oculus, were used to prove the methods and compared with the trapezoidal integration. The graphic results and Zernike terms used are described in Table 4.5, Table 4.7 and Table 4.8.

Table 4.5.- Orthonormal Zernike circle polynomials $Z_j(\rho, \theta)$ terms obtained from two subjects showed in Table 4.7 and 4.8.

Aberration Term	Subject 1	Subject 2
$Z_j(\rho, \theta)$	Value ($\times 10^{-3}$)	Value ($\times 10^{-3}$)
1	247.180	249.180
$2\rho \cos \theta$	2.333	2.535
$2\rho \sin \theta$	-1.000	-1.032
$\sqrt{3}(2\rho^2 - 1)$	138.354	142.180
$\sqrt{6}\rho^2 \sin 2\theta$	-1.123	-1.390
$\sqrt{6}\rho^2 \cos 2\theta$	0.889	0.879
$\sqrt{8}(3\rho^3 - 2\rho)\sin \theta$	1.130	67.368
$\sqrt{8}(3\rho^3 - 2\rho)\cos \theta$	0.085	-83.550
$\sqrt{8}\rho^3 \sin \theta$	1.132	1.210

In the same manner, as the previous results, an evaluation of the Peak-to-Valley value was calculated. The results of this analysis are presented in Table. 4.6. Data described in Table 4.6 showed that hexagonal integration is better than trapezoidal and square cell integration, due that the Peak-to-Valley value is closer to the simulated wavefront. The values are higher than in Table 4.5 because the piston term and defocus are higher as well.

Table 4.6.- Peak-to-Valley values obtained with the integration procedures compared.

Wavefront	Subject 1	Subject 2
Simulated	794.340	1087.656
Trapezoidal integration	704.3270	886.397
Square cell integration	798.2325	1197.237
Hexagonal cell integration	795.4974	1152.435

Table 4.7.- Wavefronts simulated and rebuilt with the methods proposed with data obtained from subject 1 using the Pentacam instrument.

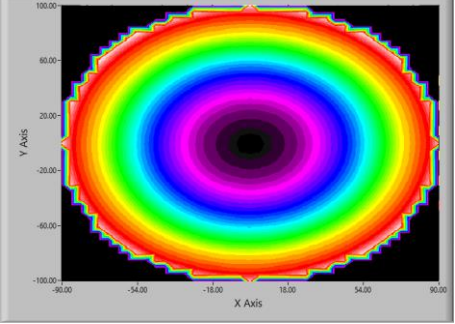
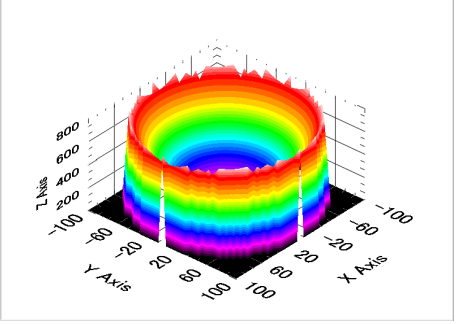
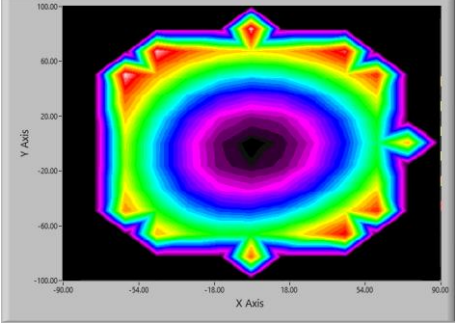
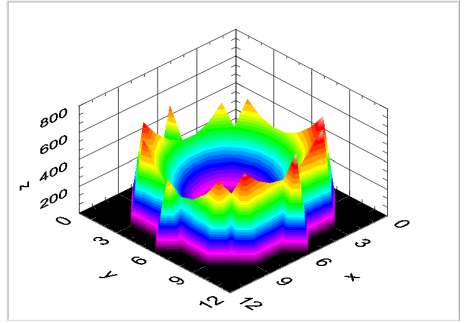
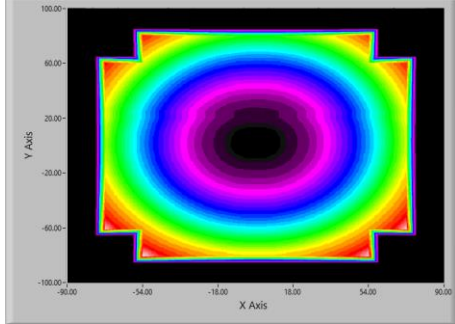
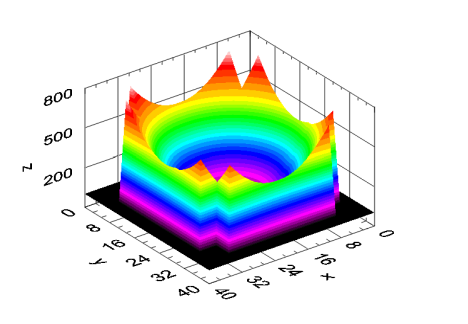
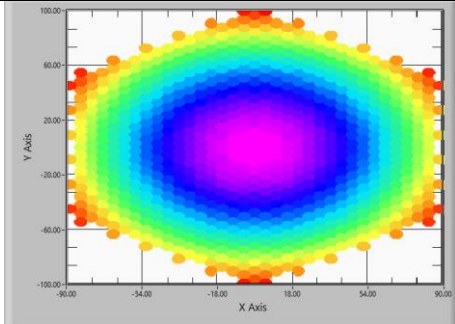
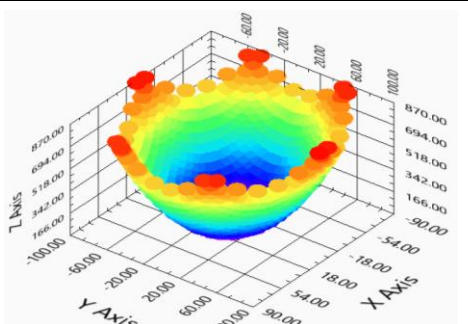
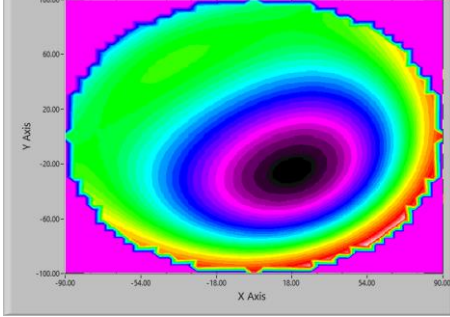
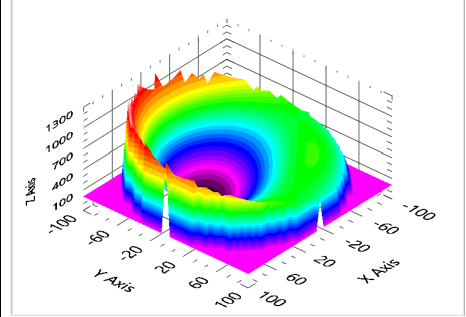
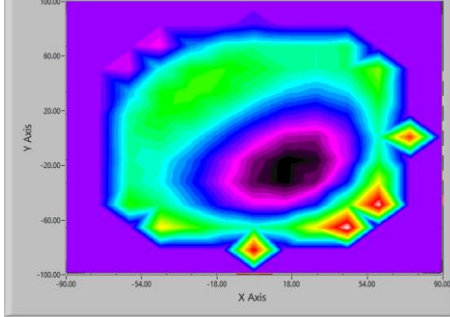
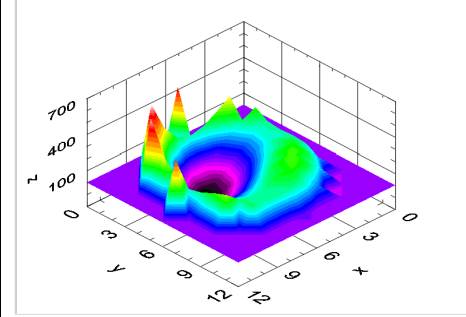
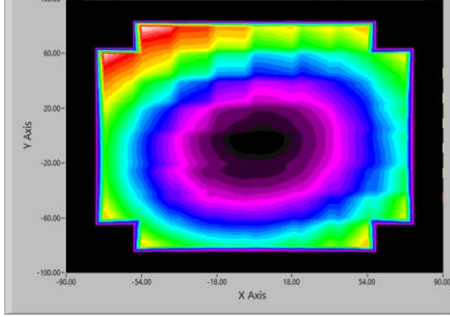
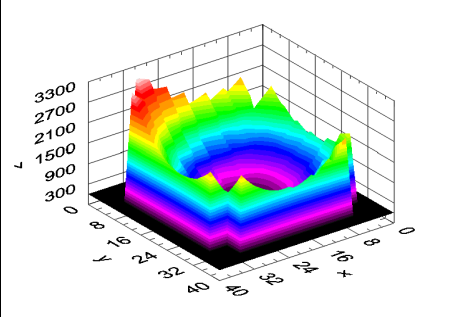
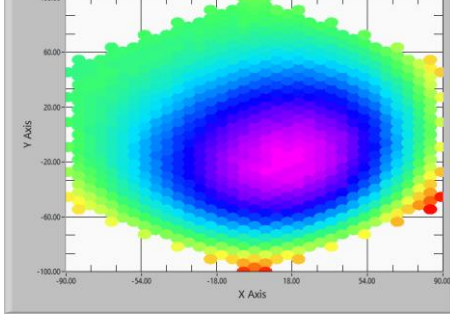
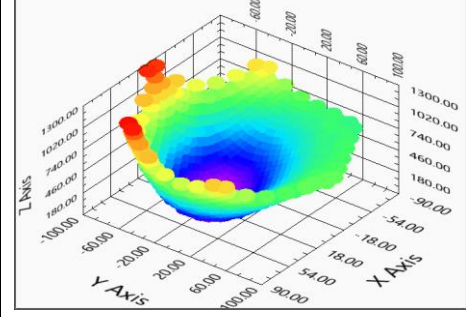
Method	X-Y Plane View	X-Y-Z Plane View
Simulated		
Trapezoidal Integration		
Square Integration		
Hexagonal Integration		

Table 4.8.- Wavefronts simulated and rebuilt with the methods proposed with data obtained from subject 2 using the Pentacam instrument.

Method	X-Y Plane View	X-Y-Z Plane View
Simulated		
Trapezoidal Integration		
Square Integration		
Hexagonal Integration		

A continuity analysis of the wavefront retrieved function was performed between two contiguous cells. This analysis was developed just in the square cell, assuming that as the aberration coefficients calculation is the same in hexagonal cells, the continuity will exist in this one as well. Continuity of several cells frontier was analyzed but here is described just one. Cells (1, 1) and (2, 1) from subject 1 were selected to describe the continuity analysis, evaluating the x and y values in Eq. 3.43. Aberrations coefficients values are shown in Table 4.9.

Table 4.9.- Aberration coefficients obtained using the square integration method for subject 1.

Aberration coefficient	Cell (1, 1)	Cell (2, 1)
A_0	0.001298	0.001708
A_1	-0.28784	-0.48447
A_2	-0.29642	-0.29123
A_3	0.098503	0.098503
A_4	0.000185	0.000185
A_5	0.001298	0.001708

Then, using Eq. 3.43, the wavefront aberration function to these cells are

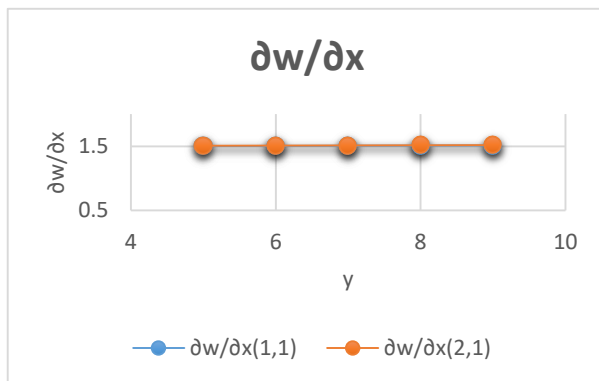
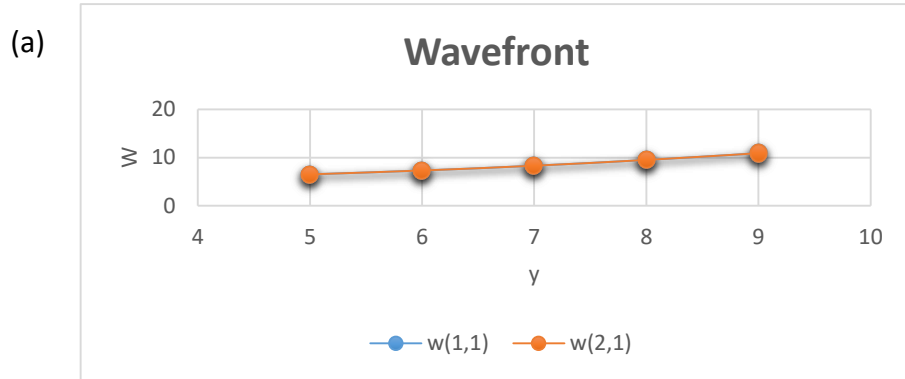
$$w_{(1,1)}(x, y) = 0.001298 - 0.28784x - 0.29642y + 0.0098503(x^2 + y^2) + 0.000185(x^2 - y^2) + 2(0.001298)xy \quad (4.71)$$

$$w_{(2,1)}(x, y) = 0.001708 - 0.48447x - 0.29123y + 0.0098503(x^2 + y^2) + 0.000185(x^2 - y^2) + 2(0.001708)xy \quad (4.72)$$

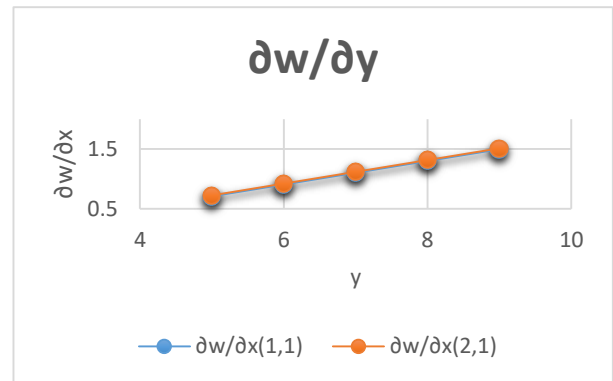
The x and y values considering in each one of the cells and wavefront values obtained with previous Eqs. are described in Table 4.10 and data are plotted in Fig. 4-11.

Table 4.10.- Wavefront and derivatives obtained from the (1,1) and (2,1) cells.

Cell (1, 1)					Cell (2, 1)				
x	y	w	$\partial w/\partial x$	$\partial w/\partial y$	x	y	w	$\partial w/\partial x$	$\partial w/\partial y$
9	9	10.91072	1.512	1.497	10	9	10.91072	1.520	1.513
9	8	9.51237	1.509	1.300	10	8	9.512369	1.512	1.316
9	7	8.310656	1.507	1.103	10	7	8.310655	1.513	1.119
9	6	7.305578	1.504	0.907	10	6	7.305577	1.510	0.922
9	5	6.497136	1.502	0.710	10	5	6.497135	1.506	0.726



(b)



(c)

Figure 4-11.- (a) Wavefront values data, (b) Partial derivatives in x and (c) Partial derivatives in y.

Values in Table 4.10 and Fig. 4-11 is demonstrated that the values at the wavefront and derivatives are similar. The small difference may be due to numerical errors because of the integration process or term aberration calculation.

4.3 Conclusions

In this chapter, a novel technique to retrieve the wavefront was presented, which is a zonal method that uses the slopes measurements at the vertices of a Hartmann pattern with a hexagonal array. One of the advantages is the uniform sampling, that compared with the square array, is more regular and cover more area, even in the pupil edges.

An important characteristic of this method is that each one of the hexagonal cells has his own polynomial expressions, formed by nine terms, tilts, curvature, astigmatism, comas, and triangular astigmatism. Moreover, the method allows the detection of local small errors that cannot be detected with only one polynomial fitting.

To conclude, the accuracy of the presented technique is greater than the obtained by other methods. Another possibility is that instead of using the measured slopes at the sampling points, the Fried geometry can be used, which measure the slopes inside of the cells [89].

Chapter 5 -Eye Models to Predict Quality Vision in Age-Related Macular Degeneration

The healthy human eye is a sophisticated optical system that is capable of forming images on the retina with good resolution. It belongs to a general group of eyes well-known as 'camera-type eyes' because, in a simple manner, the eye works as a camera lens focusing light onto a film. In the eye, the optical imaging system is formed by the cornea and crystalline lens, while the retina is the detection instrument. Now, the complexity of the eye comes when is analyzed as a complete biological organ and the neural connections have to be considered. Similarly, the cornea and lens are living lenses, so, other factors like organic components, start to be important.

As the eye can be explained from an optical system perspective, it can be affected by aberrations that reduce the quality of the retinal image. The total aberration contribution, mainly, can be divided between the two components of the optical imaging system, i.e., the cornea and the eye lens. Also, deteriorations in the retina, about which we will talk later, reduce the image resolution. But, there are additional factors responsible for the degradation of retinal images like diffraction in the pupil and intraocular scattering [9], [10].

In this chapter, an overview of the human eye is studied and the AMD is analyzed, also, a preview series of eye models with AMD are presented.

5.1 Eye Model with Age-Related Macular Degeneration

In this section, preliminary results of personalized eye models with AMD are described. As previously mentioned, drusen are a particular marker in AMD; its presence in the retina deforms the spherical shape of this. Therefore, modeling these deformations in the retina

using Zemax, an exact ray-tracing software, is possible to obtain the Amsler grid image simulation.

The first step was to generate a matrix with central deformations, fovea area, representing the drusen. To define the central area, the standard Wisconsin Age-Related Maculopathy Grading System [90] was used. It is a system that divides the macula into three areas as Fig. 5-1 shows, where the innermost circle has a radius of $500\ \mu\text{m}$, the radii of the middle is $1500\ \mu\text{m}$ and the outer has a radius of $3000\ \mu\text{m}$. The areas covered corresponds to the fovea, innermost circle and the rest of macula in the middle and outer circles. These images were used to simulate the retinal edemas, modifying the spherical shape of the retina and using the schematic eye data shown in Table 5.1.

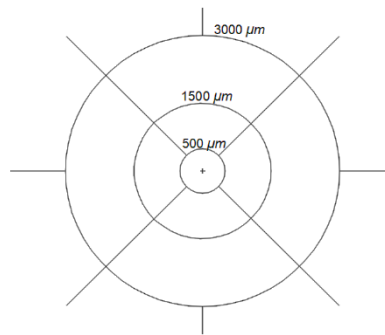


Figure 5-1.- Standard Wisconsin Age-Related Maculopathy grading system. The grid is defined by three concentric circles centered at the macula.

With the standard grid defined, a series of matrices with drusen of several sizes was built in order to obtain the Amsler grid deformations. The drusen were placed in the central area of the standard grid, as the central macular area is the most affected. Fig. 5-2 illustrates an example of the schematic eye with deformations in the retina, where the drusen size is $300\ \mu\text{m}$.

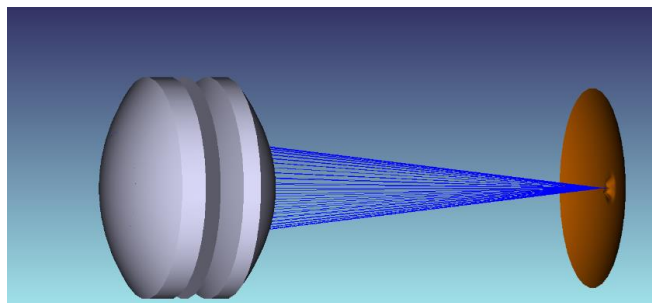
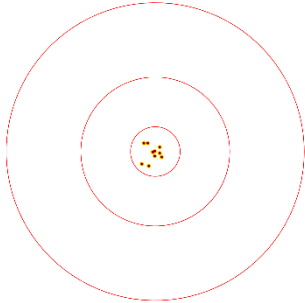
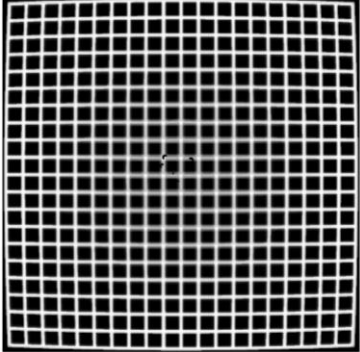
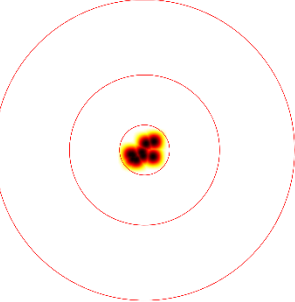
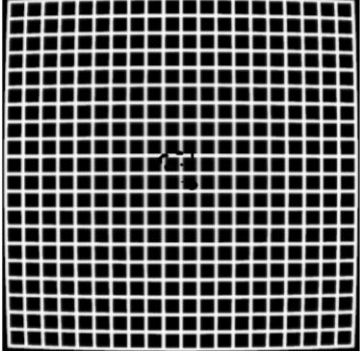
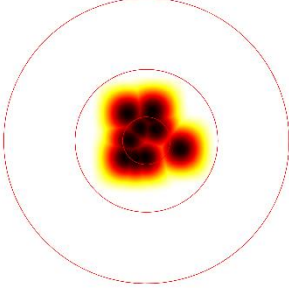
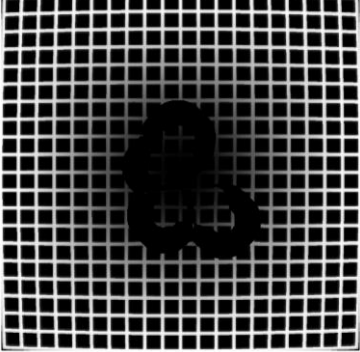


Figure 5-2.- Schematic eye model with drusen deformations of $300\ \mu\text{m}$ in the retina.

In order to show the manner that the drusen affect the central vision, three retinal matrices were generated with drusen sizes of $63 \mu\text{m}$, $300 \mu\text{m}$, and $800 \mu\text{m}$. With these matrices were developed the simulations of a preloaded image and the Amsler grid, as Table 5.1 describes.

Table 5.1.- Amsler grid and image simulation from a retina with different size of drusen.

Drusen Size (μm)	Retinal Matrix	Amsler Grid Simulation	Image Simulation
63			
300			
800			

From Table 5.1 can be observed that the drusen can be simulated and even at small sizes, $63 \mu\text{m}$ for example, deformities are visible. Now, if the drusen size is larger, the effect of the malformations is noticed and agrees with the published review.

Once the simulations were developed and the matrices of drusen were working to reproduce the Amsler grid effects, a series of cross-sectional retinal fundus images were acquired in order to simulate the Amsler grids. A Spectralis Ocular Coherence Tomography, by Heidelberg Engineering was used to acquire the fundus retinal images with help of a staff member in the Visual and Eye Research Institute (VERI), Anglia Ruskin University, Cambridge, UK, place where my internship was held. In the images obtained with the OCT, a bar scale is displayed in the left corner, so, with this measure was possible to build the drusen in the retinal matrices.

Since not enough subjects were recruited, it was possible to obtain just preliminary results. Hence, two cases of AMD are described and illustrates in Figs. 5-3 and 5-4 with their Amsler grid simulations in order to illustrate the possible application of the personalized eye models.

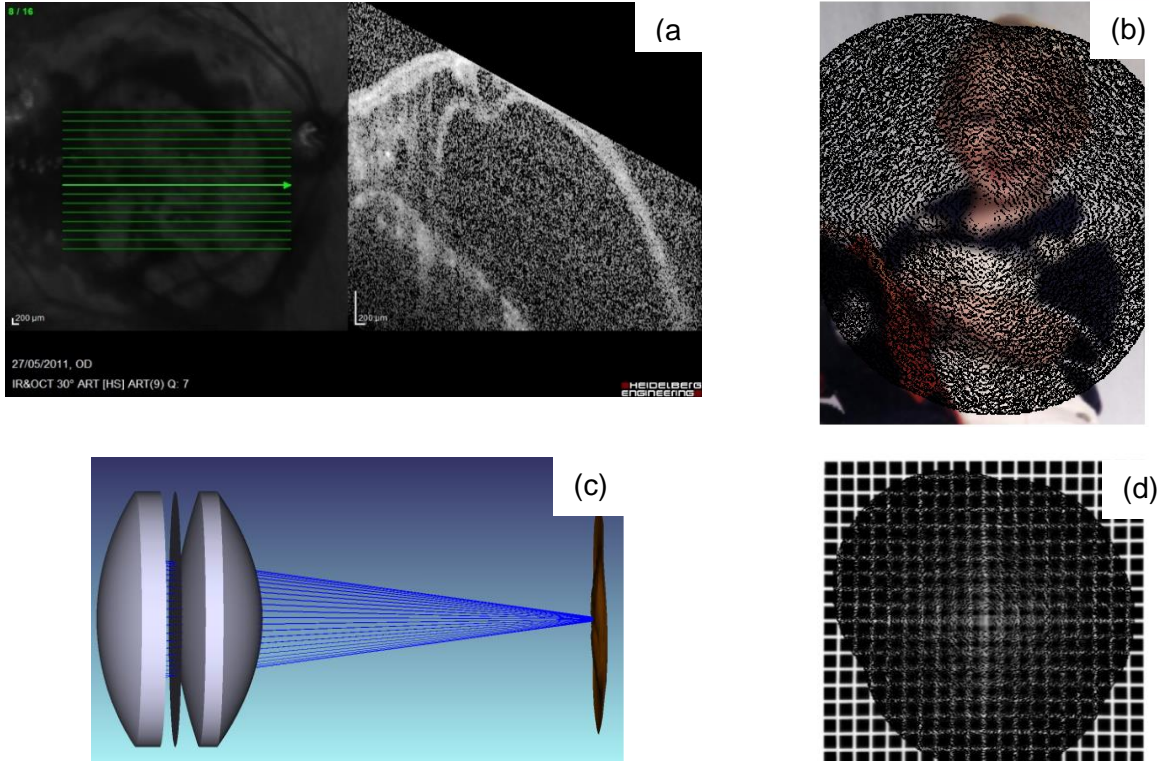


Figure 5-3.- Male subject of 85 years old and AMD. (a) Cross-sectional retinal fundus image of a patient with late AMD. (b) Image vision simulation of an image. (c) Schematic eye of the patient with AMD. (d) Amsler grid simulation.

The subject in Fig. 5-3 was a male of 85 years old and as can be seen, he presents a severe AMD case, in Fig. 5-3 (a) can appreciate the retinal deformation. The drusen size of this patient was about 1200 μm and he was severely sight impaired.

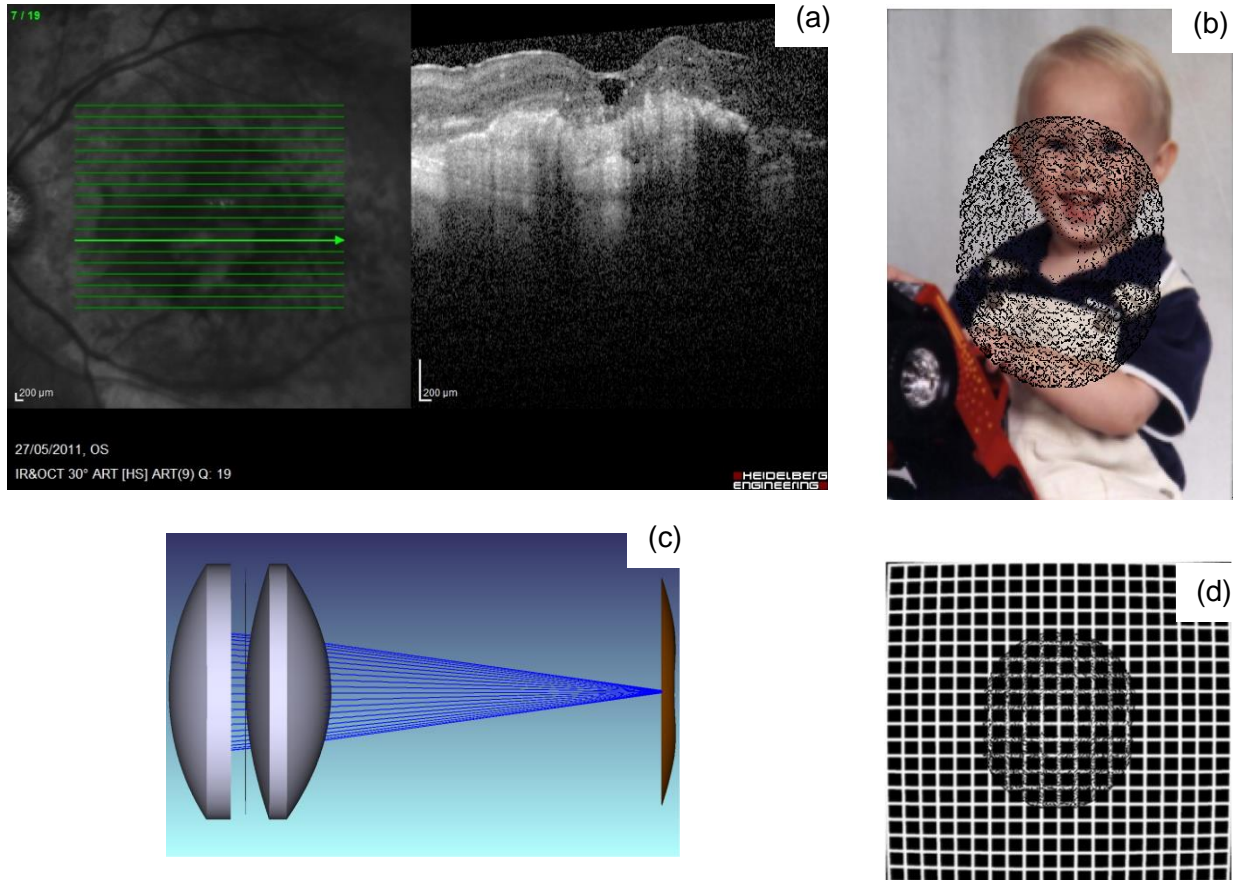


Figure 5-4.- Male subject of 76 years old and AMD. (a) Cross-sectional retinal fundus image of a patient with late AMD. (b) Image vision simulation of an image. (c) Schematic eye of the patient with AMD. (d) Amsler grid simulation.

In Fig. 5-4 shows the simulated the Amsler grid, image and eye schematic of a male with AMD and 76 years old. Even if the case is not as advanced as Fig. 5-4, the central vision of this subject is lost as well.

The results described are an approximation to the development of a cost-effective method to the diagnosis of AMD using a simple Amsler grid. Usually, the Amsler grid is used as a quantitative method to evaluate the progression of AMD, but in this chapter has been explained that it can be an interesting approach. Furthermore, the use

of this grid will be a relevant and useful technique in developing countries that may have limited access to expensive technology, such as OCT scans.

5.2 Conclusions

AMD is one of the main blind causes worldwide. The principal characteristic of late AMD is the presence of drusen, which are edemas formed by proteins, blood and other kinds of components. The manifestation of these affectations are the main characteristics to identify the AMD disease, but instead of an OCT scan, we had proposed a cost-effective technique.

Moreover, preliminaries studies of AMD characterization were presented in this chapter, where the Amsler grid was used as a method to evaluate the progress of AMD. As it was described in the results, it is possible to use this grid in order to quantify the size of the drusen with a high approximation of the dimensions. It was described promissory results with the modeling of eyes with this disease, but more subjects are necessary to evaluate this method in order to validate this technique.

Chapter 6 - Ocular Surface Characterization Using Infrared Thermography

The body temperature can be considered as a reference to human health. As is known, metabolic activities in the body produce heat and this is the reason to relate the condition of the temperature with health. The heat generated has to be released to the body surface in order to keep an internal balance. Transportation of the heat is mainly made by the vascular system, which is another reason and interest to study the temperature of the human body.

Since ancient times, an indirect manner to measure the temperature has been using the hands. It was not until around 1600 when Galileo developed a rudimentary thermometer that he used to quantify variations in the temperature [91]. Nowadays, the mercury thermometer, developed by Wunderlich in 1868, is one of the most used instrument to measure the temperature, besides there are other options such as thermocouples and radiometers. But, the instruments previous mentioned have the characteristic that the contact between patient and device is needed. It is where the importance of a noncontact method is relevant due to is less invasive and also they can cover a bigger area to measure. Infrared thermography is one example of these non-invasive techniques.

A brief description of the infrared thermography and the manner it is used in the human eye is presented in this chapter. Also, a study developed about the dynamic of temperature in glaucoma patients is presented.

6.1 Infrared Thermography and Eye Temperature

Measurement

Infrared (IR) thermography is a widely used technique for temperature measurement, whose main characteristic is that it is non-invasive. The principle used by this procedure is that the objects emit infrared radiation (0.7-100 μm) and in this theory is also consider that a good absorber has to be a good emitter. It is where the meaning of a black body is important for the physics of thermal radiation, which is an object whose temperature and wavelengths of the light emitted are related. Planck, Stefan-Boltzmann and Wien displacement laws, as well as the concept of emissivity, are important principles used in the IR thermography. Equations 6.1, 6.2, 6.3 and 6.4 are the Planck, Wien displacement, Stefan-Boltzmann and emissivity laws respectively.

$$I(\lambda, T) = \frac{2\pi hc^2}{\lambda^5} \frac{1}{e^{\frac{hc}{\lambda kT}} - 1} \quad (6.1)$$

$$\lambda_{\max} = \frac{2898 \mu m \cdot K}{T} \quad (6.2)$$

$$j = \sigma T^4 \quad (6.3)$$

$$\varepsilon = \frac{E_{\lambda}}{E_{b\lambda}} \quad (6.4)$$

I is the spectral radiance in Watts per Steradian per square meter, λ wavelength, and T temperature. h is the Planck constant (6.626×10^{-34} Js), k is the Boltzmann constant (1.381×10^{-23} J/K), c is the speed of light (2.998×10^8 m/s) and σ is the Stefan-Boltzmann constant (5.67×10^{-8} W/m²K⁴). For the emissivity equation, Eq. 6.4, this term denotes the relation between the amount of radiation emitted by an object, E_{λ} , and by an ideal black body, $E_{b\lambda}$. Using the emissivity equation, Eq. 6.3 can be written as

$$j = \varepsilon \sigma T^4 \quad (6.4)$$

As usual, the equipment progress for infrared measurements was due to military and astronomical applications [92]. These days, the availability of infrared detectors

includes thermal and photonic. Examples of thermal detectors are microbolometers, pyroelectrics, and Golay cells, while photonics are quantum well infrared photodetector and mercury-cadmium-telluride [93].

There is evidence that in 1934 Hardy was one of the first that work on the development of an infrared detector to temperature measurement in the skin [94]. However, it was not until the development of better infrared cameras that this technique was widely used. Currently, IR thermography is widely used in medicine due to the advantages of its non-invasive characteristics. Applications of these techniques are in breast cancer, dentistry, and vascular disorders, and of course in ophthalmology [92], [93]. In ophthalmology, the work of Mapstone is known as one of the first tries to measure, first with a bolometer and after with IR cameras, the cornea temperature [95].

Something interesting to remark about IR thermography is that this technique is not possible to measure the intraocular temperature. The reason is that the ocular tissues absorb almost the same wavelengths as water does, and it means that the radiated energy by any ocular tissue is absorbed by the previous tissue [92], [93]. Using the previous explanation can be understood that the tear film, which besides has high water content, absorbs the spectrum radiated by the cornea.

The fact that the tear film is exposed to the environment makes to think about the effect of external factors. Blinking, the temperature of the environment, blood flood to the eye and heat transfers from adjacent structures are examples of external factors [92]. In order to decrease these effects, different strategies have been used such as a period of time to adapt to the room temperature where the ocular surface temperature, OST, is going to be measured. Also, controlling the airflow and humidity are other examples of this.

In the following section, a study of the dynamics of OST is presented, which was performed using IR thermography, in order to evaluate glaucoma subjects and healthy patients.

6.2 Ocular Surface Characterization Using Infrared Thermography

A study with the purpose to calculate the dynamics of OST with IR thermography was developed. Four zones were analyzed, eyelid, central, ellipse and peripheral, in order to explore the differences in vascular and avascular areas. Subjects with glaucoma disease and healthy patients are presented in this section.

6.2.1 Methodology

The study was carried out in the Vision and Eye Research Institute at Anglia Ruskin University, Cambridge, UK. 21 glaucoma patients and 19 healthy subjects were recruited to develop this study in order to test the dynamics of OST using IR thermography.

The previous section explained how the environment can affect the OST measured, thus, the tests were made in a controlled environmental chamber (CEC). The CEC, PSR-B, WEISS Gallenkamp, has the capacity to control the temperature between 5 °C and 40 °C and relative humidity between 5 % and 85 %. Also, the laminar flow is 0.08 m/s controlled by the CEC. This study was performed using a temperature of 23 °C and 45 % of relative humidity, and the subjects were inside the CEC for a period of 10 minutes of adaptation. If the patients had previous surgeries, such as refractive surgery, pathological diseases, they were excluded.

A video per subject was acquired using a thermal camera (Therm-App Hz, Opgal Optronic Industries Ltd., Israel) with a frame rate of 25 Hz. 8 s after the patients opened the eye and their eyes were closed by 10 s, were captured in the video. After the video was recorded, the thermal images were analyzed using MATLAB, were three factors were tested. The temperature at $t = 0$ s, it is at the time after opening eye, the temperature changes over 8 seconds and the cooling rate, slope of the linear function, during three different periods. For the temperature at $t = 0$ s, three areas were tested, 3 mm of the eyelid and central cornea and the peripheral zone. Temperature changes were measured

in the central and peripheral zones and the cooling rate was evaluated from 0-2 s, from 2-4 s, and from 4-8 s. Fig. 6-1 shows the zones analyzed.

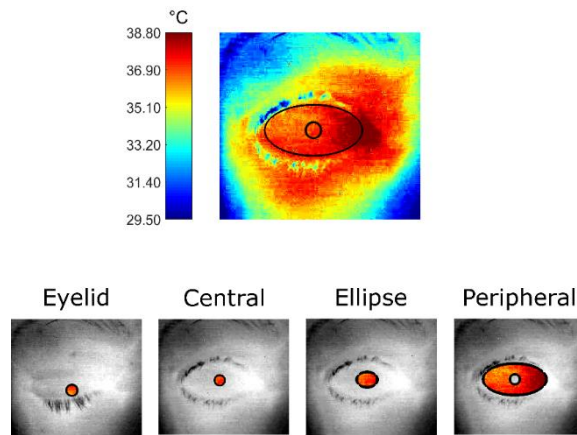


Figure 6-1.- Zones where the temperature was measured. [97]

6.2.2 Results

The results of this work were published in the “*Journal of the Optical Society of America A*”, where a more detailed explanation of results can be consulted [96].

Figure 6-2 shows the plots of the three zones analyzed, eyelid, central ocular surface and peripheral, at $t = 0$ s.

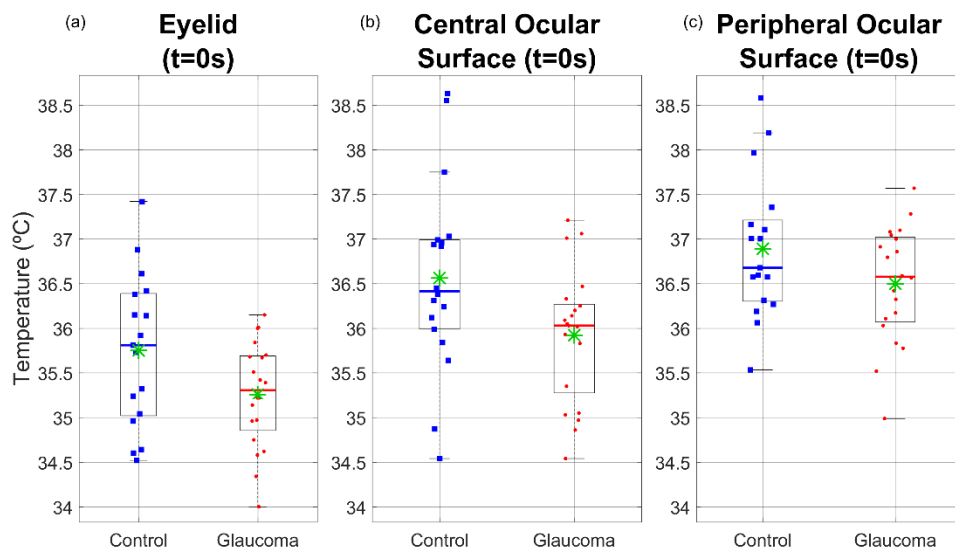


Figure 6-2.- Temperature values measured in control and glaucoma subjects. (a) Eyelid, (b) central ocular surface and (c) peripheral ocular surface at $t = 0$ s. Squares and points represent controls and glaucoma, with the main value in green asterisk. [97]

From the statistical analysis was found that subjects with glaucoma have a cooler temperature in the eyelid than healthy patients. Also, in the central cornea, the values are cooler for glaucoma patients. For the peripheral area, there are no significant differences. $P = 0.046$, $P = 0.036$ and $P = 0.183$ were the values found for eyelid, central and peripheral area, respectively.

The second parameter evaluated was the temperature changes over 8 s in the central cornea. Fig. 6-3 shows evolution.

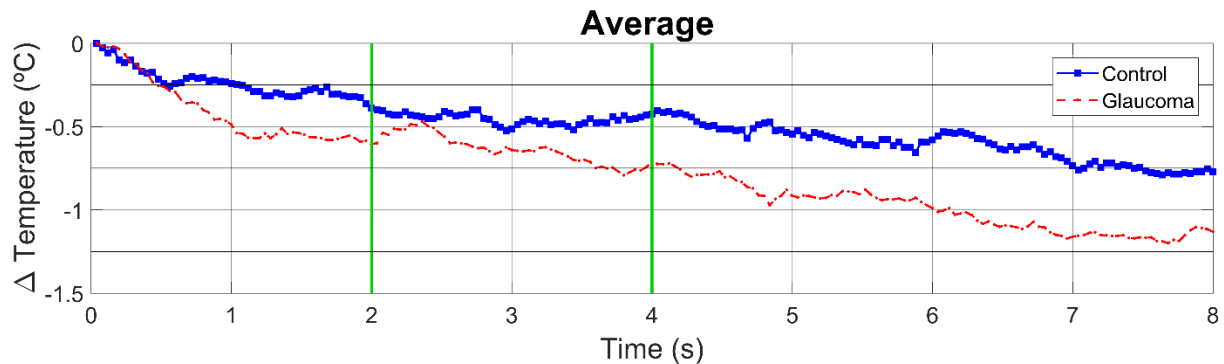


Figure 6-3.- Average OST changes in the central cornea zone. Green lines are the periods of time analyzed to find the cooling rates. [97]

During the first second, the glaucoma subjects registered a decrease of $0.49\text{ }^{\circ}\text{C}$ and healthy patients just $0.24\text{ }^{\circ}\text{C}$. After the first second the cooling behavior of glaucoma patients was faster than healthy subjects. In order to describe the cooling rate, the cooling rate was calculated from 0-2 s, 2-4 s, and 4-8 s. The results are presented in the plots of Fig. 6-4.

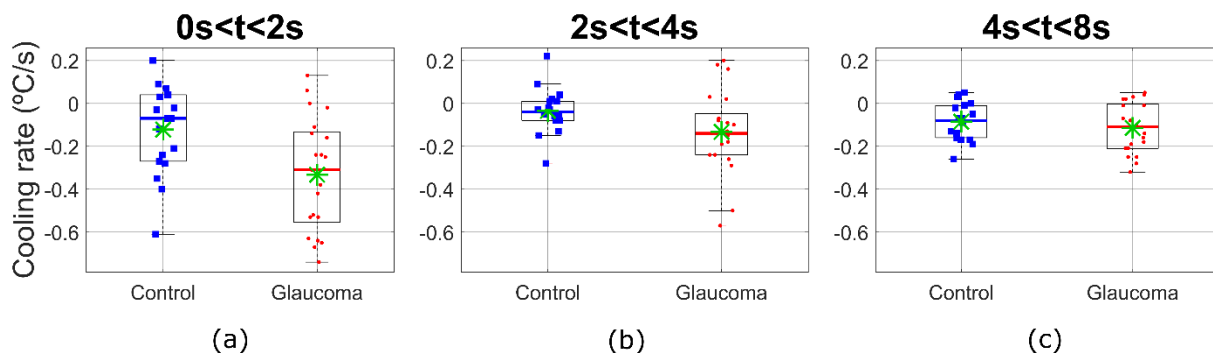


Figure 6-4.- Cooling rate (a) from 0 to 2 seconds, (b) from 2 to 4 seconds and (c) from 4 to 8 seconds. [97]

Table 6.1 shows the values obtained in these periods for glaucoma and healthy subjects.

Table 6.1.- Cooling rate values for the periods of time analyzed.

Period (s)	Cooling rate (°C/s)	
	Glaucoma	Control
0 – 2	-0.333	-0.122
2 – 4	-0.133	-0.035
4 – 8	-0.115	-0.085

For the case of lower temperatures in the glaucomatous eyes, the possible reason could be due that the impaired blood supply. The blood supply could be affected not only in the optic nerve, it could be that the vascular system is affected also for the blood supply. Another possible explanation can be described from the glaucoma medication point of view. Several studies have been described side effects of the hypotensive drops, used to balance the IOP, and some of them affect blood pressure [97]. There is a third possibility due to the dry eye disease, glaucoma subjects suffer this disease and there is evidence that subjects with dry eye have lower temperatures of around one degree than healthy subjects [98].

6.3 Conclusions

In this study was found that on average, the central cornea of patients with glaucoma was 0.64 °C cooler than in healthy subjects. This parameter suggests that due to the glaucoma disease, side effects due to the treatment in these patients such as the eye drops and dry eye, the temperature is cooler.

Also, the cooling rate is faster for glaucoma patients and the peripheral area changes his value although is not significant. Finally, considering that although the central cornea does not have a vascular system, the effect of the alteration in the ocular blood supply in glaucoma subjects has an effect on the thermal dynamics of the central cornea.

Chapter 7 - Conclusions

The main objective of this work was to establish methods that allow improving the ocular aberrations measurements and produce diagnosis techniques to evaluate visual pathologies. Firstly, two numerical wavefront reconstruction methods that improve the measurements of ocular aberrations were described. Secondly, studies on glaucoma and AMD pathologies were presented, in order to develop new techniques to evaluate and diagnose these eye diseases.

The numerical procedures to make wavefront reconstruction are based on the Hartmann and Shack-Hartmann tests. Using two different geometrical configurations of the Hartmann plate, square and hexagonal, cells are formed. These procedures are zonal methods that use the slope measurements to retrieve the wavefront, with the main characteristic that a single analytical expression is not obtained. The main advantage of these techniques is that instead of a single polynomial that fits the whole pupil, several polynomials are obtained. A polynomial per cell is found, so, it means that small irregularities can be identified in small areas.

In the square pattern, quadrangular cells are formed and at each one of the vertices, information of the slope in two directions is obtained. Hence, in each one of the square cells, eight data values are found. Even if the eight measurements are not independent, the wavefront inside the cells can be assumed to be represented by a polynomial expression with five aberration terms. Tilts, defocus and astigmatism, including its axis orientation, aberrations are possible to be obtained. In addition, these coefficients are different for each square cell. This is another advantage, as it was said since small localized errors that cannot be adjusted by a single polynomial expression can be represented with this method. Besides the benefit described in the previous sentence, the analytical function founded is obtained in an exact manner. Although the piston term is not determined with this method, a procedure to calculate the piston term is also presented as a technique that takes advantage of the points shared between cells.

It is important to remark that the results obtained with the square cell integration are better than those found with the trapezoidal integration. In this manner, the square cell integration can replace the trapezoidal integration in order to obtain better results. Moreover, the time to perform this technique proposed is less than with the trapezoidal since some times with the last methods it is necessary to perform the integration in three directions.

For the case of the hexagonal patterns, the geometry is more complicated than the square pattern but it is possible to obtain nine aberration terms instead of five. Moreover, a higher sampling density is achieved with this configuration, so, the pupil is more uniformly sampled, even at the edge. Similar to the square method, a unique analytical expression is obtained for each one of the hexagonal cells shaped. In this hexagonal method, as the hexagon has six sides and six vertices as well, twelve data are available to calculate the nine aberrations terms. Besides, the coefficients obtained with the first method, with the second technique coma and triangular astigmatism can be found. It was described that with hexagonal integration is possible to obtain better results than the trapezoidal method. In some cases, also the hexagonal technique can be better to perform the wavefront retrieval than the square cell integration. The reason is that the hexagonal method allows a higher polynomial representation for each one of the cells. Furthermore, with the two methods presented, a smoothed wavefront is retrieved and the accuracy is higher.

In addition to the methods described, to perform a better ocular aberrations measurement, preliminary results of a technique to model personalized eyes with AMD were briefly described. AMD is one of the main causes of vision loss in the world, and this technique is an initial work trying to link the size, volume and magnitude of retinal edemas, drusen, produced by the late stage of AMD. As in the section of AMD was described, visual distortions caused by the deformities in the macula can be simulated in the Amsler grid. Hence, the final aim is to obtain an inverse procedure to estimate the characteristics of the drusen that generates visual distortion in the retinal image. So, a simple, cost-effective method to evaluate and measure the progression of AMD through the simple Amsler grid test is proposed. Moreover, using the procedure described is possible to

obtain personalized eye models, allowing a better diagnosis. In this aspect, the Amsler grid test may potentially stop being monitoring and qualitatively test to become a quantitative and effective diagnosis technique.

Continuing with visual pathologies, a study to characterize the OST using IR thermography was presented. In this study was found and remarked that the cooling behavior of the ocular surface in patients with glaucoma is faster than healthy subjects. This study also suggests that in the first second after the opening eye there is no difference between glaucoma and healthy subjects. After this time, the ocular surface of glaucoma subjects has a considerable decrease in the temperature. As part of the study, room temperature and relative humidity were established at 23°C and 45% respectively, to evaluate the effects of these parameters in the OST. The hypothesis of the cooler temperature in glaucomatous eyes can be explained from several possibilities. The first one due to the damaged blood supply to the eye. The second could be explained due to the glaucoma medication since the side effects of the drops used have an influence on the blood pressure. Finally, dry eye disease is the third reason for the cooler temperature in glaucoma subjects. It has to be considered that the full explanation of this can be the combination of all three factors since glaucoma is a complex disease.

Overall, four studies were performed in this work to improve the techniques to measure ocular aberrations and methods of pathology diagnosis. Although there are more studies needed and work on these topics presented in this work, there is future work to do in order to improve them. Certainly, the results show the potential of the works developed through this thesis in order to improve the visual quality of the people.

Bibliography

- [1] C. Scheiner, *Oculus, hoc est: Fundamentum opticum*. Flesher, 1652.
- [2] M. Tscherning, "Die monochromatischen aberrationen des menschlichen uges," *Z. Psychol. Physiol. Sinne.*, vol. 17, pp. 456–471, 1894.
- [3] J.Hartmann, "Bemerkungen über den Bau und die Justirung von Spektrograpen," *Zt. Instrumentenkd*, vol. 20, pp. 47–58, 1900.
- [4] S. Marcos, "and Optical Aberrations," *Opt. Photonics News*, no. January, pp. 22–25, 2001.
- [5] C. Mcalinden, "Corneal refractive surgery: Past to present," *Clin. Exp. Optom.*, vol. 95, no. 4, pp. 386–398, 2012.
- [6] F. Ronald S, "Darwin and Helmholtz on imperfections of the eye," *Arch. Ophthalmol.*, vol. 128, no. 9, pp. 1209–1211, 2010.
- [7] H. J. Caulfield and K. Biedermann, "The Eye, Hartmann, Shack, and Scheiner," *Opt. Inf. Process. A Tribut. to Adolf Lohmann*, 2017.
- [8] J. Liang, D. R. Williams, and D. T. Miller, "Supernormal vision and high-resolution retinal imaging through adaptive optics," *J. Opt. Soc. Am. A*, vol. 14, no. 11, p. 2884, 1997.
- [9] P. Artal, "Image Formation in the Living Human Eye," *Annu. Rev. Vis. Sci.*, vol. 1, no. 1, pp. 1–17, 2015.
- [10] P. Artal, *Handbook of Visual Optics, Volume One: Fundamentals and Eye Optics*. CRC Press, 2017.
- [11] D. A. Atchison and G. Smith, *Optics of the Human Eye*. Butterworth-Heinemann, 2000.
- [12] C. E. Willoughby, D. Ponzin, S. Ferrari, A. Lobo, K. Landau, and Y. Omid, "Anatomy

- and physiology of the human eye: Effects of mucopolysaccharidoses disease on structure and function - a review,” *Clin. Exp. Ophthalmol.*, vol. 38, no. SUPPL. 1, pp. 2–11, 2010.
- [13] J. E. Gómez-Correa, S. E. Balderas-Mata, B. K. Pierscionek, and S. Chávez-Cerda, “Composite modified Luneburg model of human eye lens,” *Opt. Lett.*, vol. 40, no. 17, p. 3990, 2015.
- [14] J. E. Gómez-Correa, V. Coello, A. Garza-Rivera, N. P. Puente, and S. Chávez-Cerda, “Three-dimensional ray tracing in spherical and elliptical generalized Luneburg lenses for application in the human eye lens,” *Appl. Opt.*, vol. 55, no. 8, p. 2002, 2016.
- [15] I. Escudero-Sanz and R. Navarro, “Off-axis aberrations of a wide-angle schematic eye model,” *J. Opt. Soc. Am. A*, vol. 16, no. 8, p. 1881, 1999.
- [16] R. C. Bakaraju, K. Ehrmann, E. Papas, and A. Ho, “Finite schematic eye models and their accuracy to in-vivo data,” *Vision Res.*, vol. 48, no. 16, pp. 1681–1694, 2008.
- [17] D. A. Atchison and L. N. Thibos, “Optical models of the human eye,” *Clin. Exp. Optom.*, vol. 99, no. 2, pp. 99–106, 2016.
- [18] A. V. Goncharov and C. Dainty, “Wide-field schematic eye models with gradient-index lens,” *J. Opt. Soc. Am. A*, vol. 24, no. 8, p. 2157, 2007.
- [19] S. R. Flaxman *et al.*, “Global causes of blindness and distance vision impairment 1990–2020: a systematic review and meta-analysis,” *Lancet Glob. Heal.*, vol. 5, no. 12, pp. e1221–e1234, 2017.
- [20] G. Dai, *Wavefront Optics for Vision Correction*. Society of Photo Optical, 2008.
- [21] E. Hecht, *Optics*. Addison-Wesley, 2002.
- [22] D. Malacara, *Óptica básica*. FCE - Fondo de Cultura Económica, 2015.
- [23] M. Born, E. Wolf, and A. B. Bhatia, *Principles of Optics: Electromagnetic Theory of Propagation, Interference and Diffraction of Light*. Cambridge University Press,

- 2000.
- [24] D. Malacara-Hernández and Z. Malacara-Hernández, *Handbook of Optical Design, Second Edition (Optical Engineering)*. 2003.
- [25] G. Hernández-Gómez, D. Malacara-Doblado, Z. Malacara-Hernández, and D. Malacara-Hernández, “Modal processing of Hartmann and Shack–Hartmann patterns by means of a least squares fitting of the transverse aberrations: erratum,” *Appl. Opt.*, vol. 54, no. 8, p. 1870, 2015.
- [26] G. Hernández-Gómez, Z. Malacara-Hernández, and D. Malacara-Hernández, “Hartmann tests to measure the spherical and cylindrical curvatures and the axis orientation of astigmatic lenses or optical surfaces,” *Appl. Opt.*, vol. 53, no. 6, p. 1191, 2014.
- [27] B. C. Platt and R. V Shack, “Lenticular Hartmann Screen,” *Opt. Sci. Newsl.*, vol. 5, pp. 15–16, 1971.
- [28] D. Malacara-hernández and D. Malacara-doblado, “What is a Hartmann test ?,” no. October 2014, 2015.
- [29] V. Laude, S. Olivier, C. Dirson, and J.-P. Huignard, “Hartmann wave-front scanner,” *Opt. Lett.*, vol. 24, no. 24, p. 1796, 1999.
- [30] V. Laude and J. Huignard, “Liquid-crystal Hartmann wave-front scanner,” 2000.
- [31] X. Wei and L. Thibos, “Design and validation of a scanning Shack Hartmann aberrometer for measurements of the eye over a wide field of view,” *Opt. Express*, vol. 18, no. 2, p. 1134, 2010.
- [32] D. Malacara, *Optical Shop Testing*. Wiley, 2007.
- [33] J. Liang, B. Grimm, S. Goelz, and J. F. Bille, “Objective measurement of wave aberrations of the human eye with the use of a Hartmann-Shack wave-front sensor,” vol. 11, no. 7, 1994.
- [34] L. N. Thibos, “Clinical applications of the Shack-Hartmann aberrometer,” *Optom. Vis. Sci.*, vol. 76, no. 12, pp. 817–825, 1999.

- [35] L. N. Thibos, "Principles of Hartmann-Shack aberrometry.," *J. Refract. Surg.*, vol. 16, no. 5, pp. S563-5, 2000.
- [36] W. H. Southwell, "Wave-Front Estimation From Wave-Front Slope Measurements.," *J. Opt. Soc. Am.*, vol. 70, no. 8, pp. 998–1006, 1980.
- [37] D. Malacara-Hernández, *Optical Shop Testing*, vol. 26, no. 7. 1979.
- [38] G. Hernández-Gómez, D. Malacara-Doblado, Z. Malacara-Hernández, and D. Malacara-Hernández, "Modal processing of Hartmann and Shack-Hartmann patterns by means of a least squares fitting of the transverse aberrations," *Appl. Opt.*, vol. 53, pp. 7422–7434, 2014.
- [39] I. Ghozeil and J. E. Simmons, "Screen Test for Large Mirrors," *Appl. Opt.*, vol. 13, pp. 1773–1777, 1974.
- [40] D. P. Salas-Peimbert, D. Malacara-Doblado, V. M. Durán-Ramírez, G. Trujillo-Schiaffino, and D. Malacara-Hernández, "Wave-front retrieval from Hartmann test data," *Appl. Opt.*, vol. 44, no. 20, p. 4228, 2005.
- [41] W. L. Wong *et al.*, "Global prevalence of age-related macular degeneration and disease burden projection for 2020 and 2040: A systematic review and meta-analysis," *Lancet Glob. Heal.*, vol. 2, no. 2, pp. e106–e116, 2014.
- [42] X. Guillonneau, C. M. Eandi, M. Paques, J. A. Sahel, P. Sapiéha, and F. Sennlaub, "On phagocytes and macular degeneration," *Prog. Retin. Eye Res.*, vol. 61, pp. 98–128, 2017.
- [43] S. L. Fine, J. W. Berger, M. G. Maguire, and A. C. Ho, "Age-related macular degeneration," *N. Engl. J. Med.*, vol. 342, no. 7, 2000.
- [44] F. L. Ferris *et al.*, "Clinical classification of age-related macular degeneration," *Ophthalmology*, vol. 120, no. 4, pp. 844–851, 2013.
- [45] M. Dinu, G. Pagliai, A. Casini, and F. Sofi, "Food groups and risk of age-related macular degeneration: a systematic review with meta-analysis," *Eur. J. Nutr.*, vol. 58, no. 5, pp. 1–21, 2018.

- [46] E. Pead *et al.*, “Automated detection of age-related macular degeneration in color fundus photography: a systematic review,” *Surv. Ophthalmol.*, vol. 64, no. 4, pp. 498–511, 2019.
- [47] C. J. F. Boon, J. P. H. van de Ven, C. B. Hoyng, A. I. den Hollander, and B. J. Klevering, “Cuticular drusen: Stars in the sky,” *Prog. Retin. Eye Res.*, vol. 37, pp. 90–113, 2013.
- [48] P. T. Johnson *et al.*, “Drusen-associated degeneration in the retina,” *Investig. Ophthalmol. Vis. Sci.*, vol. 44, no. 10, pp. 4481–4488, 2003.
- [49] E. Midená and S. Vujosevic, “Metamorphopsia: An Overlooked Visual Symptom,” *Ophthalmic Res.*, vol. 55, no. 1, pp. 26–36, 2015.
- [50] A. Suansilpong and S. Uaratanawong, “Accuracy of amsler grid in screening for chloroquine retinopathy,” *J. Med. Assoc. Thail.*, vol. 93, no. 4, pp. 462–466, 2010.
- [51] M. M. Diab, M. Nassar, and N. Badawi, “Resurrection of the Amsler chart in macular diseases,” *Menoufia Med. J.*, vol. 28, no. 1, p. 174, 2015.
- [52] M. Amsler, “Earliest symptoms of diseases of the macula,” *Br. J. Ophthalmol.*, vol. 37, no. 9, pp. 521–537, 1953.
- [53] J. B. Jonas, T. Aung, R. R. Bourne, A. M. Bron, R. Ritch, and S. Panda-jonas, “Seminar Glaucoma,” vol. 390, pp. 83–93, 2017.
- [54] S. D. Kaštelan, M. T. T, K. M. D. Soldo, and J. S. T, “How Ocular Surface Disease Impacts the Glaucoma Treatment Outcome,” vol. 2013, no. Table 1, 2013.
- [55] A. Tuulonen *et al.*, “The finnish evidence-based guideline for open-angle glaucoma,” *Acta Ophthalmol. Scand.*, vol. 81, no. 1, pp. 3–18, 2003.
- [56] A. Iwase *et al.*, “The prevalence of primary open-angle glaucoma in Japanese: The Tajimi Study,” *Ophthalmology*, vol. 111, no. 9, pp. 1641–1648, 2004.
- [57] C. E. Saade, H. B. Lari, T. L. Berezina, R. D. Fechtner, and A. S. Khouri, “Topical glaucoma therapy and ocular surface disease: A prospective, controlled cohort study,” *Can. J. Ophthalmol.*, vol. 50, no. 2, pp. 132–136, 2015.

- [58] F. Pérez-Bartolomé, J. M. Martínez-De-La-Casa, P. Arriola-Villalobos, C. Fernández-Pérez, V. Polo, and J. García-Feijoó, "Ocular surface disease in patients under topical treatment for glaucoma," *Eur. J. Ophthalmol.*, vol. 27, no. 6, pp. 694–704, 2017.
- [59] D. Malacara-Hernandez, "Testing and centering of lenses by means of a Hartmann test with four holes," *Opt. Eng.*, vol. 31, no. 7, p. 1551, 1992.
- [60] Z. Malacara-Hernández, D. Malacara-Doblado, and D. Malacara-Hernández, "Least-squares fitting of Hartmann or Shack–Hartmann data with a circular array of sampling points," *Appl. Opt.*, vol. 54, no. 28, p. E113, 2015.
- [61] F. J. Gantes-Nuñez, Z. Malacara-Hernández, D. Malacara-Doblado, and D. Malacara-Hernández, "Zonal processing of Hartmann or Shack–Hartmann patterns," *Appl. Opt.*, vol. 56, no. 7, p. 1898, 2017.
- [62] C. E. Shannon, "Communication in the Presence Noise *," pp. 10–21, 1947.
- [63] B. Pathak and B. R. Boruah, "Improved wavefront reconstruction algorithm for Shack-Hartmann type wavefront sensors," *J. Opt.*, vol. 16, p. 55403, 2014.
- [64] M. Kasper, D. Looze, S. Hippler, R. Davies, and A. Glindemann, "Increasing the sensitivity of a Shack-Hartmann sensor," 2016.
- [65] I. Mochi and K. A. Goldberg, "Modal wavefront reconstruction from its gradient," *Appl. Opt.*, vol. 54, no. 12, p. 3780, 2015.
- [66] L. Huang, J. Xue, B. Gao, C. Zuo, and M. Idir, "Spline based least squares integration for two-dimensional shape or wavefront reconstruction," *Opt. Laser Enginerring*, vol. 91, pp. 221–226, 2017.
- [67] F. Dai, J. Li, X. Wang, and Y. Bu, "Exact two-dimensional zonal wavefront reconstruction with high spatial resolution in lateral shearing interferometry," *Opt. Commun.*, vol. 367, pp. 264–273, 2016.
- [68] D. R. Luke, J. V Burke, and R. G. Lyon, "Reconstruction : Theory and Numerical Methods," *Society*, vol. 44, no. 2, pp. 169–224, 2002.

- [69] J. M. Bardsley, "Wavefront Reconstruction Methods for Adaptive," *Image (Rochester, N.Y.)*, pp. 1–16, 2006.
- [70] J. Silva, E. Brunner, A. Polo, C. De Visser, and M. Verhaegen, "Wavefront reconstruction using intensity measurements for real-time adaptive optics," *2014 Eur. Control Conf. ECC 2014*, pp. 2412–2417, 2014.
- [71] G.-M. Dai, "Wavefront Reconstruction from Slope Data Within Pupils of Arbitrary Shapes Using Iterative Fourier Transform," *Open Opt. J.*, vol. 1, no. 1, pp. 1–3, 2007.
- [72] L. Huang, M. Idir, C. Zuo, K. Kaznatcheev, L. Zhou, and A. Asundi, "Comparison of two-dimensional integration methods for shape reconstruction from gradient data," *Opt. Lasers Eng.*, vol. 64, pp. 1–11, 2015.
- [73] M. Lombardo and G. Lombardo, "New methods and techniques for sensing the wave aberrations of human eyes," *Clin. Exp. Optom.*, vol. 92, no. 3, pp. 176–186, 2009.
- [74] A. S. Bruce and L. J. Catania, "Clinical applications of wavefront refraction," *Optom. Vis. Sci.*, vol. 91, no. 10, pp. 1278–1286, 2014.
- [75] N. Visser, T. T. J. M. Berendschot, F. Verbakel, A. N. Tan, J. de Brabander, and R. M. M. A. Nuijts, "Evaluation of the comparability and repeatability of four wavefront aberrometers," *Investig. Ophthalmol. Vis. Sci.*, vol. 52, no. 3, pp. 1302–1311, 2011.
- [76] S. Marcos, "A BERROMETRY: BASIC SCIENCE AND CLINICAL APPLICATIONS," pp. 197–213, 2006.
- [77] M. Lombardo and G. Lombardo, "Wave aberration of human eyes and new descriptors of image optical quality and visual performance," *J. Cataract Refract. Surg.*, vol. 36, no. 2, pp. 313–331, 2010.
- [78] V. Toal and B. Mcgrath, "Ocular Aberrations Wavefront Sensor In Clinical Application Matthew Sheehan B App Sc (Optometry)," no. April, 2008.
- [79] M. X. Wang, *Corneal Topography in the Wavefront Era: A Guide for Clinical*

Application. 2006.

- [80] A. Castillo Gómez, A. Verdejo del Rey, C. Palomino Bautista, A. Escalada Ferrándiz, D. Carmona González, and S. Ceballos Burgos, “Principles and Clinical Applications of Ray-Tracing aberrometry,” *Emmetropia*, no. 3, pp. 96–110, 2012.
- [81] T. Liu, L. Thibos, G. Marin, and M. Hernandez, “Evaluation of a global algorithm for wavefront reconstruction for Shack-Hartmann wave-front sensors and thick fundus reflectors,” *Ophthalmic Physiol. Opt.*, vol. 34, no. 1, pp. 63–72, 2014.
- [82] R. Henselmans, L. A. Cacace, G. F. Y. Kramer, P. C. J. N. Rosielle, and M. Steinbuch, “The NANOMEFOS non-contact measurement machine for freeform optics,” *Precis. Eng.*, vol. 35, pp. 607–624, 2011.
- [83] K. Garrard, T. Bruegge, J. Hoffman, T. Dow, and A. Sohn, “Design tools for freeform optics,” *Curr. Dev. Lens Des. Opt. Eng. VI*, vol. 5874, no. August 2005, p. 58740A, 2005.
- [84] L. B. Kong and C. F. Cheung, “Design, fabrication and measurement of ultra-precision micro-structured freeform surfaces,” *Comput. Ind. Eng.*, vol. 61, no. 1, pp. 216–225, 2011.
- [85] D. G. Smith and J. E. Greivenkamp, “Generalized Method for Sorting Shack-Hartmann Spot Patterns Using Local Similarity,” *Appl. Opt.*, vol. 47, pp. 4548–4554, 2008.
- [86] W. Zhou, T. W. Raasch, and A. Y. Yi, “Design, fabrication, and testing of a Shack–Hartmann sensor with an automatic registration feature,” *Appl. Opt.*, vol. 55, no. 28, p. 7892, 2016.
- [87] O. Soloviev and G. Vdovin, “Hartmann-Shack test with random masks for modal wavefront reconstruction,” *Opt. Express*, vol. 13, no. 23, p. 9570, 2005.
- [88] F. J. Gantes-Nuñez, Z. Malacara-Hernández, D. Malacara-Doblado, and D. Malacara-Hernández, “Zonal wavefront reconstruction of Shack–Hartmann and Hartmann patterns with hexagonal cells,” *Opt. Commun.*, vol. 427, pp. 61–69, 2018.

- [89] D. L. Fried, "Least-square fitting a wave-front distortion estimate to an array of phase-difference measurements," *J. Opt. Soc. Am.*, vol. 67, no. 3, p. 370, 1977.
- [90] R. Klein, M. D. Davis, Y. L. Magli, P. Segal, B. E. K. Klein, and L. Hubbard, "The Wisconsin Age-related Maculopathy Grading System," *Ophthalmology*, vol. 98, no. 7, pp. 1128–1134, 1991.
- [91] J. M. S. Pearce, "A brief history of the clinical thermometer," *Qjm*, vol. 95, no. 4, pp. 251–252, 2002.
- [92] C. Purslow and J. S. Wolffsohn, "Ocular surface temperature: A review," *Eye Contact Lens*, vol. 31, no. 3, pp. 117–123, 2005.
- [93] J. H. Tan, E. Y. K. Ng, U. Rajendra Acharya, and C. Chee, "Infrared thermography on ocular surface temperature: A review," *Infrared Phys. Technol.*, vol. 52, no. 4, pp. 97–108, 2009.
- [94] J. D. Hardy, "THE RADIATION OF HEAT FROM THE HUMAN BODY: I. An Instrument for Measuring the Radiation and Surface Temperature of the Skin.," *J. Clin. Invest.*, vol. 13, no. 4, pp. 593–604, 1934.
- [95] R. Mapstone, "Ocular thermography.," *Br. J. Ophthalmol.*, vol. 54, no. 11, pp. 751–754, 1970.
- [96] N. García-Porta, F. J. Gantes-Nuñez, J. Tabernero, and S. Pardhan, "Characterization of the ocular surface temperature dynamics in glaucoma subjects using long-wave infrared thermal imaging: publisher's note," *J. Opt. Soc. Am. A*, vol. 36, no. 9, p. 1584, 2019.
- [97] P. Kalouda, C. Keskini, E. Anastasopoulos, and F. Topouzis, "Achievements and Limits of Current Medical Therapy of Glaucoma," in *Developments in Ophthalmology*, vol. 59, 2017, pp. 1–14.
- [98] K. E. A. Breau *et al.*, "Temperatures of the Ocular Surface , Lid , and," vol. 14, no. 1, 2016.